Mercury lattice clock : from the Lamb-Dicke spectroscopy to stable clock operation

Rinat Tyumenev

LABORATOIRE DES SYSTÈMES DE RÉFÉRENCE TEMPS-ESPACE

THÈSE DE DOCTORAT DE
L'UNIVERSITÉ PIERRE ET MARIE CURIE

Spécialité : Physique Quantique
ÉCOLE DOCTORALE : Physique en Île de France (ED 564)

Présentée par

Rinat Tyumenev

Pour obtenir le titre de
DOCTEUR de l'UNIVERSITÉ PIERRE ET MARIE CURIE

Sujet de Thèse :

Mercury lattice clock: from the Lamb-Dicke spectroscopy to stable clock operation

Soutenue le 23 juillet 2015 devant le jury composé de :

Jan W. Thomsen	Rapporteur
Martina Knoop	Rapporteur
François Nez	Président du jury
François-Xavier Esnault	Examinateur
Philip Tuckey	Directeur de thèse
Sébastien Bize	Co-encadrant

Contents

Introduction

Measurement of any quantity is one of the most meaningful processes in our life. Everything in our world is relative and if one wants to quantify some feature of an object, for example its length, one has to compare it against some reference. Nowadays this reference is a unit of measure. Some units of measure are defined based on a feature of a certain object, which is considered as a standard, like the meter was defined in 1889 as length of the prototype bar [1]. Modern metrology goes further and tries to get rid of such macroscopic objects and replace them with standards based on microscopic entities as for example the second was redefined based on a transition between two energy levels in Cs atom [2]. Moreover, metrology tends to define fundamental constants and use them to define units [3] like for instance the meter was redefined in terms of second and the speed of light in 1983 [4]. In our daily life we are continuously using standards, such as kilogram, meter, kelvin and of course second and nowadays standards are international and united in systems of units. With great advances in science and technologies the accuracy (see ch.1 for accuracy and stability) of the standards is continuously improving. The most accurate standards for now are the standards of frequency and time with outstanding relative accuracy of $\sim 2\times10^{-16}$ [5], [6], [7]. Ultra-precise and ultra-stable frequency and time standards are of great importance for fundamental science, for example making it possible to measure fundamental constants with higher precision and test the validity of fundamental theories, as well as for industry and applications, for instance stable frequency standard is prerequisite to the operation of satellite navigation systems (GPS, GLONASS, Galileo, BeiDou) and worldwide digital data networks.

In spite of the fact that today's primary frequency standards' accuracy and stability are very high, there is still demand for even more ac-

curate and stable clocks. Since more stable and precise clocks would not only increase the performance of existing applications, but also give rise to new ones, such as precise measurement of the Earth gravitational field for example. However, current primary standards have reached their stability limit that can not be surpassed (see ch.1) and therefore a new generation of more accurate and stable clocks in the optical domain is being developed (see sec.1.1 and 1.2), which will become new primary frequency standard in the future.

Several atomic species listed in the table 1 are being used as a reference in optical clocks all over the world in the attempt to create the most accurate frequency standard. Optical standards based on various atomic species have different advantages and disadvantages among which is the sensitivity to black body radiation (see sec.2.3.1). Today, fluctuations of a clock frequency induced by the black body radiation (BBR) are one of the main and challenging limits of optical clocks accuracy that requires a lot of effort to suppress it. Best optical clocks based on neutral Yb and Sr faced this limit recently and had to implement complicated radiation shield as in case of Yb [8] or cryogenic environment as in case of Sr [9] in order to reach uncertainty levels of a few 10^{-18}.

Table 1. *Theoretical calculations for the fractional BBR shift at 300 K of the clock transition for different atomic species. Given uncertainty corresponds to temperature uncertainty of 1 K.*

	Clock transition	BBR shift	Uncertainty	Reference
Al^+	$^1S_0 \rightarrow ^3P_0$ (267 nm)	$-8 \cdot 10^{-18}$	$3 \cdot 10^{-18}$	Rosenband et. al., 2006
In^+	$^1S_0 \rightarrow ^3P_0$ (237 nm)	$< -7 \cdot 10^{-17}$	$8 \cdot 10^{-19}$	Rosenband et. al., 2006
Hg	$\mathbf{^1S_0 \rightarrow ^3P_0}$ **(266 nm)**	$\mathbf{-1.6 \cdot 10^{-16}}$	$\mathbf{2 \cdot 10^{-18}}$	**Hachisu et. al., 2008**
Mg	$^1S_0 \rightarrow ^3P_0$ (458 nm)	$-3.9 \cdot 10^{-16}$	$1 \cdot 10^{-17}$	Porsev and Derevianko et. al., 2006
Sr^+	$4^2S_{1/2} \rightarrow 3^2D_{5/2}$ (674 nm)	$-5.4 \cdot 10^{-16}$	$> 7 \cdot 10^{-17}$	Mitroy et. al., 2008
Sr	$^1S_0 \rightarrow ^3P_0$ (698 nm)	$-5.5 \cdot 10^{-15}$	$1 \cdot 10^{-16}$	Porsev and Derevianko et. al., 2006
Yb	$^1S_0 \rightarrow ^3P_0$ (579 nm)	$-2.6 \cdot 10^{-15}$	$3 \cdot 10^{-16}$	Porsev and Derevianko et. al., 2006

As one can see from the table 1 the theoretical estimation of clock frequency shift due to the BBR for neutral mercury is 16 and 34 times less than for Yb and Sr correspondingly, which means that same level

of uncertainty can be reached with much less effort on an environment temperature control. Notice, that the same factors also apply to the sensitivity to static electric fields, which have significant contribution to the accuracy budget of a clock [10]. It was a very strong motivation to use neutral mercury as a reference for optical clock and in 2004 it was independently proposed at LNE-SYRTE (Laboratoire National de métrologie et d'Essais-Systemes de Référence Temps-Espace) in Observatoire de Paris, France and at Tokyo University, Japan [11], to use mercury in an optical lattice clock. Besides low BBR sensitivity, mercury has a relatively simple energy level structure, a relevant part of which is shown on figure (1). Mercury has relatively strong intercombination transition ${}^1S_0 \rightarrow {}^3P_1$ favourable for laser cooling with a Doppler limit at 30.6 μK and weakly coupled ultra-narrow ${}^1S_0 \rightarrow {}^3P_0$ transition with a linewidth of approximately 100 mHz. This makes mercury a very good candidate for an optical frequency standard that in theory will become the most stable standard among atomic species presented in the table 1 reaching the relative instability below 1×10^{-18} after less than 10 000 s of integration.

In addition, mercury is one of the heaviest atoms that were ever laser cooled. It has many naturally occurring isotopes that are not that well studied in laser cooled regime, which makes mercury a very interesting species to experiment with. Mercury is of interest as well for fundamental physics tests and search of a unified field theory and new physics beyond the standard particle model. For instance, mercury is a good candidate to test the invariance of the fine structure constant α. Variation of α with time can be studied via the change of the frequency ratio of two atomic clocks referenced to hyperfine transitions in two different atomic species. This can be done by measuring the frequency difference of the two clocks and relating it to the change of α through the relativistic frequency shifts [12]. The heavier the atomic species, the bigger the relativistic frequency shifts, which makes mercury favourable for these tests.

In this thesis I will describe all the advantages and disadvantages of neutral mercury as a frequency standard reference in chapter 2, the state of the experiment at the beginning of this thesis in chapter 3, the work that had been done on the improvement of the setup in chapter 4 and the results of the experiments performed on the improved setup in chapter 5.

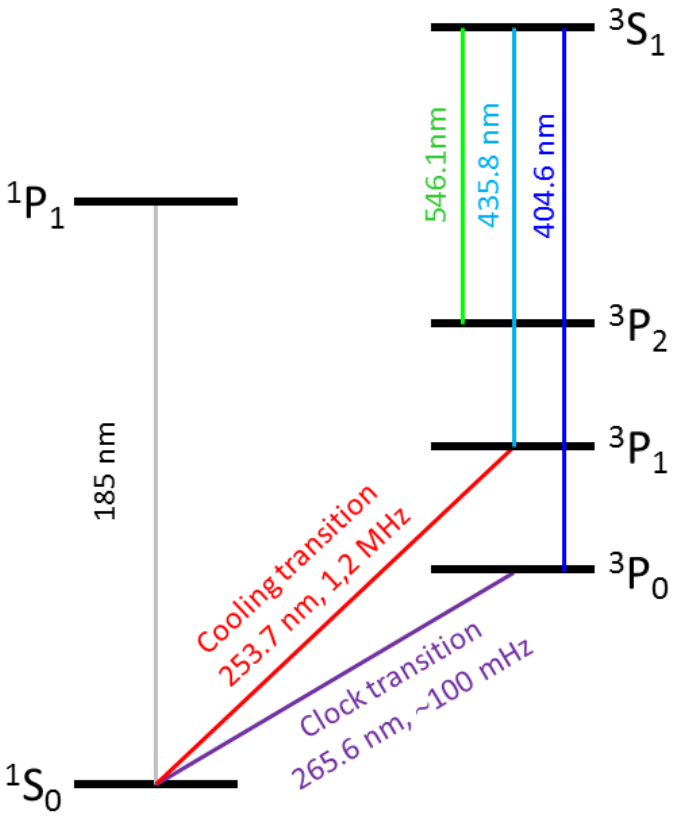

Figure 1. *Mercury atom lowest energy levels scheme. Detailed information about cooling and clock transitions can be find in sections 2.2 and 2.3 respectively*

Chapter 1

Optical frequency standards

The very basic and simple scheme of a frequency standard is shown on fig. 1.1. It consists of a local oscillator, a reference and a servo system. The frequency of the local oscillator $\nu(t)$ is being compared to the frequency of a reference ν_0. Then the result of the comparison $\delta(t) = \nu(t) - \nu_0$ is fed into the servo system. Based on $\delta(t)$ servo system generates a correction signal, which introduces a shift of the local oscillator frequency such that $\delta(t) \to 0$. Thereby the frequency of the local oscillator is actively locked to the frequency of the reference.

An ideal local oscillator after being locked to a reference would provide exactly the frequency ν_0 of the reference, but it is not the case in reality. Frequency of a real device will fluctuate with time to some extent. Therefore all frequency standards are characterized by two main quantities. First of all "good" frequency standards should have high frequency stability, which means that a set of temporal measurements of local oscillator's frequency should be well concentrated around some averaged frequency ν_{avg}, i.e. deviation of the measured frequency from ν_{avg} should be small. The second criteria is the systematic uncertainty, which reflects how well ν_{avg} matches the frequency of unperturbed atomic transition, the closer ν_{avg} to the frequency of the transition the better the clock. It is also common and useful to characterize a clock by its precision. This can be defined as the difference between the actual output frequency and the nominal value with respect to a primary frequency standard. If there is no absolute reference or it is less accurate than the frequency standard that is being compared, then the precision of the standard is defined as the limits of the confidence interval of the measured quantity [13]. In order to be able to compare

completely different frequency standards relative stability and relative accuracy are often used, which are the stability and accuracy divided by a carrier frequency.

Along with advances in science and technology the stability and accuracy of time and frequency standards are increasing, demanding more and more accurate and stable references. It became apparent that atoms are very well isolated and robust against external perturbations and able to provide stable, reproducible and universal frequency reference. In 1950s it was shown that using the appropriate transition between two energy levels in caesium (Cs) atom it is possible to reach relative frequency uncertainty $\frac{\Delta\nu}{\nu} = 1 \times 10^{-9}$ [14], where $\Delta\nu$ is frequency deviation and ν is the central frequency of the transition. This led to the fact that in the 1967 the second was redefined as duration of 9 192 631 770 periods of the radiation corresponding to the

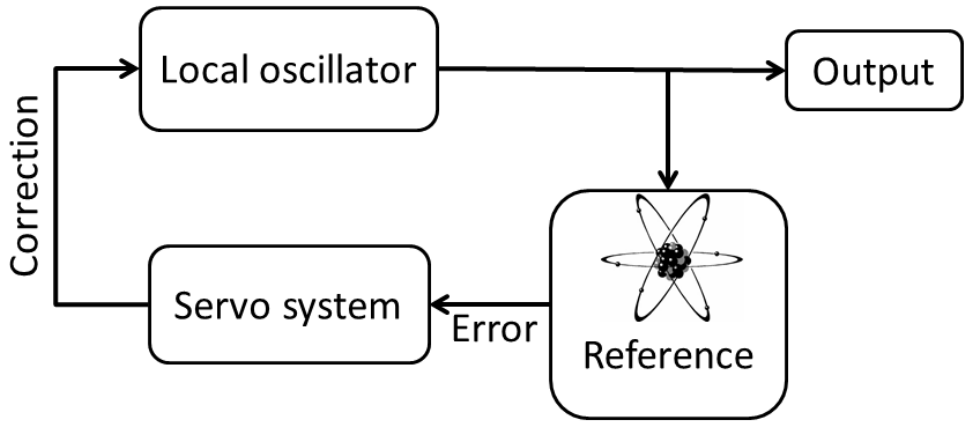

Figure 1.1. *Basic scheme of a frequency standard.*

transition between the two hyperfine levels of the ground state of the caesium 133 atom [15]. This stimulated fast development, evolution as well as implementation of atomic clocks in industry. The research of microwave atomic clocks was advancing for more than 50 years increasing the accuracy with an average speed of one order of magnitude per decade. Today best atomic Cs clocks, which are called Cs fountains, because in this clock atoms at micro kelvin temperature are being launched vertically as in fountains, has relative frequency uncertainty of $\sim 2 \times 10^{-16}$ and stability $1.6 \times 10^{-14}\tau^{-1/2}$. This is the limit that can not be surpassed by microwave clocks, because of sta-

bility issues due to cold atom collisions and distributed cavity phase shift [16].

The way to reach even higher relative frequency uncertainty is to switch to the optical frequency domain. Optical frequencies are several orders of magnitude higher than the microwave and the quality factor $Q = \frac{\nu}{\Delta\nu}$ is as well higher in optical domain. For comparison currently for our mercury optical clock the quality factor is $Q \sim 10^{14}$, while for the Cs fountain clock it is only $Q \sim 10^{10}$. Moreover, given level of uncertainty can be reached within much shorter time with optical frequencies comparing to microwave since the stability of a clock limited by quantum projection noise is proportional to Q^{-1}

$$\sigma_y(\tau) \sim \frac{1}{Q}\delta P\sqrt{\frac{T_c}{\tau}}, \tag{1.1}$$

here σ_y is the Allan deviation (see ch.5.4), which is commonly used to characterize stability of a clock , T_c is the cycle time, τ is the time scale at which stability is characterized and δP is the fundamental noise of atomic signal that comes from the indeterminacy of quantum mechanics and known as quantum projection noise (QPN). In case of an ensemble of N_{at} atoms QPN is proportional to $1/\sqrt{N_{at}}$ [17], [18].

With the development of laser cooling and trapping techniques [19] it became possible to confine neutral atoms in a certain area of space in vacuum. Movement of such confined atoms with a good level of approximation can be described as a movement of an oscillator in a harmonic potential. We will assume that an atom oscillates in the trap with frequency ω_t. Then the radiation field that the atom experiences will be phase modulated

$$E(t) = E_0 \cos(\omega_0 t + \delta\cos(\omega_t t)) \tag{1.2}$$

where ω_0 is the frequency of the radiation field and δ is the modulation index, which equals to the maximum phase difference between the modulated and unmodulated radiation field. In the frequency domain such phase modulated radiation field will be represented by a pure unbroadened carrier ω_0 and an infinite series of sidebands with frequencies $\omega_0 \pm n\omega_t$, where $1 < n < \infty$. It was calculated [20] that if an atom is confined to a space, which is less than half wavelength of the radiation field the sidebands become very weak and mostly the radiation at the carrier frequency will be absorbed and emitted by the

atom. Therefore confinement of an atom in the area smaller than the half wavelength of the probe radiation removes the first order Doppler broadening. Such condition is called Lamb-Dicke regime.

Intense development during 30 years led to the creation of two main types of optical atomic clocks, which today have outstanding accuracy and stability and competing with each other for the right to redefine the SI second and become a new primary time and frequency standard.

1.1 Optical clocks based on ions

The first type are the optical clocks that are using ions as a frequency reference - optical ion clocks. The main advantage of using ions is their strong interaction with electric fields, that allows to relatively easily trap and confine them [21]. A single ion can be stored in a trap for months (virtually forever) and probed well into the Lamb-Dicke regime. Putting trapped ions in an ultra-high vacuum environment largely reduces collisions with other atomic species and coupling to the outside world. All this allows modern optical ion clocks to achieve very high accuracy (see e.g. [22]).

However there are also drawbacks in using ions as a frequency reference for an optical clock. The main problem of ion clocks comes from the very same fact the advantage does: ions have a charge. Due to this fact several ions placed in the same potential well are pushed by their mutual Coulomb repulsion from the center of a quadrupole trap to area where trapping field is stronger. This leads to higher amplitude motion of ions in the trap that induces a frequency shift and may inhibit laser cooling [23]. This limits accuracy of a clock. There should be only one ion in a potential well, but the signal from a single ion has big quantum-projection noise (QPN) [17] and a correspondingly high stability limit. With low signal to noise ratio optical ion clocks are limited in short-term stability. Today several atomic species are being used for the optical ion clocks. The accuracy record belongs to the ion clocks made at the NIST laboratories in the USA based on single ions of Al^+. They have reached relative uncertainties at the level of several of 10^{-18} and stability at 10^{-15} level [22]. Ion optical clocks based on Sr^+ and Yb^+ had reported accuracy at the level of 10^{-17} ([24], [25], [26], [27]). Nowadays in order to decrease QPN and

therefore improve short-term stability different types of ion traps (for instance linear Pauli trap [28], surface traps [29]) are being used that are capable to trap several ions in the same time, keeping each ion in a separated potential well [30], [31]. It was found that interaction between separated ions in those traps couldn't be fully suppressed and still gives significant contribution to the loss of accuracy. The way to increase stability without sacrificing the accuracy is to use neutral atoms instead of ions.

1.2 Optical clocks based on neutral atoms

Compared to ions, neutral atoms do not have a charge and therefore their mutual interaction is weaker. More than 10^6 neutral atoms can be confined in the same trap providing much better QPN limit and therefore better short-term stability in comparison to ion clocks. At the same time neutral atoms have low sensitivity to electromagnetic fields which makes them difficult to trap. In order to trap neutral atoms at room temperature in a deep enough potential well one would have to generate fields with an unreasonably high amplitude. Nevertheless, with the discovery and development of laser cooling techniques it became possible to cool neutral atoms down to temperatures of order of tens of μK (see chapter 3.2) and drastically reduce their kinetic energy. The lower the kinetic energy of an atom, the smaller the minimal depth of a potential well that is required to trap it.

It will be shown in section 2.3.2 that an electromagnetic wave shifts the energy levels in atom due to ac-Stark effect. Two coherent counter propagating and overlapped laser beams with the same wavelength λ_l form a standing wave with intensity nodes separated by $\lambda_l/2$. Such intensity pattern will create a spatially modulated Stark shift of the energy levels in atom. As the result an atom placed in the standing wave will experience optical potential

$$U(r,z) = U_0 \exp\left[-2\left(\frac{r}{w(z)}\right)^2\right]\cos^2(k_l\, z) \tag{1.3}$$

where z is the axis along the direction of propagation of the light, $w(z)$ is the laser beam waist, r is the radial coordinate in the transverse direction, k_l is the wave vector of the light. The depth of the trap U_0 is

proportional to the intensity of the light

$$U_0 = -\frac{8\pi}{c}\alpha(\omega_l)I_l \tag{1.4}$$

where $\alpha(\omega_l)$ is the polarizability (see sec.2.3.2). It was found that the depth of the trap created by two laser beams of reasonable power was big enough to trap atoms cooled down to μK temperatures. Such traps are called dipole or lattice traps [32]. In principle, lattice traps are not suitable for atomic clocks due to the fact that the energy shifts induced by the trap light of the ground and excited states of a clock transition are different. This causes a frequency shift of the clock transition that depends on the intensity of the lattice light and worsens the accuracy and stability of the clock. The situation changed with the proposal of the magic wavelength by H. Katori [33]. The idea is to use in lattice traps light at a special so-called "magic" wavelength, for which the energy shifts of the ground and excited states are exactly the same. When this condition is satisfied no frequency shift due to lattice trap occurs (see more in sec.2.3.2). This enabled the use of lattice traps in clocks based on neutral atoms and such clocks are called optical lattice clocks.

Today several atomic species are being used in different laboratories all around the world in optical lattice clock experiments. However not every atom, as well as not every ion, have the right properties to be a reference for an accurate ultrastable clock. The first and the most important criteria is imposed on the clock transition. Highly accurate and stable clocks require atomic species with very high Q-factor. In other words only transitions with sufficiently narrow natural linewidth can provide desirable stability and accuracy. In general allowed dipole transitions have too large linewidths and can not be used as a clock transition. However, one can find some atomic species in which normally forbidden intercombination transitions ($\Delta S \neq 0$) are weakly allowed due to fine and hyperfine mixing of energy levels (see chapters 2.2 and 2.3). These transitions have very narrow linewidth suitable for optical clock applications. It is also favourable if the excited state is not connected to any other transitions except the clock transition, which means no losses of excited atoms due to spontaneous decay to other levels.

The second criteria is the existence of a suitable transition (or combination of transitions) for laser cooling. Laser cooling technique al-

lows to cool atoms down to a certain temperature limit. This limit is proportional to the linewidth γ of the cooling transition - $T_D = \frac{h\gamma}{2k_B}$, and is called Doppler temperature limit [13]. In case of lattice clocks this transition should be relatively narrow, so the atoms could be cooled down to $\approx 100\ \mu K$, but in the same time intensive enough to have good cooling efficiency. However, in some cases sub-Doppler cooling can exist [34].

Several neutral atoms do fit both criteria and were chosen for lattice clock experiments in different laboratories around the world: Yb ([8], [35]), Sr ([36],[9],[37],[38]), Hg ([39]), Mg ([40]). Each of these atomic species has different properties, advantages and disadvantages from the frequency standard point of view, which makes them interesting to study. In chapter 2 detailed description of mercury properties is given and comparison of mercury with other atomic species for each important characteristic is done.

Chapter 2

Neutral mercury from a frequency standards point of view

2.1 General properties of mercury

Mercury has atomic number 80 and its electronic configuration can be written as $1s^2 2s^2 2p^6 3s^2 3p^6 3d^{10} 4s^2 4p^6 4d^{10} 4f^{14} 5s^2 5p^6 5d^{10} 6s^2$. It means that inner shells are complete and the outer 6th shell contains only two electrons, which is similar to electronic configuration of an alkaline-earth-like atom. Mercury has 7 naturally occurring isotopes among which 6 are more than 6% abundant (table 2.1) [41]. Availability of several isotopes allows to study collisional shifts [42], which can be significantly different for different isotopes. If one isotope will prove to

Table 2.1. *Natural isotopes of mercury*

Isotope	Atomic mass	Abundance	Nuclear spin
196	195.965815	0.15%	0
198	197.966752	9.97%	0
199	198.968262	16.87%	1/2
200	199.968309	23.10%	0
201	200.970285	13.18%	3/2
202	201.970626	29.86%	0
204	203.973476	6.87%	0

have big collisional shift it is possible to switch to another one. The isotope with the lowest collisional shift could be more favourable for lattice clocks.

There are two fermions and four bosons among isotopes. All bosons have nuclear spin equal to 0, which means that clock transition is normally forbidden for them. However, it was shown in [43] that, due to Zeeman effect, a small static magnetic field applied to alkaline-earth-like atoms can mimic hyperfine mixing of states and induce coupling to the forbidden $^1S_0 \rightarrow^3 P_0$ transition. This effect is called magnetic quenching of a transition. It is remarkable that quenching of a clock transition also allows to control its linewidth by magnetic field. Thereby in spite the fact, that transition $^1S_0 \rightarrow^3 P_0$ is forbidden in bosons they still can be used for lattice clock purposes. However, fermions were chosen to be used in optical lattice clocks because the clock transition in fermions is weakly allowed (lifetime > 1 s) without additional complications and limits connected with quenching methods. Also, according to the Pauli exclusion principle two fermions can not share state with a given energy in the same time and in the same space. This means that for spin polarized sample of ^{199}Hg atoms each fermion will occupy different motional state of a trap and therefore the atoms are less prone to collide (see more in sec.5.5.1). All the experiments presented in this thesis were performed with ^{199}Hg isotope.

Another remarkable property of mercury is that its boiling and melting points are at 356.73 °C and -38.83 °C respectively at 1 bar pressure. Therefore mercury is liquid at room temperature at normal pressure. From figure 2.1 one can see that in order to have reasonable vapour pressure Sr and Yb, which are mainly used in optical lattice clocks (OLC), have to be heated up to 300-400 °C or more. Mercury has vapour pressure at room temperature 14 orders of magnitude higher than Yb and Sr and has to be on contrary cooled down to not over flood the vacuum chamber. This is another advantage of mercury - absence of an oven or other hot devices helps to control the background temperature with better accuracy and less effort. It also enables the use of efficient sources of slow atoms, such as 2D Magneto-optical trap.

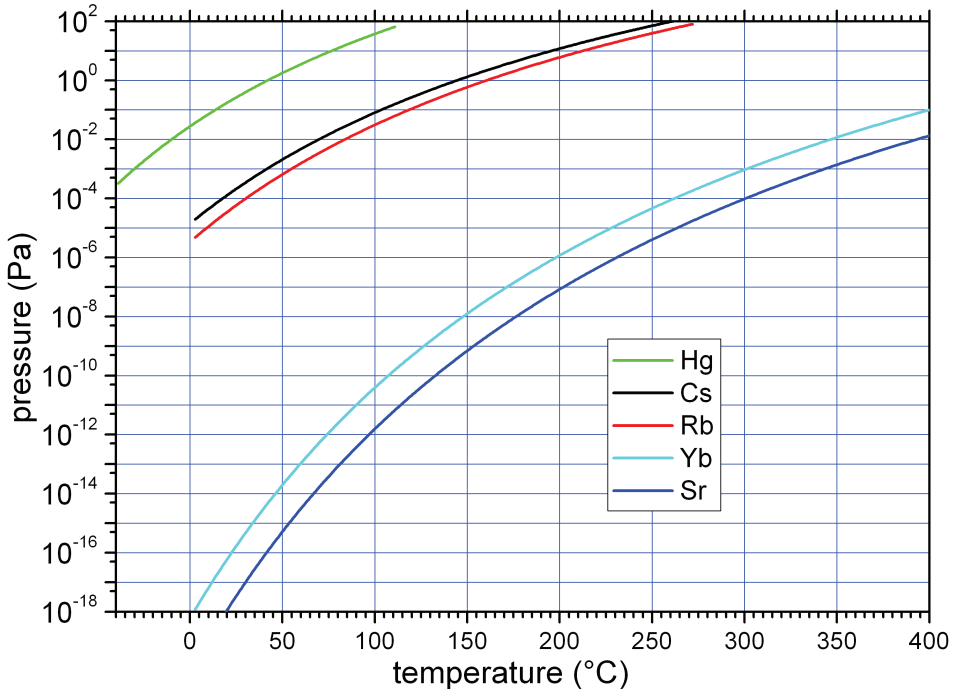

Figure 2.1. *The vapour pressure of liquid mercury compared to liquid caesium and rubidium and solid strontium and ytterbium.The figure is taken from [44].*

2.2 ^{1}S$_0$ - ^{3}P$_1$ cooling transition

We will now look more closely on the cooling transition ${}^1S_0 \rightarrow {}^3P_1$. Intercombination transitions, in which total electronic spin of ground and excited states are different, are not coupled by electric dipole coupling. Therefore in the central field model of atom these transitions are forbidden, but this is no longer true if one takes into account interaction between angular momentum of an electron and its spin. Then the hamiltonian can be written as

$$H_{fs} = H_c + H_r + H_{LS} \tag{2.1}$$

where H_c describes interaction between nucleus and electrons, H_r - repulsive interaction between electrons, and

$$H_{LS} = \xi(\mathbf{r_1})\mathbf{l_1} \cdot \mathbf{s_1} + \xi(\mathbf{r_2})\mathbf{l_2} \cdot \mathbf{s_2}. \tag{2.2}$$

LS-coupling. In the case when H_{LS} is very small unperturbed energy eigen states can be written in Russel-Saunders form $|^{2S+1}L_J\rangle$ and LS-coupling can be treated as perturbation of those. This perturbation

will mix energy eigen states of different S, but not different J, which is good quantum number, so that the new energy levels structure will be

$$\begin{aligned} |^1P_1'\rangle &= -\beta\,|^3P_1\rangle + \alpha\,|^1P_1\rangle \\ |^3P_1'\rangle &= \alpha\,|^3P_1\rangle + \beta\,|^1P_1\rangle \\ |^3P_0'\rangle &= |^3P_0\rangle \\ |^3P_2'\rangle &= |^3P_2\rangle. \end{aligned} \tag{2.3}$$

where α and β are mixing constants that depend on the strength of LS-coupling (2.2). This constants can be estimated from lifetime of the transitions [44], for mercury their values are

$$\begin{aligned} \alpha &= 0.986 \\ \beta &= -0.164. \end{aligned} \tag{2.4}$$

New $|^3P_1'\rangle$ state now consists of $|^3P_1\rangle$ mixed with a small fraction of $|^1P_1\rangle$ that makes it weakly coupled. Strength of the $^1S_0 \rightarrow^3 P_1'$ transition depends on the fraction of $|^1P_1\rangle$ in $|^3P_1'\rangle$. In the case of mercury, the wavelength of the $^1S_0 \rightarrow^3 P_1'$ transition is 253.65 nm and because of quite strong LS-coupling the transition has a width of $\approx$1.2 MHz. This transition is strong enough to perform trapping of more than 10^6 atoms in a magneto-optical trap (see section 3.2) directly from a thermal atomic vapour and in the same time has relatively low Doppler limit temperature $T_D = 30.6\,\mu K$ allowing loading atoms into a dipole trap directly from single stage magneto-optical trap without additional cooling.

2.3 ^{1}S$_0$ - ^{3}P$_0$ clock transition

Fermionic isotopes of mercury ^{199}Hg and ^{201}Hg have non-zero nuclear spins equal to 1/2 and 3/2 respectively. Nuclear spin interacts with the total angular momentum J of the electronic cloud, splitting fine structure energy levels into a hyperfine structure. Hyperfine structure is characterised by total angular momentum F, which is equal to a vector sum of total electronic angular momentum J and nuclear spin I

$$\mathbf{F} = \mathbf{J} + \mathbf{I}. \tag{2.5}$$

This interaction now mixes states with different J, but not different F, so the final $|^3P_0''\rangle$ state will be a mix of fine structure states $|^3P_0'\rangle$, $|^3P_1'\rangle$

and $|^1P_1'\rangle$:

$$|^3P_0''\rangle = |^3P_0'\rangle + \beta_1 |^3P_1'\rangle + \alpha_1 |^1P_1'\rangle. \tag{2.6}$$

This makes doubly forbidden transition $^1S_0 \rightarrow^3 P_0$ ($\Delta S \neq 0$, $J = 0 \rightarrow 0$) weakly coupled. While bosonic isotopes of mercury have nuclear spin equal to 0, as it was mentioned before, hyperfine interaction can be imitated by addition of small static magnetic field. The hyperfine splitting coefficients for mercury were calculated in [45] and for ^{199}Hg isotope they have values of

$$\begin{aligned} \alpha_1 &= 2.31 \cdot 10^{-4} \\ \beta_1 &= -1.21 \cdot 10^{-5}. \end{aligned} \tag{2.7}$$

Note that there is no published uncertainties of these calculations. The $|^3P_0''\rangle$ state can be written as a function of the pure LS-states

$$|^3P_0''\rangle = |^3P_0\rangle + (\alpha_1\alpha - \beta\beta_1)|^3P_1\rangle + (\alpha_1\beta + \beta_1\alpha|^1P_1\rangle = |^3P_0\rangle + \gamma|^1P_1\rangle. \tag{2.8}$$

where $\gamma = \alpha_1\beta + \beta_1\alpha$. The second term in the equation is very small and can be neglected and we consider that the $^1S_0 \rightarrow^3 P_0''$ transition becomes weakly coupled mostly due to the mixed fraction of $|^1P_1\rangle$ state. Then the rate coefficient of the $^1S_0 \rightarrow^3 P_0''$ transition for ^{199}Hg isotope calculated as

$$A_{265} = \frac{8\pi^2e^2}{3\epsilon_0\hbar}\frac{1}{\lambda_{265}^3}|\langle^1S_0|\hat{d}|^3P_0''\rangle|^2 \tag{2.9}$$

here λ_{265} is the wavelength of the $^1S_0 \rightarrow^3 P_0''$ transition and $\hat{d}$ is the dipole coupling operator. Substituting (2.8) in (2.9) we get

$$A_{265} = \frac{8\pi^2e^2}{3\epsilon_0\hbar}\frac{1}{\lambda_{265}^3}\gamma^2|\langle^1S_0|\hat{d}|^1P_1\rangle|^2 = \gamma^2 A_{185}\left(\frac{\lambda_{185}}{\lambda_{265}}\right)^3. \tag{2.10}$$

Here the $|\langle^1S_0|\hat{d}|^1P_1\rangle|$ matrix element was expressed through the rate coefficient A_{185} of the $^1S_0 \rightarrow^1 P_1$ transition using (2.9). Using $A_{185} = 7.46 \times 10^8$ taken from [46] the rate coefficient for $^1S_0 \rightarrow^3 P_0''$ is calculated to be $A_{265} = 0.6\ s^{-1}$. Note that the same rate coefficient was independently calculated by [47] to be $1.3 \times 10^{-2}\ s^{-1}$, which is by a factor of 48 less than the result obtained above. The linewidth of the $^1S_0 \rightarrow^3 P_0''$ corresponding to rate coefficient of $1.3 \times 10^{-2}\ s^{-1}$ is ~ 100 mHz, which corresponds to atomic quality factor of $Q \sim 10^{16}$.

Presence of external magnetic field will remove the degeneracy of the total angular momentum F of the atom. Magnetic field will split energy levels with total angular momentum F in $2F+1$ sub-levels characterized by projection of total angular momentum on quantisation axis

M_F. This is called Zeeman splitting and the energy shift between sub-levels with different M_F is called Zeeman shift. The first order Zeeman shift is proportional to magnetic field

$$\Delta E_{Zeeman} = \mathbf{M} \cdot \mathbf{B}, \tag{2.11}$$

where M is the magnetic moment of atom

$$\mathbf{M} = g_F \mu_B M_F \tag{2.12}$$

g_F is the Lande factor and μ_B the Bohr magneton and M_F is projection of total angular momentum F on axes of magnetic field. Notice that for both states of clock transition $|^1S_0''\rangle$ and $|^3P_0''\rangle$ J=0, which means that an atom in these states has no overall electronic spin nor angular momentum. Therefore the sensitivity to magnetic fields is determined by much weaker interaction with nuclear spin and $g_F\mu_B = g_I\mu_N$, where g_I is the nuclear g-factor and μ_N is the nuclear magneton, which leads to sensitivity to linear Zeeman effect reduced by a factor of ~ 2000. For the ^{199}Hg isotope the nuclear spin is $1/2$ and therefore in external magnetic field each level $|^1S_0''\rangle$ and $|^3P_0''\rangle$ will split into two Zeeman sub-levels with $M_F = -1/2$ and $M_F = 1/2$ (see fig. 2.2) According to selection rules only dipole transitions with $\Delta M_F = 0, \pm 1$ are allowed. This leads to four different transitions between Zeeman sub-levels. Transitions with $\Delta M_F = 0$ are coupled with linearly polarised light, polarisation vector of which is collinear with the magnetic field **B**. These are called π - transitions. Transitions with $\Delta M_F = \pm 1$ are coupled with circular left and right polarisations and called $\sigma+$ and $\sigma-$ transitions (fig. 2.2).

The energy of Zeeman sub-levels in the presence of an external magnetic field B according to (2.11) will be

$$\begin{aligned} {}^1S_0,\ M_F = \pm\frac{1}{2} \qquad & E_{g\pm} = E_g \pm g_F^{ground}\mu_B B/2 \\ {}^3P_0,\ M_F = \pm\frac{1}{2} \qquad & E_{e\pm} = E_g + \hbar\omega_0 \pm g_F^{excited}\mu_B B/2. \end{aligned} \tag{2.13}$$

where ω_0 and E_g are the $^1S_0 \rightarrow ^3P_0$ transition wavelength and $^1S_0$ state energy with external magnetic field equal to zero. The energy difference of excited and ground states in presence of magnetic field for π transitions is

$$\begin{aligned} M_F = \frac{1}{2} \rightarrow \frac{1}{2} \qquad & \Delta E_+ = \hbar\omega_0 + (g_F^{excited} - g_F^{ground})\mu_B B/2 \\ M_F = -\frac{1}{2} \rightarrow -\frac{1}{2} \qquad & \Delta E_- = \hbar\omega_0 - (g_F^{excited} - g_F^{ground})\mu_B B/2. \end{aligned} \tag{2.14}$$

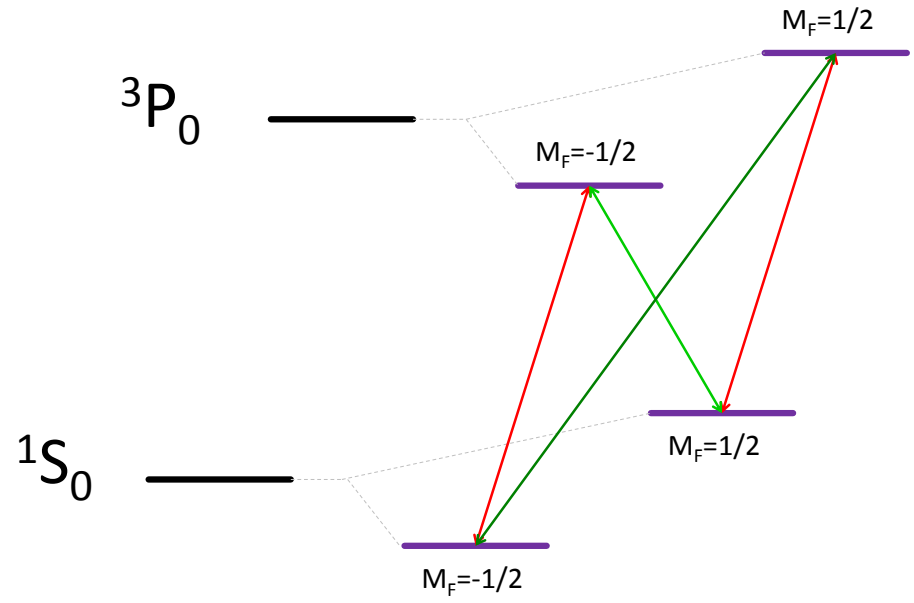

Figure 2.2. *Zeeman splitting of the clock transition in ^{199}Hg and possible transitions between sub-states. The red lines indicate the π transitions, the dark green - $\sigma+$ and the light green - $\sigma-$*

As one can see from (2.14) if $g_F^{excited} = g_F^{ground}$ then $\Delta E_+ = \Delta E_- = \hbar\omega_0$ and both π transitions have same frequency, which is equal to the frequency of unperturbed by magnetic field $^1S_0 \rightarrow^3 P_0$ transition. This is not the case for ^{199}Hg in spite the fact that both $^1S_0$ and $^3P_0$ states have $J = 0$. Due to the hyperfine mixing a small fraction of electronic spin is mixed to the excited state and therefore the Lande factors of the ground and excited states are different by $\delta g = -4.7 \cdot 10^{-4}$ [47]. Thus all four possible Zeeman components of clock transitions (fig. 2.2) will have different frequencies.

2.3.1 Black body radiation sensitivity

One of the main motivation of using mercury in lattice clocks, as it was already mentioned, is the low sensitivity to thermal radiation field. This field is often well approximated by the radiation field of an ideal black-body radiator. Its spectral energy density is given by Planck's

formula

$$\rho_{th}(\nu,T)d\nu = \frac{8\pi h\nu^3}{c^3}\cdot\frac{1}{e^{\frac{h\nu}{k_BT}}-1}d\nu. \tag{2.15}$$

Thermal radiation has a continuous spectrum of frequencies and therefore its average electric field can be calculated as

$$\langle E^2(t)\rangle = \frac{1}{\varepsilon_0}\int_0^\infty \rho_{th}(\nu,T)\,\mathrm{d}\nu = \frac{8\pi^5 k_B^4}{15c^3h^3\varepsilon_0}T^4 = \frac{4\sigma}{\varepsilon_0 c}T^4 \tag{2.16}$$

where σ is the Stefan-Boltzmann constant. For room temperature (T=300 K) this field will be

$$\langle E^2(t)\rangle = (831.9428(15)\,V/m)^2. \tag{2.17}$$

The ac-Stark effect due to the field (2.17) will induce temperature dependent shift of clock transition frequency decreasing stability and accuracy of a clock. This shift can be expressed as [8], [48]

$$\delta\nu_{BBR} = -\frac{1}{2}\frac{\delta\alpha}{h}\langle E^2(t)\rangle\,[1+\eta(T)] \tag{2.18}$$

where $\delta\alpha$ is the differential polarisability between the two clock states and η is a dynamic correction that takes into account the frequency dependence of the state polarisabilities across the BBR spectrum. As one can see evaluation of the $\delta\nu_{BBR}$ requires not only knowledge of the atomic response on the BBR, but also knowledge of the absolute radiation temperature, accurate measurement of which is the actual limiting factor. In order to have sufficient control of the BBR frequency shift one has to cool down the environment of the trapped atoms down to cryogenic temperatures. This was done for example for Strontium clock in [9], but it requires another level of complexity and can limit the future operability of the clock. Low sensitivity to BBR reduces necessary level of temperature control. For instance, since the ac-Stark effect is proportional to the square of electric field (see sec. 2.3.2) and according to (2.16) to the fourth of temperature $\Delta\nu/\nu = k_T T^4$, for neutral mercury BBR shift at room temperature (T=300 K) is calculated to be $\frac{\Delta\nu}{\nu} \approx 1.60\times10^{-16}$ [47] and clock frequency fluctuations induced by BBR will be

$$\frac{d(\frac{\Delta\nu}{\nu})}{dT} = \frac{4}{T}\cdot\frac{\Delta\nu}{\nu} = \frac{4}{300}\cdot 1.6\times10^{-16} = 2.1\times10^{-18}K^{-1}. \tag{2.19}$$

This means that controlling the environment temperature at level of one degree will be enough for mercury lattice clock to reach the relative stability of few 10^{-18}.

2.3.2 Light shift and the magic wavelength

Interaction of an atom with fast oscillating electric fields results in energy shifts of atomic levels and corresponding frequency shifts of lines due to the ac-Stark effect. These shifts are called ac-Stark or simply light shifts. Since the interaction energy with electric fields in general is small, they can be calculated by perturbation theory. A series expansion of the light shift of the energy of a level gives [49]

$$\delta E^{Stark} = -\alpha(\omega_l)\left(\frac{E_l}{2}\right)^2 - \alpha'(\omega_l)\left(\frac{E_l}{2}\right)^4 + O(E_l^6) \tag{2.20}$$

where E_l and ω_l are the amplitude and the frequency of the laser field and $\alpha(\omega_l)$ and $\alpha'(\omega_l)$ are the dynamic polarizability and hyperpolarizability respectively. The resulting frequency light shift of the transition between $|g\rangle$ and $|e\rangle$ levels will be

$$h\delta\nu^{Stark} = -\delta\alpha(\omega_l)\left(\frac{E_l}{2}\right)^2 - \delta\alpha'(\omega_l)\left(\frac{E_l}{2}\right)^4 \tag{2.21}$$

where $\delta\alpha(\omega_l) = \alpha_e(\omega_l) - \alpha_g(\omega_l)$ is differential polarizability. Polarizability of a given state a depends on the dipole moment of the atom $\mathbf{D}$ and electric field $\mathbf{E}$ and can be calculated as

$$\alpha_a(\omega) = \sum_b \frac{|\langle a|\mathbf{D}\cdot\hat{E}|b\rangle|^2}{E_b - E_a - \omega} + \sum_b \frac{|\langle a|\mathbf{D}\cdot\hat{E}|b\rangle|^2}{E_b - E_a + \omega}. \tag{2.22}$$

The sums run across all atomic states $|b\rangle$ that are coupled to state $|a\rangle$ by electric dipole transitions. One can decompose the polarizability for a state $|nFM_F\rangle$ into contributions and write it as

$$\alpha_{nFM_F}(\omega) = \alpha_F^S(\omega) + (\hat{k_l}\cdot\hat{B})\mathcal{A}\frac{M_F}{2F}\alpha_F^V(\omega) + \frac{1}{2}(3|\hat{E}\cdot\hat{B}|^2 - 1)\frac{3M_F^2 - F(F+1)}{F(2F-1)}\alpha_F^T(\omega). \tag{2.23}$$

Here superscripts S, V and T indicate scalar, vector and tensor parts of polarizability. $\hat{k_l}$ and $\hat{B}$ are unit vectors along laser light wave vector and quantization B field respectively and $\mathcal{A}$ is the degree of the light polarisation. $\mathcal{A} = \pm 1$ for $\sigma_\pm$ polarization and $\mathcal{A} = 0$ for linear. For ^{199}Hg isotope $F = 1/2$ and tensor part of polarizability is equal to 0.

Lattice trapping of neutral atoms assumes laser fields of high intensity and significant energy shifts (see sec. 4.2.1), which means that any fluctuations of light intensity will be transmitted into a frequency fluctuations. However, as one can see from (2.3), polarizability depends on the wavelength and there is a possibility that exists such

wavelength at which polarizabilities of excited and ground states of a clock transition will be exactly the same. In this case the light shift is

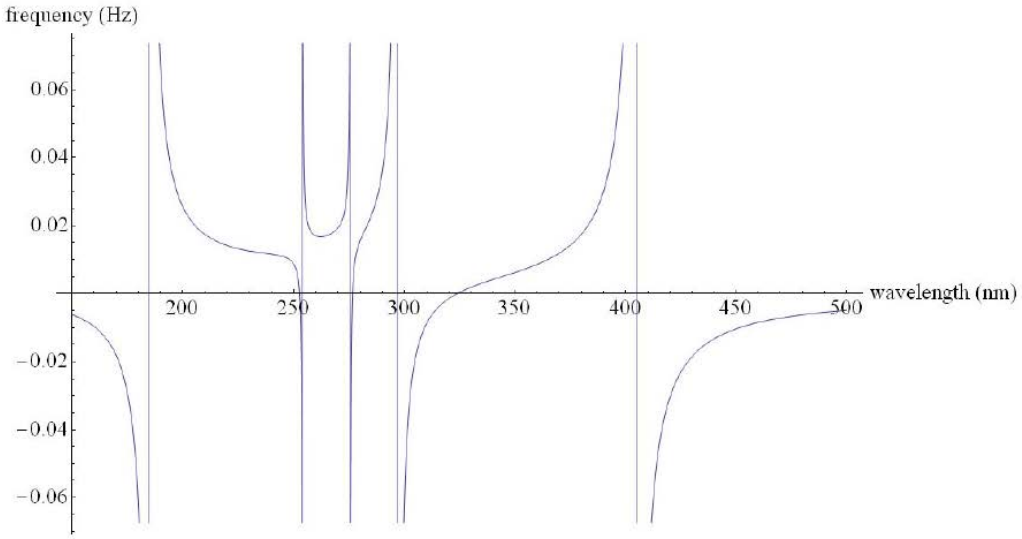

Figure 2.3. *Theoretical estimation of the Hg clock transitions light shift due to a dipole trapping laser field as a function of the laser wavelength. The figure is taken from [44].*

equal to 0 and the field of the lattice trap does not perturb the transition frequency any more (see fig.2.3). This wavelength is called the magic wavelength [33]. It worth to mention, that polarisability at the magic wavelength can be both positive and negative, which leads to two different cases. For the case when $\alpha > 0$, $U_0 < 0$ and atoms are attracted to maxima of the local intensity. Trapped atoms form layers of pancake-like clouds separated by $\lambda/2$ in the axial direction (see eq.1.3). In case when $\alpha < 0$ atoms are pushed to the minima of local intensity, which means that they will escape a 1D lattice trap along the radial direction. In this case atoms can be trapped only in 3D optical lattices.

Theoretical calculations predicted existence of the magic wavelength, which were after experimentally measured for Yb [8], Sr [50]. For mercury, calculations predicted magic the wavelength to be 360 nm [47]. In 2011 LNE-SYRTE made the first experimental determination of the magic wavelength [51], which was later refined in 2012 to $\lambda_m = 362.5697 \pm 0.0011$ nm [39]. In these experiments the wavelength of the lattice light was tuned to acquire several values close to the expected magic number and for each wavelength the center frequency of the clock transi-

tion was measured at different trap depths. The magic wavelength was determined as the one at which the frequency of the clock transition had the smallest dependency on the lattice light intensity.

It is common to express the depth of an optical lattice trap in terms of recoil energy

$$E_{recoil} = \frac{1}{2m_{at}}\hbar^2\left(\frac{2\pi}{\lambda_l}\right)^2 = \frac{h^2}{2m_{at}\lambda_l^2} \tag{2.24}$$

where m_{at} is the atom mass and λ_l is the wavelength of the lattice light. In the experiments presented in [39] the trap depth was limited by the amount of available lattice light and had maximal value of 20 recoil energies, which corresponds to a very shallow trap. For comparison, typical trap depths of Yb and Sr lattice clocks lie in the range of $100-150$ recoil energies.

From what was said above we can conclude that mercury has a good cooling transition, that allows to cool atoms down to 30 μK, a favourable clock transition with simple level structure and $Q \sim 10^{16}$, and the most important - low sensitivity to BBR. Mercury as well has low lattice-induced light shift of the clock transition due to hyper polarisability (2 orders of magnitude lower than for Sr and Yb [[52]]). All this makes mercury a very promising candidate for lattice clocks able to provide relative accuracy and stability below 10^{-18}. Nevertheless, mercury was the latest to be used in lattice clocks. The reason for this is the complexity of the laser systems that have to be used on the experiment. Cooling, trapping and probing of mercury requires relatively powerful laser systems with wavelengths in the deep UV.

Chapter 3

Experimental setup

There are not many laser systems, that are able to generate CW laser light in UV domain with tunable frequency. The situation becomes even more challenging if one needs light sources with high power (hundreds mW) and relatively narrow linewidth. To our knowledge the only way to generate such laser light at the wavelengths mainly used in our experiment ($\lambda_{cooling} = 253.7$ nm, $\lambda_{clock} = 265.6$ nm, $\lambda_{lattice} = 362.5$ nm) is to use infrared laser sources along with frequency doubling techniques. In this chapter, I will describe our experimental setup including main laser systems and the vacuum chamber. This chapter describes the state of the experiment at the beginning of my PhD work and almost everything that is mentioned here was done and implemented before, while the chapter 4 describes the work and improvements of the experimental setup that I performed during my work on the project.

3.1 Cooling light laser source at 253.7 nm

The cooling laser system is the most problematic part of the experiment and is very hard to operate. For the normal operation of the experiment with desired performance this laser system has to generate at least 200 mW of light at 253.7 nm wavelength. To generate such an amount of power we use powerful infrared light laser source followed by two frequency doubling stages. Scheme of the whole cooling laser system is shown on figure 3.1.

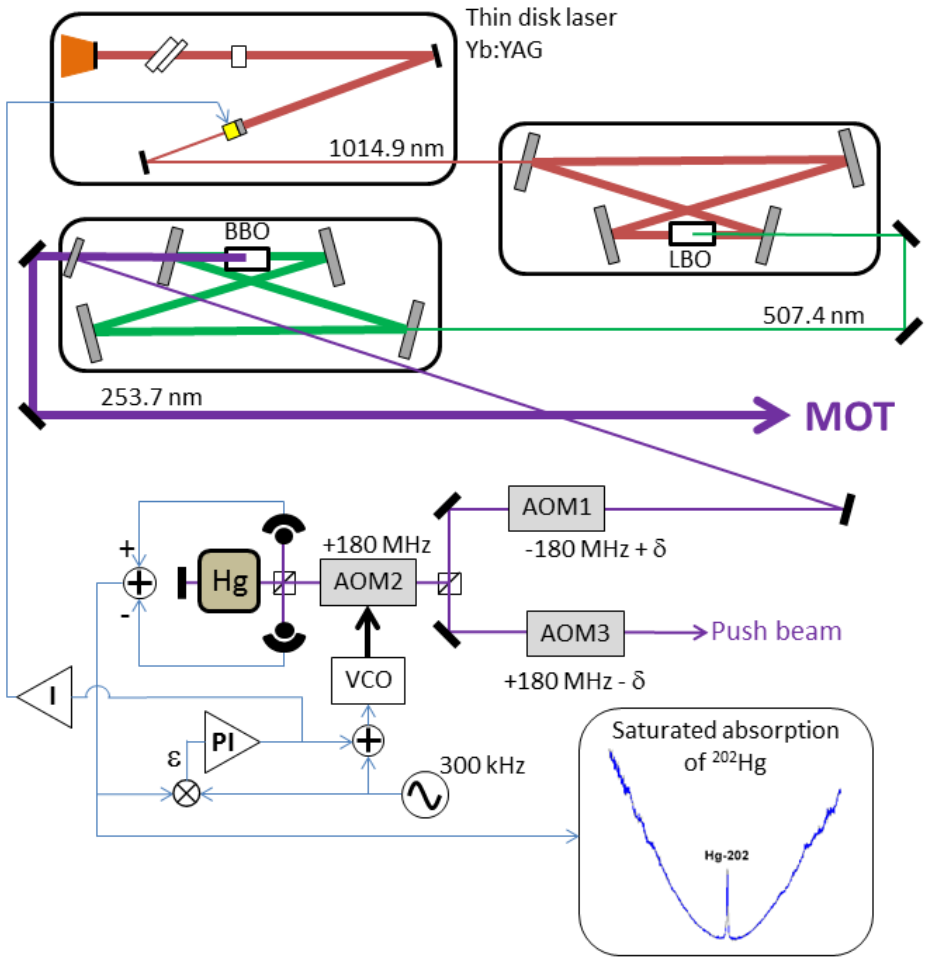

Figure 3.1. *Scheme of the cooling laser source. The laser source is based on a commercial thin-disk laser with subsequent two stages of frequency doubling in external bow-tie cavities with non-linear LBO (507 nm) and BBO (254 nm) crystals. You can also see an auxiliary UV beam that is used in the frequency stabilisation scheme (at the bottom of the figure) based on a saturated absorption in a Hg vapour cell and for a push beam, that is used in state selection (sec. 5.3). See text for more details.*

3.1.1 Yb:YAG thin-disk laser

The infrared laser source has to be quite powerful since the efficiency of the second harmonic generation in general is low. It was chosen to use a commercially available Yb:YAG crystal thin-disc laser (Versadisk) from ELS. The active medium or this laser is a $240\ \mu m$ thick and 10 mm diameter disk of Yb:YAG crystal. The back side of the disk has high-reflective coating and acts as one of the mirrors of the ring cavity of the laser. This system is pumped by up to 100 W of 938 nm light from diode arrays. This light is sent to a parabolic mirror. The light is reflected from the parabolic mirror and hits the crystal 24 times. The crystal is opposite to the parabolic mirror and the substrate of the crystal has high reflective (HR) coating. The nominal operation point of the laser system is at 1030 nm with 50 W of output power. Before the beginning of my thesis this laser system was modified to operate at 1014.9 nm with available output power of 8 W. Unfortunately being used in not optimal configuration the laser system became less stable and harder to operate. The modifications of the Versadisk were done considering not only the shift of the output light frequency but also the possibility to tune it in a controllable way over a range of several tens of picometers, corresponding to the shift of clock frequency of all the stable isotopes of mercury. Frequency tuning was implemented by the means of an etalon installed in the cavity (see fig. 3.2).

The etalon is a round, 5 mm thick plane-parallel temperature stabilized slab of fused silica. By tuning the temperature of the etalon one can shift the frequency of the laser system. To avoid temperature gradients transverse to the light beam the etalon is mounted on a doughnut shaped peltier element. Detailed description of the modified system can be found in [44].

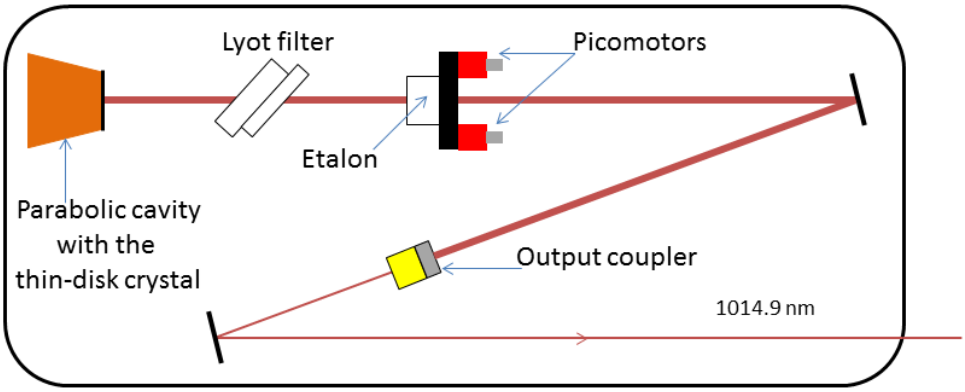

Figure 3.2. *Versadisk cavity scheme. Most parts of the laser's cavity and disk itself are shown as the brown trapezium on the left and on the figure one can find only the output coupler, mounted on a PZT driver and a Lyot filter with an etalon that are used for frequency selection and control. The etalon is a 5 mm thick plane-parallel slab of fused silica that is temperature stabilized and mounted on two picomotors.*

3.1.2 Frequency doubling stages

Second harmonic generation (SHG) can be realized in a non-linear medium, typically an uniaxial crystal. The phenomenon of second harmonic generation is based on the fact, that electromagnetic wave interacts with atomic or molecular systems in a dielectric medium inducing microscopic dipoles. Under weak incident electric field E, the induced polarization $P(E)$, which is the sum of all microscopic dipoles, has linear dependence E and all dipoles oscillate with the same frequency ω as the incident electromagnetic wave. In fact in general polarisation is non-linear and can be written as

$$P(E) = \epsilon_0(\chi^{(1)}E + \chi^{(2)}E^2 + \chi^{(3)}E^3 + \dots), \tag{3.1}$$

where $\chi^{(i)}$ are the susceptibilities, which usually become smaller with increase of i. This means that there will be dipoles that are oscillating at frequencies of the second, third etc. harmonics. These dipoles will generate electromagnetic waves correspondingly at 2ω, 3ω etc. In the optical domain non-linear effects are very small and show up only at high intensities of the light. More information about second harmonic generation can be found in [53].

The first frequency doubling stage of the cooling laser is a commercial system supplied with the Versadisk. It uses a 15 mm long 90° cut

LBO (Lithium triborate) crystal as a non-linear medium. In order to increase the efficiency of SHG the crystal is put inside a bow-tie cavity. The crystal is kept at around 210 °C to fulfil the phase matching condition ([53]). The length of the cavity is locked by an electronic system, in order to keep the SHG at maximum efficiency. This electronic system, supplied together with the Versadisk, uses the Hänsch-Couillaud locking method [54]. With an input of 8 W at 1014.9 nm the doubling stage is able to generate up to 3 W of 507 nm light.

The second frequency doubling stage is also implemented in a bow-tie cavity but with BBO (Beta barium borate) crystal as a non-linear medium. The BBO crystal is the only known crystal transparent at the wavelength of our cooling transition, which is able to generate sufficient amount of UV light. Therefore we had no other choice, but to use this crystal in our laser system. We are using a 7 mm long Brewster cut crystal with uncoated surfaces, this configuration was preferred to a 90 degrees cut coated crystal due to damage of coatings induced by the UV light. It is worth noting, that due to the spatial walk-off effect (walk-off angle 4.8° at 285 nm) [55] a longer crystal would lead to an unpractically elliptical beam.

The output coupler of the cavity is AR coated at 254 nm in order to let all generated UV light leave the cavity. A small amount of UV light is being picked off at the output of the cavity and sent on a photo diode. Using the signal from the photo diode we lock the cavity on a side of the resonance peak, which allows us to easily change the output power by changing the offset of the side lock. The second doubling stage is able to generate up to 800 mW of UV light with 3 W of 507 nm light. However, we were able to operate this system only at 50-70 mW output power because of the crystal and optics damage due to exposure to high power UV light (see more in sec.4.1.2).

3.1.3 Frequency lock on saturated absorption

As it was mentioned in chapter 1 the Doppler effect is the largest contribution to spectral broadening of lines in the optical frequency domain, and has to be suppressed. A simple technique to perform laser spectroscopy of an atomic transition suppressing the broadening induced by the Doppler effect is non-linear saturation spectroscopy. The idea of this method is to use two spatially overlapped counter propa-

gating laser beams passing through an atomic vapour. If the laser light frequency ν is blue detuned by δ from the transition frequency ν_0 then the light will interact with a group of atoms with velocities v such that $\delta = \vec{k} \cdot \vec{v}$ transferring them into the excited state and forming a hole in the ground state velocity distribution. The counter propagating light beam will also form a hole in the ground state velocity distribution, but for velocity $v\prime = -v$. If $\delta = 0$ then both laser beams will interact with the same group of atoms for which $\vec{k} \cdot \vec{v} = 0$, in other words atoms, that are moving perpendicularly to the light beams and experience no first-order Doppler shift. In this case if one of the beams saturates the transition, light of the second beam will be absorbed less. This will lead to appearance of a narrow dip in the Doppler profile of the transition scanning laser light frequency across the resonance (see fig.3.3). The laser system can be locked on this narrow dip free from the Doppler broadening. More details about saturated absorption locking can be found in [13].

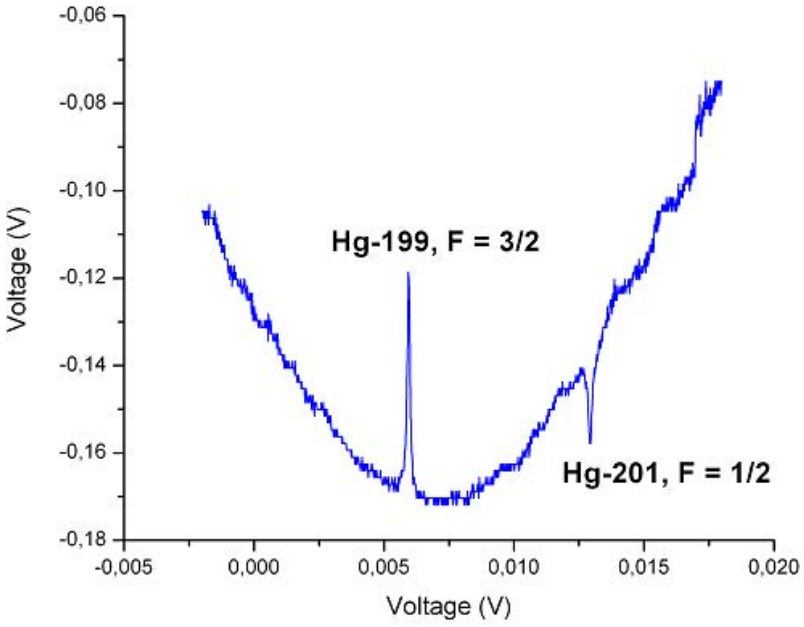

Figure 3.3. *Saturated absorption spectroscopy. The figure is taken from [44]*

The scheme of our saturated absorption lock is shown on the figure 3.1. In order to devote all available power to cooling and trapping

of atoms and to not send too much UV light through acousto-optic modulators (AOM) we use a rather weak auxiliary light beam for saturated absorption and locking the frequency of light to the transition via PZT of the Versadisk cavity. About 7.5% of the main output beam is reflected from an uncoated UV grade fused silica beam sampler and sent first to a prism, to separate second harmonic from fundamental light, and then to a mercury vapour cell through a set of AOMs. Frequency of the first AOM is 183.7 MHz and controlled by PC to detune the laser system from the cooling transition frequency. Second AOM is used to form a push beam pulses. It also compensates for the push beam's frequency detuning of -1.5Γ from the frequency of cooling transition, which is introduced by the first AOM (see fig.3.1). Frequency lock of the laser system is implemented in two nested feedback loops. First the third AOM is being locked to the saturated absorption signal with proportional-integral lock by homodyne detection with a 300 kHz modulation frequency. Then the correction signal of the first lock is taken as the input of the second loop, integrated one more time and sent to the feed forward unit. Feed forward unit in turn sends this signal to the PZTs of Versadisk and both doubling cavities with different gains to frequency lock the laser system. Using feed forward helps doubling cavities to follow the changes of the Versadisk cavity while staying locked. The resulting linewidth of the locked laser system is not more than 64 kHz in UV[44], which is smaller than the natural linewidth of the cooling transition (1.3 MHz).

3.2 Magneto-optical trapping of neutral mercury

Atoms in a cloud or a thermal beam have relatively high temperatures and therefore high kinetic energy. The typical depth of lattice traps is very small in comparison to kinetic energy of atoms even at room temperature and therefore atoms can not be trapped. First atoms have to be cooled down to temperatures of the order of $100\mu K$, forming a cold atomic sample, which then can be loaded into a lattice trap. The most efficient way to cool atoms to such temperatures is to use laser light. Two overlapped counter-propagating laser beams with frequency red-detuned from the frequency of an appropriate transition in atom will create a damping force that depends on the atom's veloc-

ity. This force will decelerate atoms along the direction of propagation of laser beams. Intersection of three perpendicular pairs of such laser beams is called optical molasses. Atoms in optical molasses are cooled down to low temperatures, but are not confined in space. Adding a quadrupole magnetic field and using circularly polarised laser beams removes space isotropy and create a force that depends on the magnetic field gradient. This force will push atoms towards the center of the trap, where magnetic field is equal to zero [13]. All components have to be put in a vacuum to avoid heating of the atoms due to collisions with hot background gas. This is called magneto-optical trap (MOT).

3.2.1 Vacuum system

Vacuum chamber of our experiment is shown on the figure 3.4. The vacuum chamber consists of two parts. The first part is composed of a mercury vapour source and a 2D-MOT. The source is a droplet of mercury kept in a copper tube cooled down to $\approx -40°$C with the help of a Peltier element. Being at $\approx -40°$C is low enough to produce a vapour pressure of order of $\approx 10^{-6}$ mbar (see fig. 2.1). 2D-MOT is

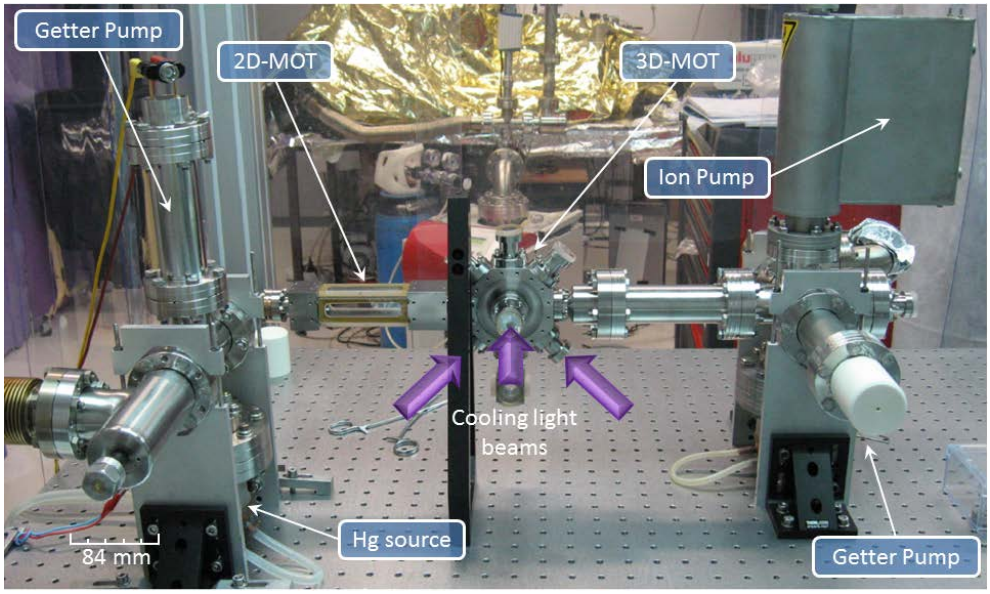

Figure 3.4. *Picture of the vacuum chamber of the experiment. The picture shows vacuum chamber alone without experiment optics (lattice cavity is not presented on the picture). Three cooling light beams access the chamber as it is shown on the picture and then are retro-reflected to form the 3D MOT.*

a chamber that is used to pre-cool atoms, compressing them in the radial direction of the thermal beam. The second part consists of a 3D-MOT and a lattice trap. The 3D-MOT chamber has six openings through which the cooling light access atoms inside the chamber (see the figure) and two more openings, one at the bottom and one at the top, for the vertically oriented lattice trap. The lattice trap is created by a vertical standing wave in a build-up Fabry-Perot cavity formed with two high reflective curved mirrors (not shown on fig.3.4, see more in sec.4.2). The two parts of the vacuum chamber are separated by a 1.5 mm diameter tube (fig. 3.5), which forms an atomic beam while at the same time creating a differential vacuum of about three orders of magnitude between the two parts of the chamber. Resulting vacuum level in 3D-MOT chamber is 10^{-9} mbar. Detailed information about vacuum chamber of the experiment can be found in [44].

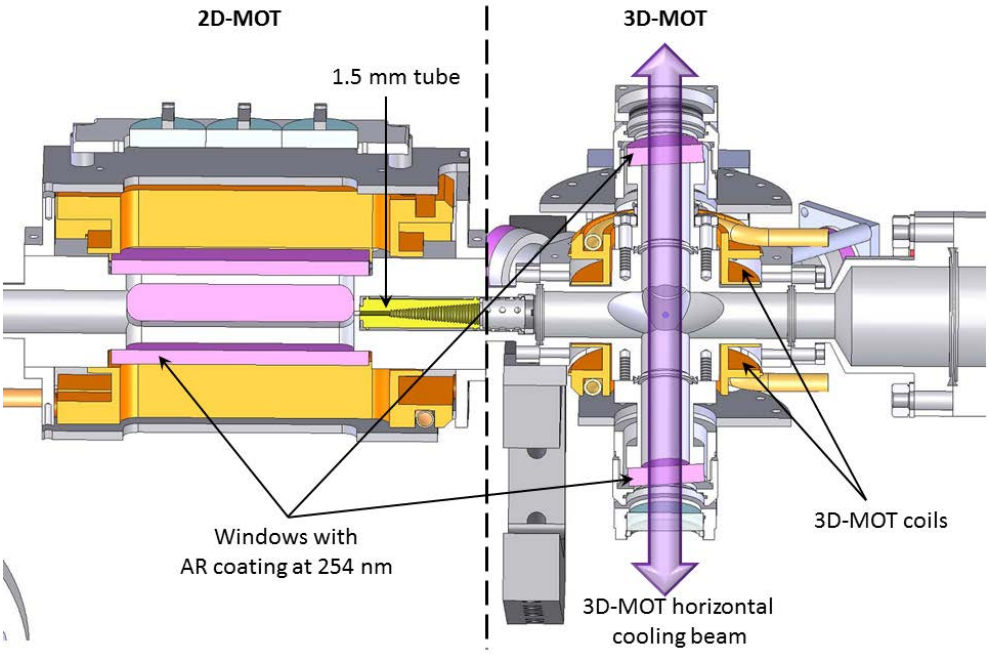

Figure 3.5. *Cut of the vacuum chamber of the experiment in the horizontal plane. You can see 2D-MOT and 3D-MOT separated by the dashed line. On the figure you can find as well the ⌀ 1.5 mm tube that separates 2D-MOT and 3D-MOT chambers.*

The high efficiency of 2D-MOT was demonstrated in [44]. It was measured that use of 2D-MOT increases number of trapped atoms at least by 400% in comparison to trapping from a thermal beam. Unfortunately the amount of light that our cooling laser system is able

to provide on a daily basis is not enough for simultaneous operation of 2D and 3D MOTs. All the experiments discussed below were done without 2D-MOT.

3.2.2 Detection scheme

Detection of trapped atoms in the experiment is done with the help of actively cooled low noise electron-multiplied (EM) CCD camera. The camera detects fluorescence of atoms at 254 nm. Scheme of the detection is shown on the figure 3.6.

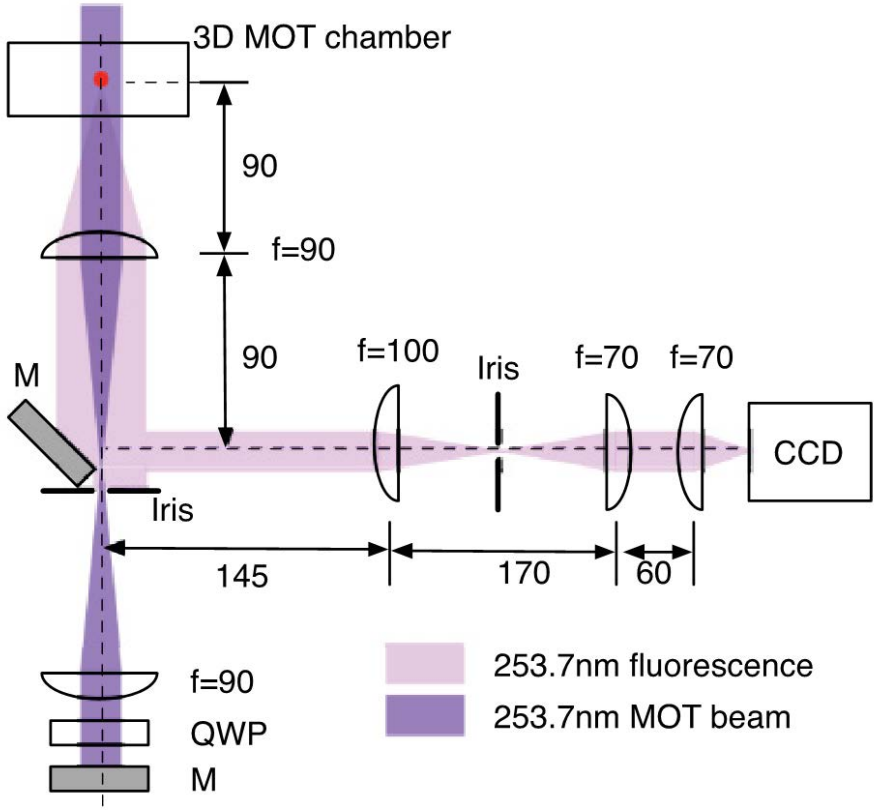

Figure 3.6. *Detection scheme of the experiment. Red dot marks the trapped atoms position. The figure is taken from [56].*

As you can see from the figure, the detection is done on the same axis as the horizontal MOT cooling beam. The cooling light and fluorescence of atoms are spatially separated. By a set of lenses cooling beam is focused to a pinhole that is used to filter possible multiple reflections from the lenses and vacuum chamber mirror. After the pin-

hole the MOT beam is retro-reflected from a mirror and sent back to the vacuum chamber by exactly the same path through the pinhole.

The fluorescence of atoms is collimated by the same set of lenses. Fluorescence from the half of accessible solid angle is reflected by a half-cut mirror at 45° and sent to the CCD camera through an iris, that is used to filter background light, which is not coming from the trapped atoms site.

Absolute number of trapped atoms is calculated based on the number of counts of the CCD camera. In our experiment one count equals to 11.9 electrons, registered by the CCD. Number of electrons registered by CCD depends on the number of photons that hit the matrix of the camera.

$$N_e = G\eta N_{photon} \tag{3.2}$$

where $G = 50$ is the electron-multiplying gain and $\eta = 0.3$ is the quantum efficiency of the CCD matrix. The number of photons emitted by one atom, that hit the matrix of the CCD during the detection is calculated as

$$N_{photon} = R_{emis} T_{exp} \Omega. \tag{3.3}$$

Here R_{emis} is the emission rate of the atom, $T_{exp} = 9$ ms is the time of exposure of the CCD camera, $\Omega = 1/4(1 - \cos(\theta))$ is the solid angle from which photons are collected. θ was calculated as $\arctan(11.5/90)$, where 90 mm is the distance from trapped atoms to the first lens (see fig.3.6) and 11.5 mm is the radius of the lens. The emission rate of the atom is calculated as

$$R_{emis} = \frac{\Gamma}{2} \frac{S}{1+S}. \tag{3.4}$$

Here $\Gamma = 8$ MHz is the cooling transition linewidth and S is the saturation parameter

$$S = \frac{I/I_s}{1 + 4\delta^2/\Gamma^2}. \tag{3.5}$$

Here I is the intensity of the cooling light and δ its frequency detuning from the cooling transition. I_s is the saturation parameter

$$I_s = \frac{2\pi^2 \hbar c \Gamma}{3\lambda^3}. \tag{3.6}$$

Amount of CCD counts per atom depends on the detuning and intensity of the cooling light. For typical detuning during detection $\delta = -1.5\Gamma$ and cooling light intensity $I \approx 40$ W/m^2 we have 3.3 counts per one atom.

Our detection scheme also has real-time image processing with background cancellation and it was characterized to have noise floor of ~ 40 atoms (see [57]).

3.2.3 Experiment operation cycle

As it was already mentioned the ${}^1S_0 \rightarrow {}^3P_1$ transition in mercury has good properties and is used for cooling and trapping in MOT. Trapping of atoms in our experiment can be divided into three phases (fig.3.7). First phase is called "loading phase" and it takes the biggest

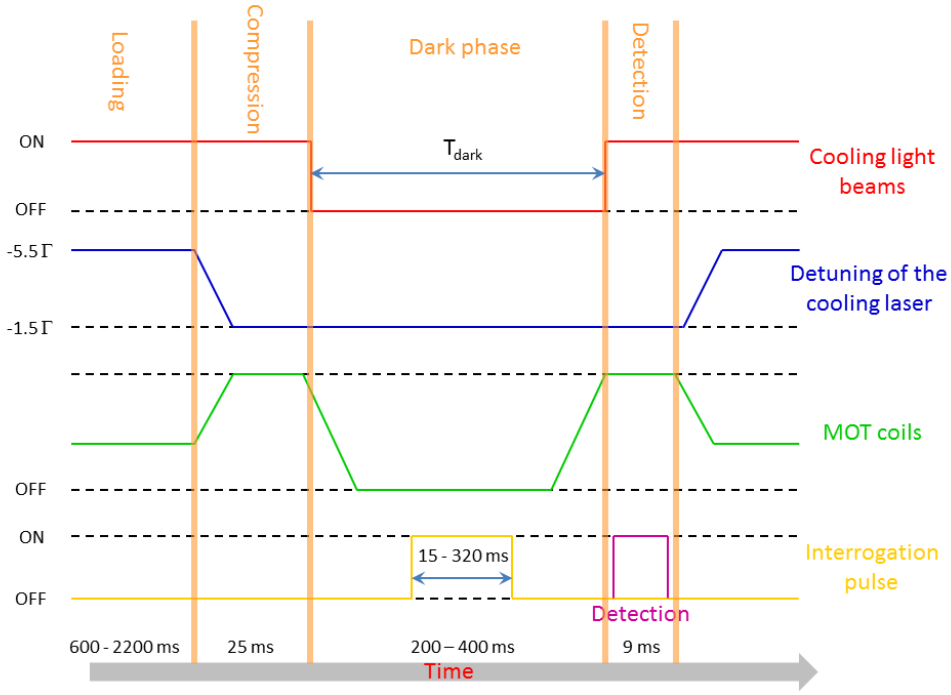

Figure 3.7. *Scheme of the time sequence of the main operation cycle of the experiment. The operation cycle is divided in four phases, separated on the scheme by vertical lines. Duration of the loading and dark phases as well as duration of the probe pulse could be varied depending on goals of performed experiments.*

part of the duty cycle. During this phase atoms from the low velocity tail of Maxwell-Boltzmann distribution at room temperature (by this time atoms were already thermalized via collisions with walls of the vacuum chamber) are cooled down and captured in the MOT. Cooling light in this phase is red-detuned from the resonance by $5.5\ \Gamma$, which corresponds to the highest loading efficiency. Duration of this phase

depending on the goals was varying between 600 and 2200 ms. Typical duration of this phase in the experiments presented in this thesis is 900 ms, during which about $\sim 6 \times 10^5$ atoms are trapped in the MOT. The second phase is the "compression phase". In this phase the detuning of the cooling beams changes with a linear ramp from $5.5\ \Gamma$ to $1.5\ \Gamma$ along with the increase of magnetic field gradient. As a result the cloud of atoms captured in the MOT during loading is further cooled down and compressed in size. This phase lasts for ≈ 25 ms. The third phase is the "Dark time" phase. It lasts for 200 ms during which the cooling light and the MOT coils are turned off and atoms are released. Atoms with energies smaller than the depth of the lattice trap are being captured in it (see ch. 4.2.1) and the rest of the MOT cloud expands and leaves the trap area. After that an interrogation pulse is being applied. The last phase is the "detection phase". In this phase MOT coils and 2 out of 3 cooling light beams are turned back on and atoms are being detected by CCD camera. We kept horizontal MOT cooling beam turned off during the detection in order to avoid stray cooling light from multiple reflections on optics going to the CCD camera. The CCD exposure time in all experiments described in this thesis was 9 ms.

Typical duration of a clock cycle in the experiments presented in this thesis was 1.1 s and the lattice trap was on during the whole clock cycle.

3.2.4 MOT temperature and lifetime

Cooling and trapping in MOT of fermionic (^{199}Hg ,^{201}Hg) and bosonic (^{200}Hg,^{202}Hg) isotopes was demonstrated in [58]. Temperature and size of the MOT cloud can be estimated from the ballistic expansion of the cloud. Time sequence of the duty cycle of this experiment is shown on fig.3.8. Atoms are being loaded, cooled down and compressed in the MOT, then cooling light is turned off and the MOT cloud is released. After of a certain release time T_R two out of the three orthogonal pairs of cooling beams are switched back on to perform the detection. By cycling this sequence and incrementing the release time a series of images is generated that records the ballistic expansion of the MOT cloud in the detection plane, which is the x-y plane of the coordinate system with 0 at the center of the MOT and z axis along the axis of the

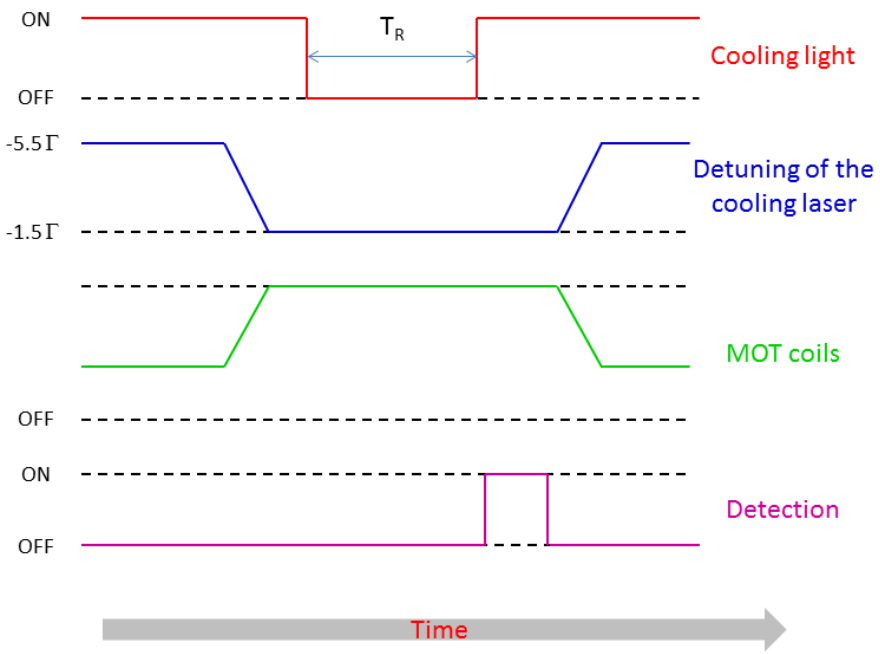

Figure 3.8. *Scheme of the time sequence of the MOT temperature and size measurement experiment. After loading and compressing phases MOT cooling beams are turned off and atoms are released. After time T_R released atoms are detected. The time T_R is incremented from cycle to cycle which allows to record ballistic expansion of the atoms cloud.*

MOT coils. The MOT cloud profile is fitted with two one dimensional Gaussians

$$f(x,t) = \exp\left[-\frac{x^2}{2r_k^2(t)}\right] \tag{3.7}$$

from where the rms radii $r_x(t)$ and $r_y(t)$ are calculated (see fig.3.9).

The sequence of cloud radii $r(t) = r_x^2(t) + r_y^2(t)$ for different release times T_R is measured. These measurements are fitted by

$$r^2(T_R) = r_0^2 + \left(\frac{k_B T}{M}\right) T_R^2 \tag{3.8}$$

where k_B is the Boltzmann constant, M is the atomic mass, T is the temperature of atoms and r_0 is the size of the cloud before the release. From the interception of the fit line with the y axis at $T_R = 0$ the initial rms radius r_0 is measured. The temperature T of the MOT cloud is determined based the slope of the fit line evaluated (see fig.3.10). In all the experiments described in this thesis typical MOT cloud radius was $r_0 = 110$ μm and MOT temperature $T = 70$ μK.

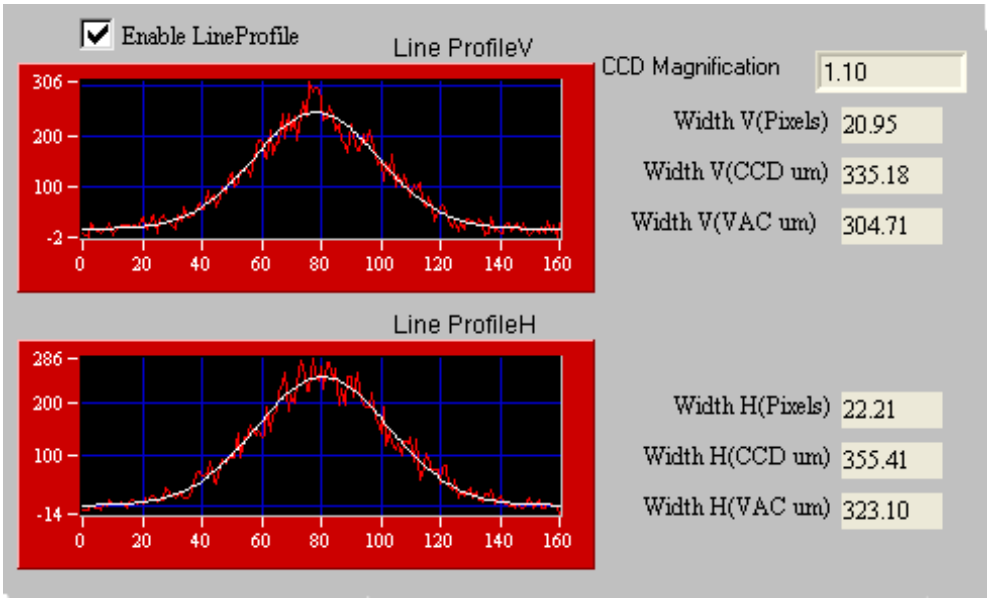

Figure 3.9. *^{199}Hg MOT cloud size measurement in x (top) and y (bottom) directions based on the CCD image. White line is the fit with the equation (3.7).*

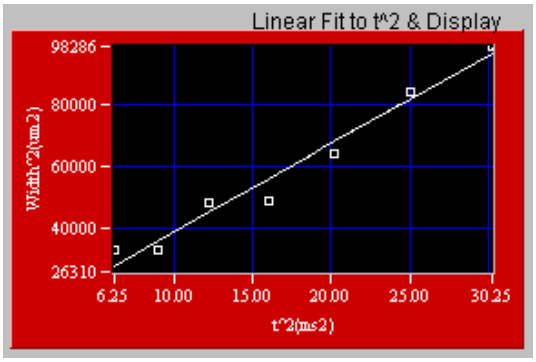

Figure 3.10. *Square of the ^{199}Hg MOT cloud size (μm) versus square of the release time T_R (ms). White line is the fit of the data with the equation (3.8).*

Atoms trapped in the MOT have a finite lifetime. This lifetime at relatively low densities of the MOT cloud is assumed to be mainly determined by loss of atoms due to collisions with hot background gas. The number of atoms in the MOT can be described by a rate equation [59]

$$\frac{\partial N}{\partial t} = R - \Gamma N \tag{3.9}$$

where R is the rate at which atoms are being trapped in the MOT and Γ is the loss-rate. The solutions of (3.9) for loading $(N(0) = 0)$ and de-loading $(R = 0)$ cases have the form of $A(1 - \exp\left[-\frac{t}{\tau}\right])$ and

$B \exp\left[-\frac{t}{\tau}\right]$ correspondingly, where $\tau = 1/\Gamma$. In order to estimate the time constant τ of these solutions the signal from the MOT cloud was monitored, while the duration of the loading phase was increased from shot to shot. The resulting loading curve (see fig.3.11) was fitted with $A(1 - \exp\left[-\frac{t}{\tau}\right])$.

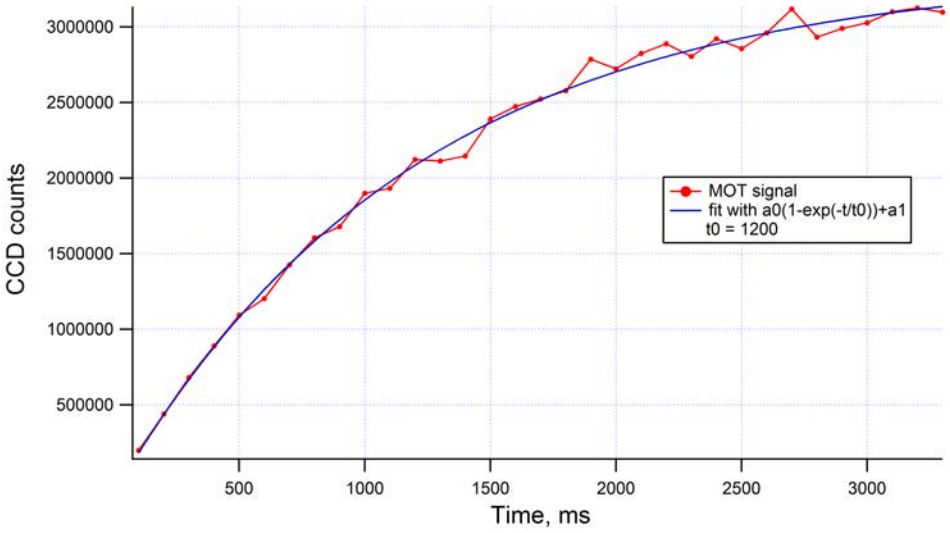

Figure 3.11. *^{199}Hg MOT atoms signal vs loading phase duration. Blue line is fit of the data with equation $A(1 - \exp\left[-\frac{t}{\tau}\right])$. From the time constant of the fit life time of atoms in the MOT is estimated to be ~ 1.2 s.*

All the experiments below are performed with ^{199}Hg isotope. The ^{199}Hg isotope was chosen due to its fermionic nature and thus low collisional shift, and, in comparison with the second fermionic isotope ^{201}Hg, higher abundance and lower nuclear spin (see table 2.1). Typical "working" parameters of the ^{199}Hg MOT cloud are $T \approx 70$ μK, $r_0 \approx 110$ μm and the MOT lifetime $T_{MOT} = \tau \approx 1.3$ s

3.3 Ultra-stable light laser source at 265.6 nm

To make a frequency standard one needs to have a local oscillator (see ch.1), whose frequency will be compared to the reference, and in our case it is a laser system. To exploit full potential of the reference, this laser system has to have a linewidth not bigger than the linewidth of the atomic reference transition and be ultra-stable in frequency. Quick description of our ultra-stable laser system is given below, while more information and details can be found in [44].

Wavelength of our clock transition is 265.6 nm and, as in case of cooling light, we have to start from infrared light and frequency double it twice. Full scheme of the probe light laser system one can find on figure 3.12. Light at 1062 nm was generated by a commercial fiber

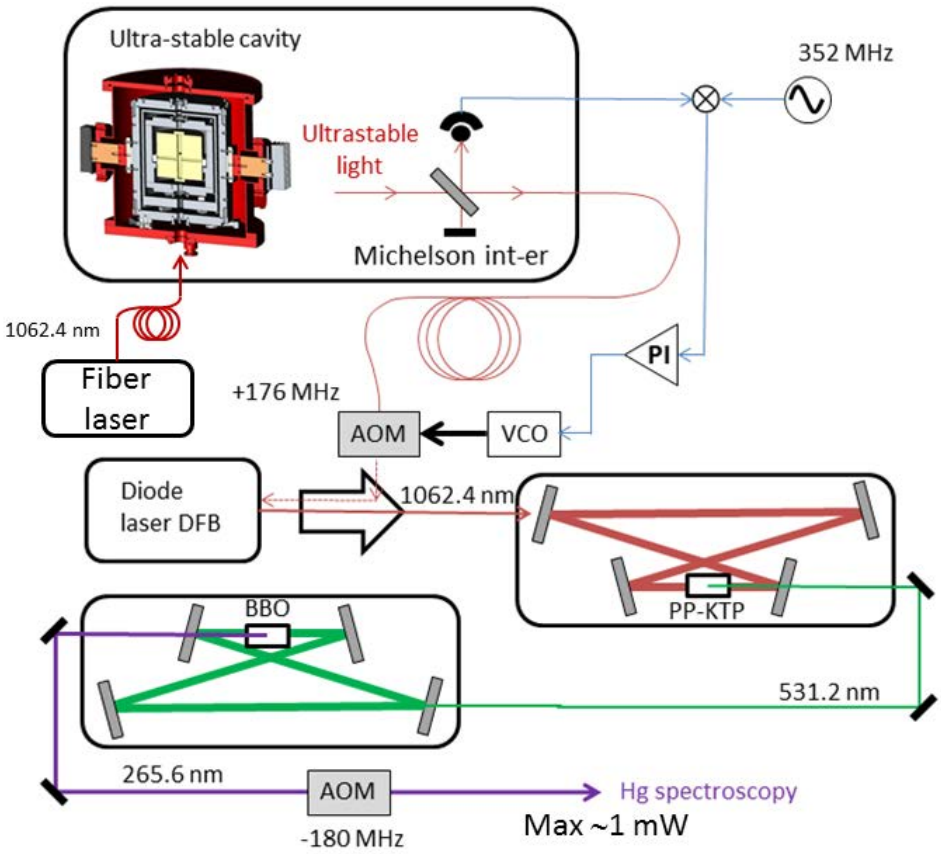

Figure 3.12. *Scheme of the ultra-stable laser source. The laser source is based on a commercial fiber laser locked to a 10 cm long ULE cavity. Part of the ultra-stable light generated by the fiber laser is used to injection lock a DFB diode laser. Light of the DFB laser is frequency quadrupled in two SHG bow-tie cavities with ppKTP (531 nm) and BBO (265 nm) non-linear crystals.*

laser, which was locked to a 10 cm long ultra-stable cavity (USC) using Pound-Drever-Hall locking technique [60]. The cavity is made from ultra-low expansion glass with optically contacted fused silica mirrors. Finesse of the cavity is estimated to be ~ 850000 and to achieve high stability the cavity has several thermal, vibration and acoustic isolations. Linewidth of the laser locked to the ultra-stable cavity is estimated to be ~ 170 mHz and the flicker floor $\sim 3 \cdot 10^{-16}$. Infrared

light of the locked fiber laser was sent to the main optical table and to the fiber comb in the neighbour laboratory via optical fibers. The light that propagates through an optical fiber acquires frequency noise induced by the fiber length fluctuation due to temperature changes. In order to suppress this noise both links were frequency stabilized. To stabilise the links a Michelson interferometer was made (see fig.3.12). The reference arm of the interferometer was a short distance between a PBS and a retro reflecting mirror. The long arm was the path that light did from the PBS to the end of the links, where small amount of it was reflected, and sent all the way back. Each link had an AOM installed on the path of the light therefore the registered beatnote of the two interferometer arms was at twice the frequency of the AOMs. This beatnote signal was later mixed with the references generated by the sum of DDS and synthesizers and the result of the mix was filtered by a passband filter leaving only the difference component. The AOMs were phase locked to the difference, compensating all the frequency noise induced by the fiber links. Each link had its own reference synthesizer stabilized to 10 GHz, that were mixed with the common DDS. The frequency of the DDS was 106 MHz and was changed linearly with time by a software in order to compensate for the drift of the USC, which value was slowly changing with time around ≈ 20 mHz/s (this is a fundamental drift that comes from a deformation of the cavity spacer due to gravity). The reference synthesizer of the fiber link to the experiment was controlled by PC and used to sweep the frequency of the probe light during spectroscopy experiments with resolution of 1 mHz.

To have sufficient amount of power we used a DFB semiconductor laser as a slave laser that was injection locked to the ultra-stable laser source. Light from the DFB laser was frequency doubled twice in two frequency doubling stages of similar configuration as the one that were used in cooling light laser system. First frequency doubling is done in ppKTP crystal and the second one in BBO crystal. After the second doubling stage light was sent to computer controlled AOM, which was used to form probe light pulses of desired length and power.

3.3.1 Probe beam spatial filtering

Due to walk-off effect in the BBO crystal [53] our probe beam had a rectangular like shape with several dark stripes crossing it. As a

result of such beam shape atoms in different places will see different intensities of the probe light. Therefore same probe pulse will have different Rabi frequencies for different atoms, which will decrease the excitation efficiency. To improve the shape of our probe beam we have installed a spatial filter. This filter was realized by putting a converging lense with focal length of 90 mm after the AOM to focus the probe beam to the waist of 16 μm and let it pass through a pinhole with diameter of 10 μm. By performing such spatial filtering we lose in power a factor of ≈ 4, but gaining nice Gaussian shape (see fig.3.13). After the pinhole probe light was sent through a set of lenses to the trapped atoms site. Probe beam was aligned with the optical lattice and entered the vacuum chamber through the top lattice cavity mirror. Polarisation of the probe light was linear and aligned with the

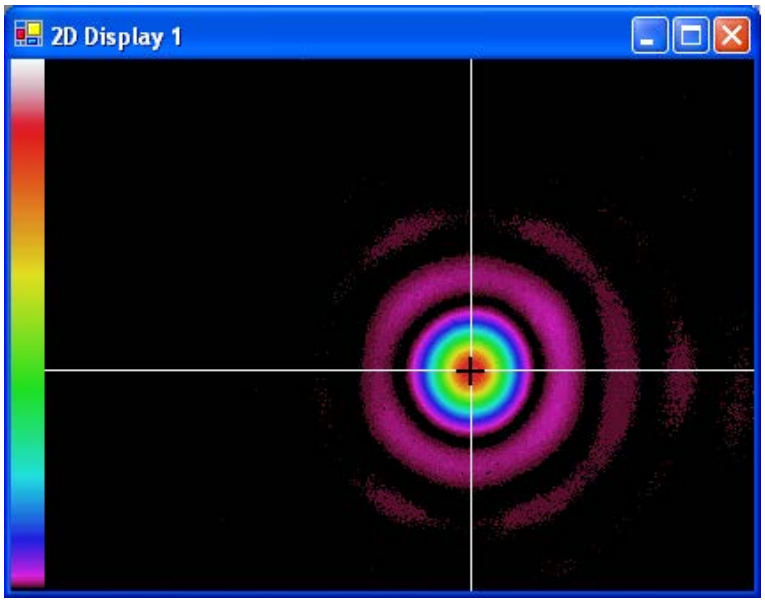

Figure 3.13. *Probe beam profile after spatial filtering, measured by a CCD camera. The picture is done at ~ 10 cm after the pinhole. Diffraction pattern around the beam is blocked by following optics and does not propagate to the atoms position in MOT.*

direction of the magnetic field that was defining the quantisation axis. The probe beam was focused on the trapped atoms with a diameter of $\approx 200\ \mu m$ in order to cover all the atoms confined in the trap with diameter of ~ 140 μm. After the probe beam left the vacuum chamber through the bottom lattice cavity mirror it was monitored with a photo diode. Typical power of the probe light sent to the atoms in our experiments was 2-750 μW depending on the duration of the probe pulse.

Spatial filtering and better control of the polarisation of the probe light increased the efficiency of the probe light π-pulse.

3.4 Lattice trap light laser source at 362.5 nm

From what was said in chapter 2 it is clear that in order to trap neutral mercury and reach desired stability and accuracy the dipole trap should fulfil several requirements. First of all the electric field and therefore the laser light should be quite powerful to form a reasonably deep trap, in our case 5.5 W laser light at 362.5 nm forms the trap with depth of 56 recoil energy. Second the lattice trap light should not perturb the clock transition, which means that the trap should be formed at magic wavelength.

Considering the theoretical calculations of the magic wavelength for mercury atoms we needed a laser source at a wavelength around 360 nm. As in the case of cooling light the best way to produce several hundreds mW at 360 nm was to use an IR laser source along with a SHG stage. The scheme of our lattice light laser source is shown on figure 3.14. We used a homemade Ti:Sa laser that was pumped by 16 W of 532 nm light delivered from the commercial laser system Verdi V-18. Approximately 750 mW of the 725 nm light generated by Ti:Sa was coupled to a bow-tie cavity with a lithium triborate (LBO) non-linear crystal. This cavity was locked to the reflection of 725 nm light from the input coupler using the Hänsch-Couillaud locking technique. The laser system was able to generate up to 150 mW of 362 nm light. This efficiency value is limited by photo damage that the LBO crystal had acquired during years of exploitation.

The 362 nm light generated by the doubling stage was focused in an AOM and 0 order of the AOM was coupled to the lattice cavity through the bottom mirror. Light transmitted through the lattice cavity was sent to a photo diode. Using signal of the photo diode the Ti:Sa laser was locked to a side of the main mode of the cavity. To perform this lock we used a proportional-integral amplifier that generated a correction signal that then was then sent to the PZT glued to one of the Ti:Sa cavity mirrors. However, the lattice cavity had drift due to temperature changes and the frequency of Ti:Sa laser, following this drift, was moving away from the magic value until a mode jump happened.

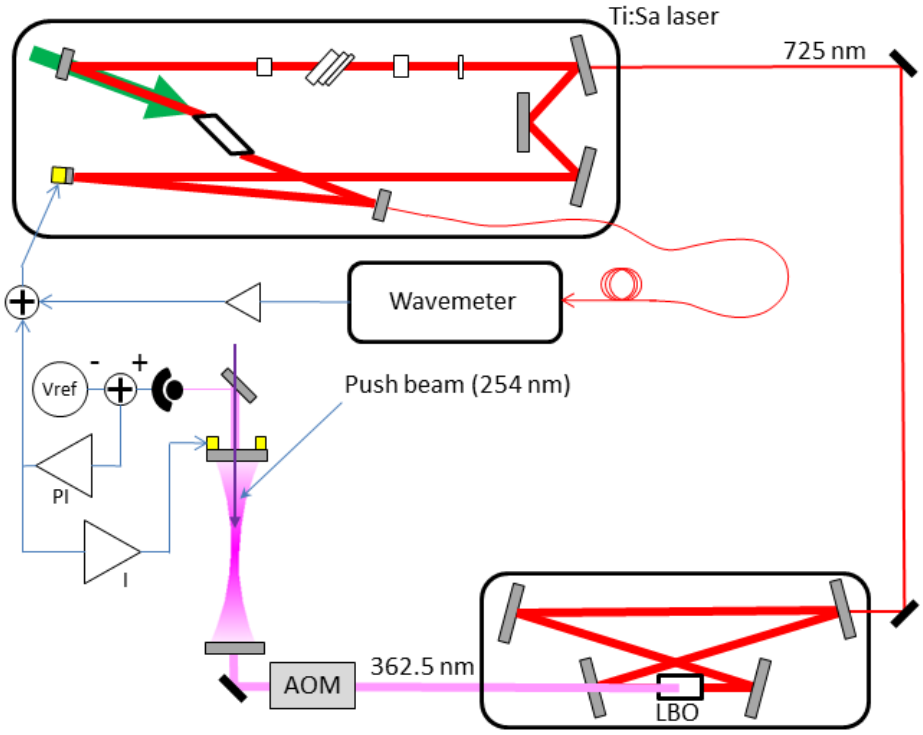

Figure 3.14. *Scheme of the lattice light laser source with the lattice cavity and frequency stabilisation system at the left bottom corner of the figure. The laser source is based on a home made Titanium Sapphire laser and subsequent bow-tie doubling cavity with LBO non-linear crystal.*

Mode jump caused unlocking of all the locks of the system. In order to avoid this an additional lock was implemented that referenced the lattice cavity on the Ti:Sa frequency on a time scale of 1-2 seconds. This helped to increase the time during which the whole system could stay locked, but still this time was less than an hour. The reason for that was the drift of the Ti:Sa laser due to cavity thermal fluctuations. As you can see, a complicated lock system of two nested feedback loops was created, but still we had to relock the system roughly each half an hour. However, it was not a limiting factor at the beginning of my PhD work and we could perform long spectroscopy measurements loosing negligible amount of data while relocking the lattice light laser system.

As you will see in the next two chapters, during this PhD work I have implemented several technical improvements, that allowed to improve the frequency stability of our clock. With the improved frequency

stability it became necessary to control the lattice light frequency in a better way. The cycle to cycle frequency fluctuations of the lattice light were measured to be less that 10 MHz (see sec.5.5.2), which proved to be enough to reach clock frequency stability below 10^{-17} at 1 s, however long term (> 200 s) frequency drift of the lattice light became the clock frequency stability limiting factor. Therefore we implemented a new frequency control system that was based on a commercial high precision wavemeter. This wavemeter was calibrated to uncertainty of 2 MHz and the frequency of the Ti:Sa laser was measured by the wavemeter and locked to the magic value (see more in sec.5.5.2).

Detailed description of this laser system can be found in [61].

Chapter 4

Improvements of the experimental setup

This chapter is devoted to the main important improvements and changes of the experimental setup that were performed during this thesis.

4.1 Cooling laser system improvements

The first improvement that we made on the experimental setup was considering the cooling laser system. In the very beginning of this PhD we had a malfunction of the Versadisk laser. The module that includes diode arrays that pump the disk was flooded with water. This failure was traced back to the cooling system of the pump module, which is based on circulation through a micro-channels system in the baseplate of the module. It was found that these micro-channels tend to break under erosion and flood the whole module with water roughly each one year and a half. We decided to switch to a different pump module to avoid repetition of this situation. The new pump module is manufactured by DILAS company. It is also water cooled but doesn't have micro-channels system and therefore should be more reliable.

The DILAS pump module was specified to have the same voltage and current requirements and was compatible with the old pump power supply. Unfortunately the size of the new pump module is too big for it to be installed on the place of the old pump inside the power supply (fig. 4.1). We had modified electric connections and cooling

circuit to install the new pump module outside the power supply.

(a)

(b)

Figure 4.1. *(a) Old pump module with micro-channels system (white part at the bottom). (b) New pump module*

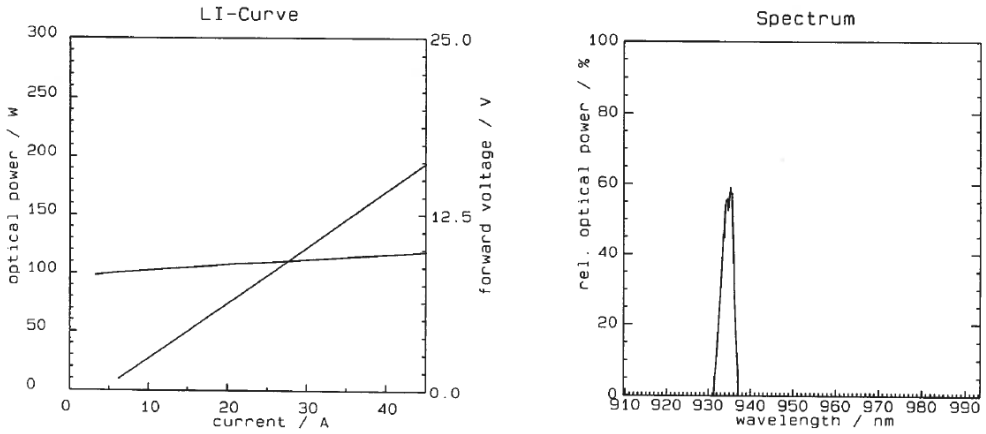

(a) Old pump specifications

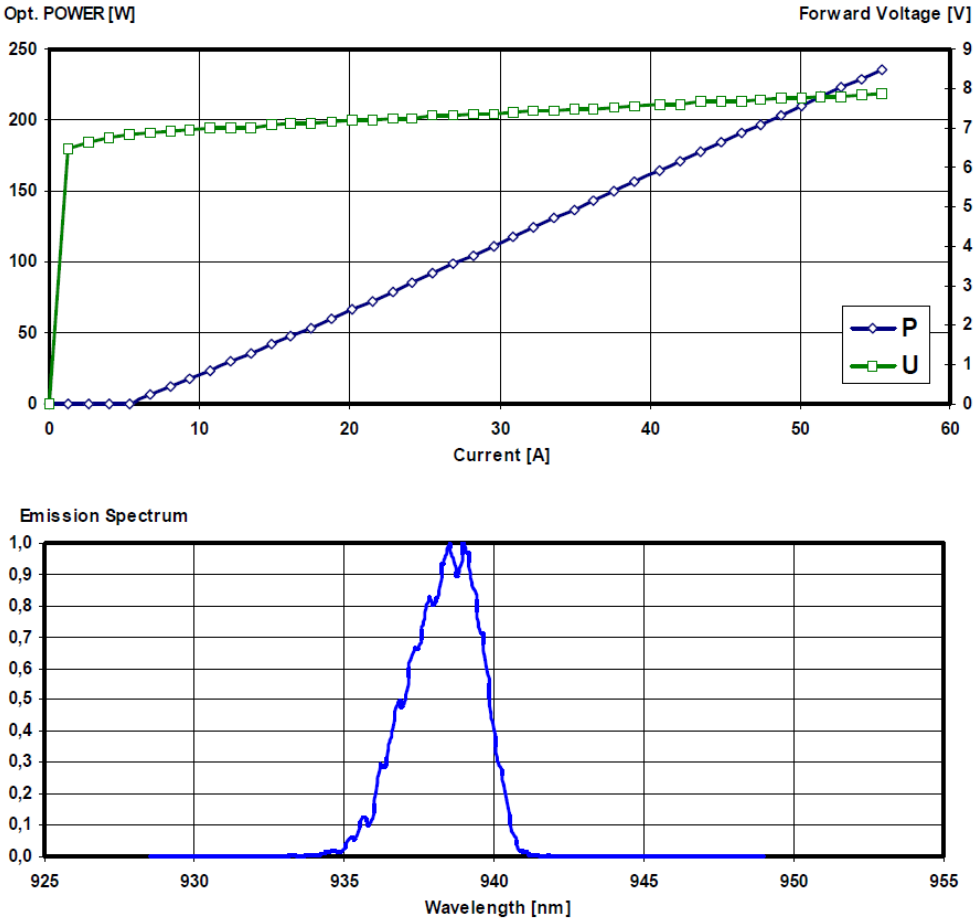

(b) New pump specifications

Figure 4.2. *Radiation wavelength, current, voltage and output power specifications for the old and the new diode pumps.*

The output power and spectrum of the new pump module are similar to the ones of the old pump (fig. 4.2). We've performed a test of the new pump output power up to 50 W, the limit of our power meter, and it was in good agreement with the data from the spec list supplied by the company. The threshold current for the new pump is 4.2 A. After the test the pump light was re-coupled to the Versadisk cavity and the latter was realigned. We have obtained generation of 1014.9 nm light with the new pump module and as one can see from the figure 4.3 even more efficient than with the old pump. We attribute this to better Versadisk cavity alignment. The threshold current for 1014 nm light generation with new pump is $11.6\ A$. It took us in total around six month to find, to supply, to test and implement the new pump module.

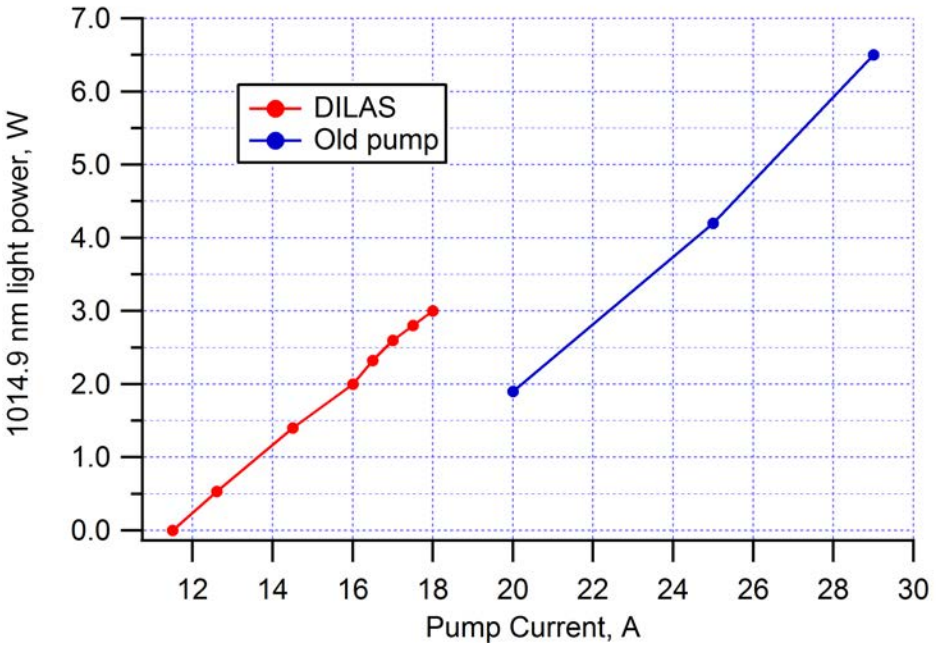

Figure 4.3. *Measured output power of Versadisk laser at 1014.9 nm versus the pump diodes current. The laser has higher output power at the same current with the new pump module (red dots) than with the old (blue dots) due to a better alignment of the Versadisk cavity.*

After the new pump module was implemented we also measured relative intensity noise of the power supply current (fig.4.4) and of 1014.9 nm light (fig.4.5) in order to check if change of the pump module introduced additional noise. As one can see from the figures no

significant noise was found.

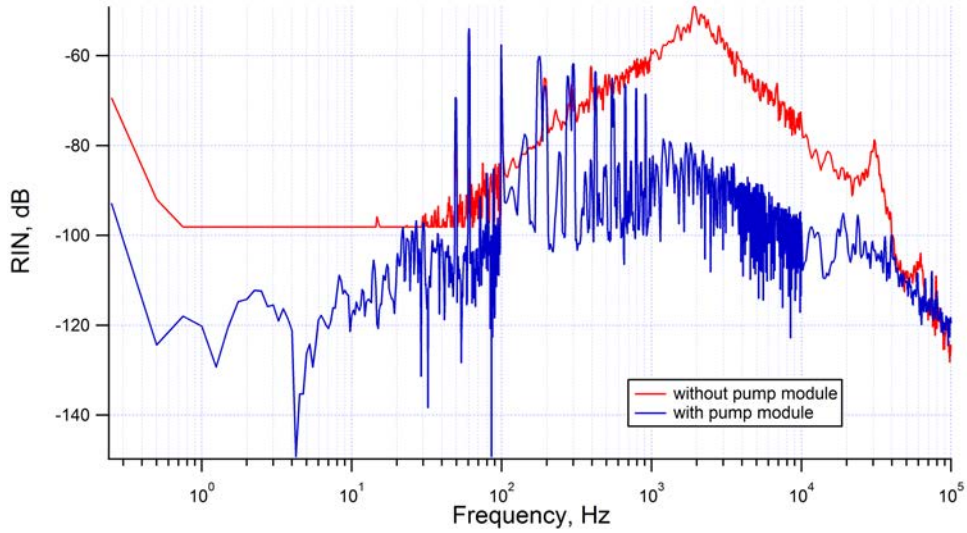

Figure 4.4. *RIN of the power supply current in short circuit (red) and with pump module connected (blue)*

When implementation and all tests of the new pump module were done IR light of Versadisk was recoupled to the first doubling stage and the cavity of the stage was realigned. We had 1.6 W at 507 nm with 4.3 W of input light at 1014.9 nm. Since we couldn't use all the available UV power that can be generated with our laser system due to the degradation of the BBO crystal in the second doubling stage (see sec.4.1.2), we decided to operate our system at around 20 A of the pump current, which corresponds to $\approx$1 W of light at 507 nm.

We have also improved the frequency control of the Versadisk laser system. As it was said in section 3.1.1 the frequency tuning of the Versadisk was implemented via the temperature control of the intracavity etalon. This way of frequency tuning works reasonably well except the cases of what we call "self locking" of the cavity. We think that the self locking effect occurs due to the high light power that is being stored in the cavity. With a pump power of 100 W we estimate a circulating power in the laser cavity to be well above 1 kW. This power heats the optics and probably the disk itself causing thermal expansion and modification of the cavity behaviour. In certain cases changing the laser frequency by acting on the etalon induces a change of the stored light power, which in turn changes the cavity behaviour in such a way, that frequency of the light comes back to the initial value. In

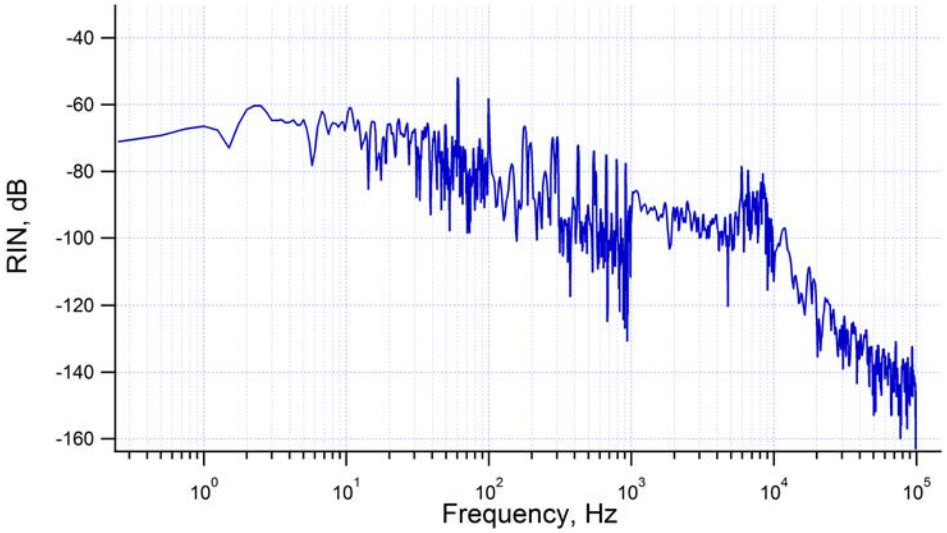

Figure 4.5. *RIN of the signal of the photodiode with 1014.9 nm light.*

other words cavity locks itself on a certain frequency and when such behaviour occurs it usually dominates within a given mode. If this happens cavity needs to be manually tweaked and another operating point has be found. In order to decouple frequency change from the temperature of the etalon we decided to change the angle of the etalon instead of the temperature. The etalon was installed on a mirror mount with possibility to control vertical and horizontal axes of the mount remotely with the help of motorized actuators with a step of ~ 1 nm (see fig.3.2). This approach didn't show "self locking" behaviour and solved the problem of frequency tuning. It has to be mentioned though, that while a small frequency tuning within a given mode is done with picomotors, big frequency changes were still done with the temperature. Tilting the etalon to far from position perpendicular to the light beam reduces the IR output power.

4.1.1 New cooling laser system

Few month before the end of my thesis a new solution for cooling laser system was found and implemented. The Versadisk and the first doubling stage were replaced by the new system and the system was then coupled to the second doubling stage, described in the section 4.1.2. It is worth mentioning that the doubling stage described in section 4.1.2 was implemented significantly before and was already

used with Versadisk laser system.

The new system is shown on figure 4.6. It is based on a home made external cavity diode laser (later seed laser) that generates light at 1015 nm. This light is sent to a commercial fiber amplifier and then is frequency doubled to 507 nm in ppLN crystal. With typical ~ 12 mW generated by the seed laser, the system is able to deliver stable 1.5 W at 507 nm. After the seed laser was temperature stabilized it has shown continuous operation within a single mode during four months. The new cooling laser system is able to deliver stable output power at the right frequency and requires minimum effort to operate. Since the seed laser is never turned off and the fiber amplifier is essentially an industry-qualified device, the new system does not have warming up time as opposed to the Versadisk. Even though the problem of degradation of the efficiency of the second doubling stage is still present, the new system was of no doubt very significant and important improvement that simplified and sped up our experiment.

Figure 4.6. *Look of the new cooling laser system. On the figure the seed laser is inside the small white box on the right, the doubling head of the amplifier is in the left bottom corner and the new 254 nm doubling stage (see sec.4.1.2) is in the aluminium box*

4.1.2 New doubling stage at 254 nm

Another step was to improve the second doubling stage of the cooling light system. It is known that BBO crystal as well as optics coat-

ings are prone to damage when exposed to high power UV light and our experimental setup is not an exception. This kind of damage accumulates over the time and reduces the amount of UV light available at the output of the frequency doubling stage. This process continues until the spot on the crystal becomes unoperational. Depending on the power, duration, and the rate at which the crystal is being used, the lifetime of a spot slowly decreases from several days in the beginning when a new crystal is installed, to several minutes at the end. Shifting from the damaged place to a new "clean" spot of the crystal recovers the amount of generated UV light. Degradation of the second doubling stage performance is the main limitation of the experiment as it is today.

The nature of the damaging process is unknown, however during years of work with the BBO crystal we learned several things about this effect. Very significant role plays the cleanness of the environment in which the crystal operates. We found that contamination is the major reason of degradation of the SHG efficiency and the crystal is very sensitive to even small amount of it that is left in the air after filtering with HEPA filters. Degradation caused by contamination is slowly accumulated over the time. Another source of damage of the crystal is an abrupt switch off of the light propagating through it. This case is different, the damage is acquired instantly and causes complete loss of the SHG efficiency. We think that nature of this effect comes from changes in structure of the crystal caused by abrupt temperature change.

It was empirically found that presence of pure oxygen helps to recover the crystal and slows down damaging of optics coatings. Therefore we decided to make new 253.7 nm frequency doubling stage from scratch, that will be enclosed in an airtight box filled with pure oxygen. Design of the cavity enclosure is shown on figure (4.7). The box of outer sizes 620x220x135 mm was machined from a single piece of aluminium in the machine shop of Observatoire. The box has 15 mm thick walls and 20 mm thick basement. Giving the complexity of machining bulky single piece and foreseeing possible changes in incoming and outgoing connections of the box we decided to go for big multi-purpose openings in the box, that will be closed with plates, which can be easily exchanged and machined as needed. All machined parts including the box itself were cleaned in ultrasonic bath in order

to remove machine grease, oil and other possible sources of contamination.

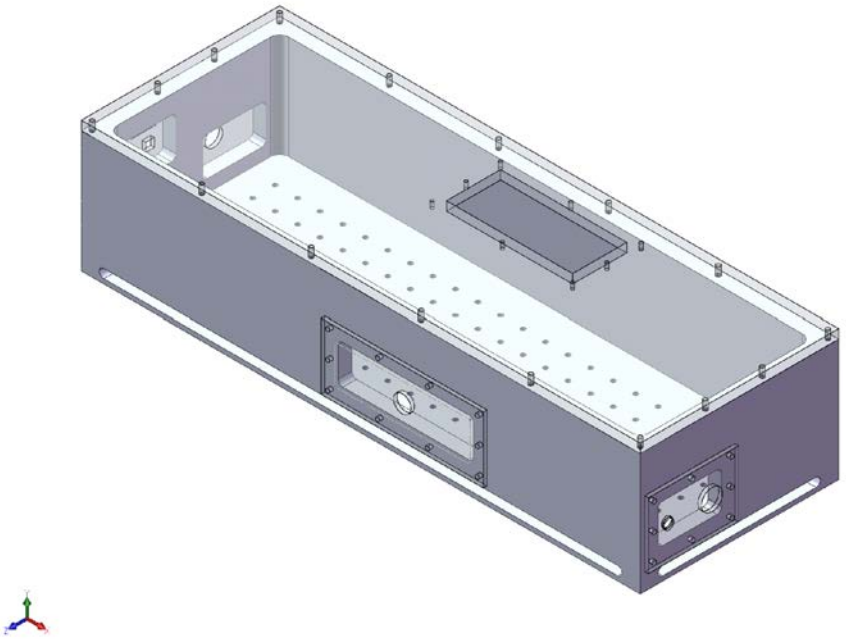

Figure 4.7. *Aluminium enclosure for 254 nm doubling stage. The enclosure is a monolithic* $620 \times 220 \times 135$ *aluminium box with openings for light beams and electric connections.*

Input light enters the box through a one inch diameter window with AR coating at 507 nm, which is glued to the input plate. The frequency doubling cavity is formed by 2 plane and 2 curved mirrors (see fig.4.8). The input coupler (M4) is a plane mirror with HR coating on one side that reflects 98.5% of light at 507.5 nm at 9° and AR coating on the back side, that reflects less than 0.2% of light at the same wavelength. The second plane mirror (M1) reflects more than 99.95% of the light and is glued on a PZT actuator. The two curved mirrors have radius of curvature 100 mm and form the short arm of the cavity with $22\ \mu$m waist at the center of the BBO crystal. Both curved mirrors reflect more than 99.9% at 507.5 nm and one of them (M3), which is the output coupler, transmits ∼95% of light at 254 nm.

We have measured the amount of 507 nm light that leaks from mirror M2 (see fig.4.8) and determined its transmission to be $\approx 0.007\%$. Scanning the cavity with PZT and monitoring the leak we have mea-

sured the peak power of 507 nm light stored in the cavity to be ≈ 92 W with input power of 950 mW. The cavity finesse estimation based on the linewidth of main mode peak yields ~ 220. Free spectral range of the cavity is 240 MHz.

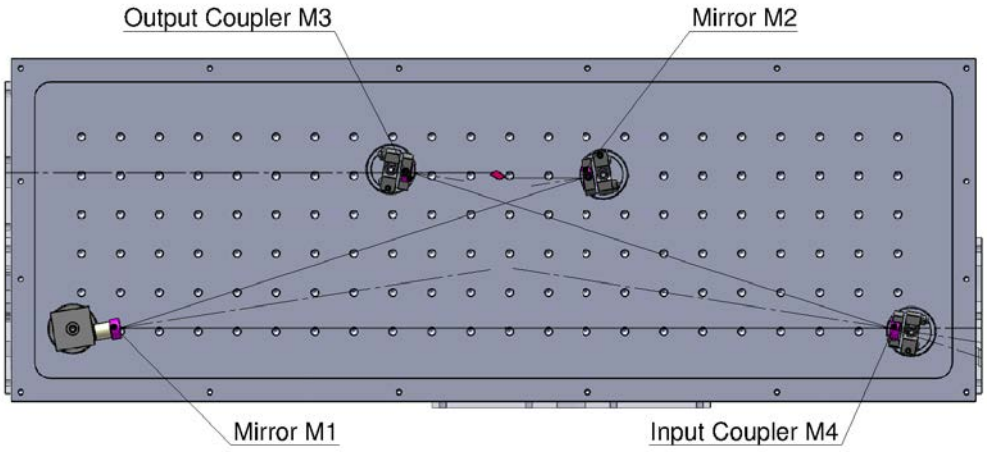

Figure 4.8. *Position of the 254 nm doubling cavity optics (with mounts) inside the new enclosure. The BBO crystal is between mirrors M2 and M3.*

The BBO crystal is fixed on a copper support with the help of 2 mm thick plate made of a special alloy of copper and zinc, as it is shown on figure (4.9). The copper support is clamped with a titanium part in such a way that it can be rotated around its axis for rough alignment of the incidence angle between the 507 nm light and the crystal input facet. The titanium part in turn is attached to a mount with possibility to shift in all three directions and to change ϕ and θ angles of the crystal input plane. The copper support has a smaller diameter section intended for a heating wire to keep the crystal above room temperature. In order to reduce the degradation of the crystal from UV light pure oxygen is delivered right to the surfaces of the crystal via small tube connected to the guiding channels made in the support (see fig. 4.10). Crystal is also covered by an aluminium cap for better protection from contamination.

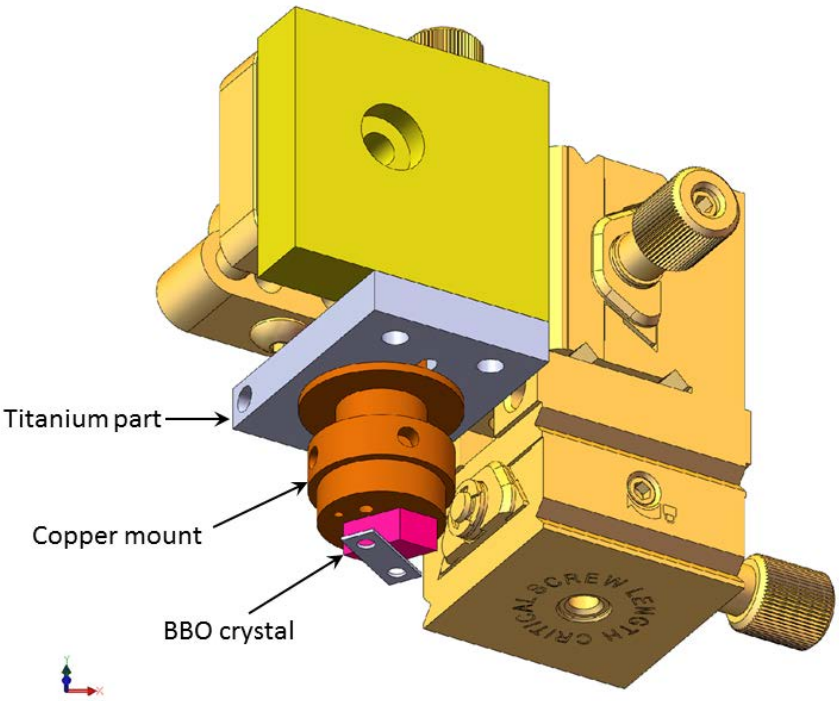

Figure 4.9. *BBO Crystal mounting. Crystal is attached to a copper mount. The copper mount is attached to a 3 axes translation stage with the help of a specially made titanium part.*

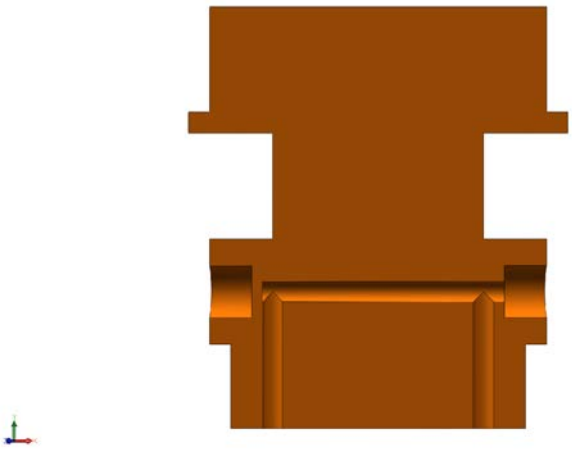

Figure 4.10. *The copper mount in cut. On the figure one can see two channels used to deliver oxygen to the crystal.*

After the BBO crystal was installed and the cavity was aligned, the box was completely sealed using rubber pads in between plates and the box. Pure oxygen was discharged in the box under pressure and air was purged through a small opening in one of the plates. The small opening was closed after and the box stayed over pressured with a small amount of oxygen continuously flowing through it. Being at pure oxygen frequency doubling cavity was locked for the first time and a test of degradation was performed. Cavity was locked for more than half an hour at different powers generating up to 110 mW of light at 254 nm and no sign of crystal or optics damage was found. Once closed the frequency doubling stage was able to generate up to 300 mW of 254 nm light with ≈ 1 W of input, however we were operating it at rather low powers in order to save crystal for future spectroscopy experiments. We operated the doubling stage at ≈ 40 mW of 254 nm light for three months without any sign of degradation.

Unfortunately after an electrical power failure in the lab, the spot on the BBO crystal was damaged. Our interpretation is that due to rapid temperature decrease of the crystal (from 33°C to room temperature, the surface of the crystal was contaminated and the contamination was subsequently burnt by the input light. We countered this by shifting the crystal but the new spot did not last as long as the first one. Over the time spots on crystal were acquiring damage and we had to shift the crystal, opening the air tight box again and again. We found that cleaning the optics helps to increase the efficiency and lengthen the life of the crystal, which we consider a further indication that contamination is the probable cause of degradation. We suppose that contamination is coming from outgassing of the rubber paddings.

In attempt to increase the lifetime of the crystal the paddings were removed and the geometry of the cavity was changed to a shorter one, in order to enlarge the waist inside the crystal and therefore decrease the intensity of the light. On the figure (4.11) one can see the change of the cavity geometry. Short version of the cavity had total length of 84.2 cm and waist in the crystal 30 μm. The estimated peak UV light power of the short cavity was 150 mW with ≈ 1 W of 507 nm light.

We also pressurized the doubling stage with pure nitrogen to see if it will help to prevent the damage of crystal, but we found that in nitrogen atmosphere the lifetime of the crystal was shorter. Thus we got another evidence that degradation of the efficiency comes not only

from contamination, but also connected with absence of oxygen in the environment.

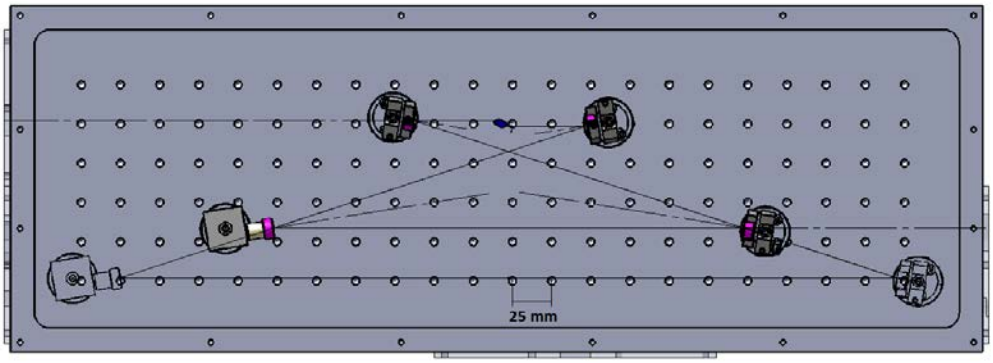

Figure 4.11. *254 nm doubling cavity in "short" configuration. Contour of mirrors and mounts for the "long" configuration is shown for better understanding of the cavity changes.*

4.2 New lattice trap

At the beginning of this thesis the main limitation of the experiment was the very shallow lattice trap, limited to 20 E_R. With such trap depth the limitation was not only in signal of trapped atoms, but also in strength of the confinement and in capability to have big enough leverage factor to control lattice light shift and measure the magic wavelength with better precision. In other words we did not had enough lattice light power to create a measurable lattice light frequency shift of the clock transition at wavelengths close to the magic value. Therefore, the most important technical improvement of the experimental setup that I have done during my thesis and that pushed the limits of the experiments much further was the development of a new lattice cavity. This section describes in details all preparation steps and implementation of this new lattice cavity.

In the limit where the trap depth is on the same order of magnitude as the atomic temperature or less, increase of the trap depth leads to increase of trapped atoms number. As it was already said the depth of a lattice trap depends on the intensity (see eq.1.4). Increasing

intensity of the light by increasing its power in our case is rather troublesome. First of all because we are limited in lattice light power and it is impossible to increase it sufficiently enough with existing laser system. Second, coating of the lattice cavity mirrors gets damaged when exposed to higher power UV light. Therefore we have decided to use another approach and to shrink the waist of the trap instead.

Since the polarisability of mercury at the magic wavelength is relatively weak the lattice light has to be quite powerful to create a trap of decent depth. For instance, to create a 1D lattice trap with waist of 100 μm and depth of 100 E_R for Hg one needs 20 W at 362 nm, while for Sr only 1.1 W at 813 nm. It was decided to decrease the waist of our trap twice in order to increase the intensity by a factor of 4 and in the same time to have still sufficiently big overlap area of the lattice with the MOT. This was done using new lattice cavity mirrors with a smaller radius of curvature equal to $r = 150$ mm (previous mirrors had radius of curvature $r = 250$ mm). The coatings of the new mirrors are specified to have high reflection at the magic wavelength $R(362) = 99 \pm 0.5\%$ and low reflection at the wavelengths of the cooling and probe light - $R(254) < 10\%$ and $R(266) < 5\%$ respectively. The backside of the mirrors is AR coated for all the three wavelengths.

The waist of the new lattice trap calculated based on the new mirrors radii and spacing is 69μm. For this waist depth of 100 E_R can be reached with ~ 10 W circulating in the cavity. Before I will describe the new lattice trap, process of its implementation and its characterisation (including measurement of the trap frequency) in details I will briefly introduce the theory of the parabolic approximation for a 1D lattice trap. This approximation is very useful for experimental characterisation of the lattice trap.

4.2.1 Lattice trap parabolic approximation

The optical potential of 1D lattice trap varies along the axial direction (the direction of propagation of the light) as

$$U(z) = U_0 \cos^2(k_l\, z) = \frac{U_0}{2}\left(1 - \cos(2k_l\, z)\right). \tag{4.1}$$

Since atoms are attracted to the maxima of local intensity and the trap is formed by a standing wave the depth U_0 is defined by $I_{max} = 4I_p$,

where I_p is the peak intensity, which equals $I_p = 2P/\pi w_0^2$ for the Gaussian beam of power P and waist w_0.

Potential near the bottom of the wells can be approximated by parabola and trapped atoms motion can be described as a motion of a harmonic oscillator. Assuming that atoms explore only small area next to the bottom of the trap we can write

$$U(z) \simeq \frac{U_0}{2}\left(1 - \left(1 - \frac{(2k_l\, z)^2}{2}\right)\right) = \frac{U_0}{2}(2k_l^2\, z^2), \tag{4.2}$$

which is equal to the harmonic potential $U_h(z) = \frac{1}{2}kz^2$ with $k = 2U_0k_l^2$. Therefore in axial direction trapped atoms will oscillate with frequency

$$\omega_{axial} = \sqrt{\frac{k}{m_{at}}} = \frac{2\pi}{\lambda_l}\sqrt{\frac{2|U_0|}{m_{at}}} \tag{4.3}$$

We can do the same approximation for the transverse motion of atoms. The potential in transverse direction has dependency

$$U(x) = U_0 \exp\left(-2\frac{x^2}{w(x)^2}\right). \tag{4.4}$$

Assuming that atoms explore only bottom of the trap and $x \ll 1$ we can write

$$U(x) \simeq -\frac{2U_0}{w^2}x^2 = \frac{1}{2}k_t x^2 \tag{4.5}$$

where $k_t = -4U_0/w^2$. Frequency of trapped atoms oscillations in transverse direction then equals

$$\omega_{trans} = \sqrt{\frac{k_t}{m_{at}}} = \frac{2}{w}\sqrt{\frac{U_0}{m_{at}}}. \tag{4.6}$$

Therefore measurement of the trap frequencies with the harmonic potential approximation can give an estimation on the trap depth. It is worth to mention that the approximation described above is the simplest model and can give only rough estimation. There are more sophisticated models [62] that are taking into account quadratic distortion of the axial potential, transverse motion of atoms in the trap, coupling between longitudinal and transverse degrees of freedom etc. These sophisticated models provide better approximation results, but they are not required for interpreting the results of this manuscript.

4.2.2 Test of the new lattice trap mirrors

Implementation of the new lattice trap mirrors on the experimental setup is a complicated and time consuming operation. On the figure 4.12 you can see a vertical cut of our 3D-MOT chamber with top lattice cavity mirror mounted on it. The cavity mirror is indium sealed on a titanium part (see more in sec.4.2.3) and the titanium part is connected to the chamber with flexible vacuum connection. The construction is also mounted on three PZT drivers, that allow changing the lattice cavity length. As you can see, change of the lattice cavity requires breaking vacuum of the experiment. Therefore to be sure that new mirrors had good coatings and to avoid the need to open the vacuum chamber for the second time, we have performed several tests of the new mirrors before installing them on the experimental setup.

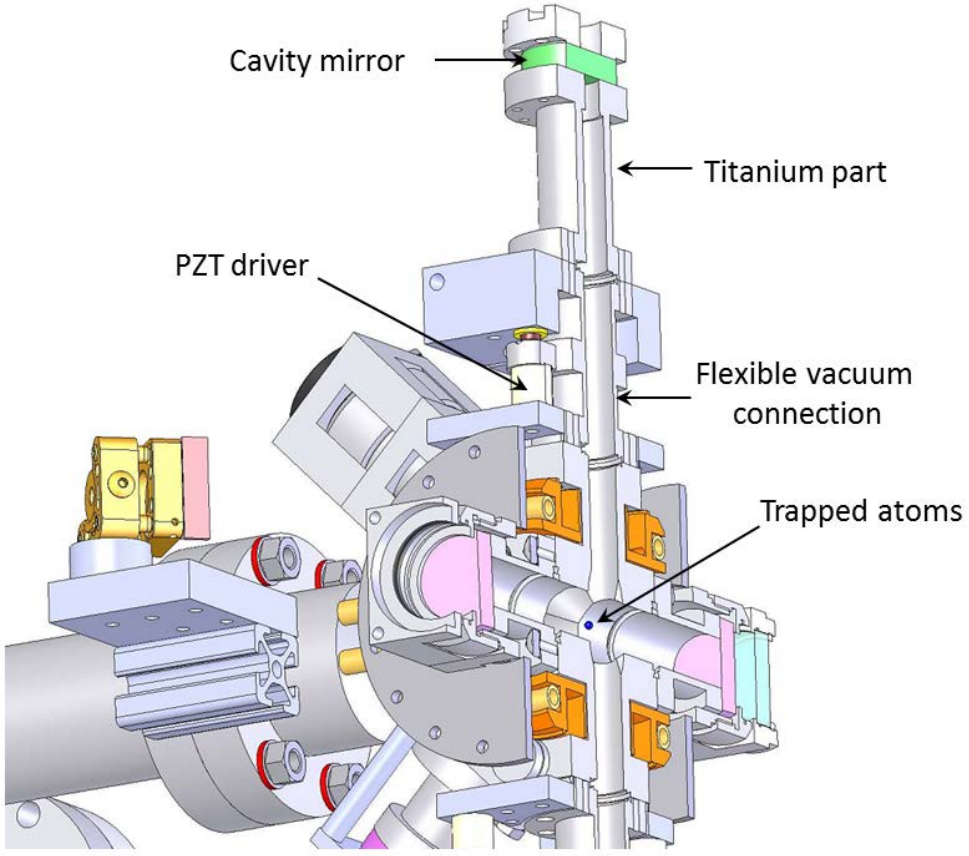

Figure 4.12. *Connection of the lattice cavity mirror (on the top) to the main vacuum chamber. MOT atoms are shown as blue cloud in the middle of the chamber.*

First of all we have measured the transmission of the new mirrors at the magic wavelength. We installed the mirrors in the lattice light beam with power 10 mW and registered the transmitted power with UV photo diode. Measured transmission was in a good agreement with the value specified by supplier. The measured power transmitted by the windows was $63,5$ μW. Taking into account that input power is known with ≈ 1 mW uncertainty the measured transmission of the mirrors at magic wavelength is $T(362) = 0.63 \pm 0.06\%$. This value later serves for determining the circulating power in the cavity and the lattice depth.

Taking into account problems with previous lattice cavity mirrors, which had acquired damage when being exposed to UV light under vacuum, plenty of other things to improve on the experiment in the meanwhile and intention to minimize the time during which the vacuum chamber will be opened we decided that it was necessary to take time and carefully test coatings of the new mirrors before implementation. Therefore we performed a damage test of the mirror coatings under high UV power in two steps. First we made a Fabry-Pérot cavity identical to the one of the lattice trap from the two new mirrors in the air. The lattice light beam was mode matched to this test cavity and after the cavity was locked on the main mode. We did not found any degradation of the mirror coatings after the cavity was locked for 20 minutes with approximate travelling power of 4 W.

The second step was to perform the same degradation test, but in vacuum, since it was seen before that coatings that can withstand a certain amount of power in air are damaged by the very same power under vacuum. For this we mounted mirrors on vacuum contact on special parts (see section 4.2.3). Mirrors on the titanium parts were mounted on a small vacuum part, forming a vacuum cavity of the right length (see fig.4.13). Test vacuum cavity was pumped to $\sim 4 \times 10^{-8}$ mbar with the help of turbo pump, which was later disconnected and a small ion pump was turned on to keep vacuum at the level. After this we coupled the lattice light to this test cavity and performed the same degradation test. We did not found any coatings degradation in vacuum as well and it was decided to install new mirrors on the experimental setup.

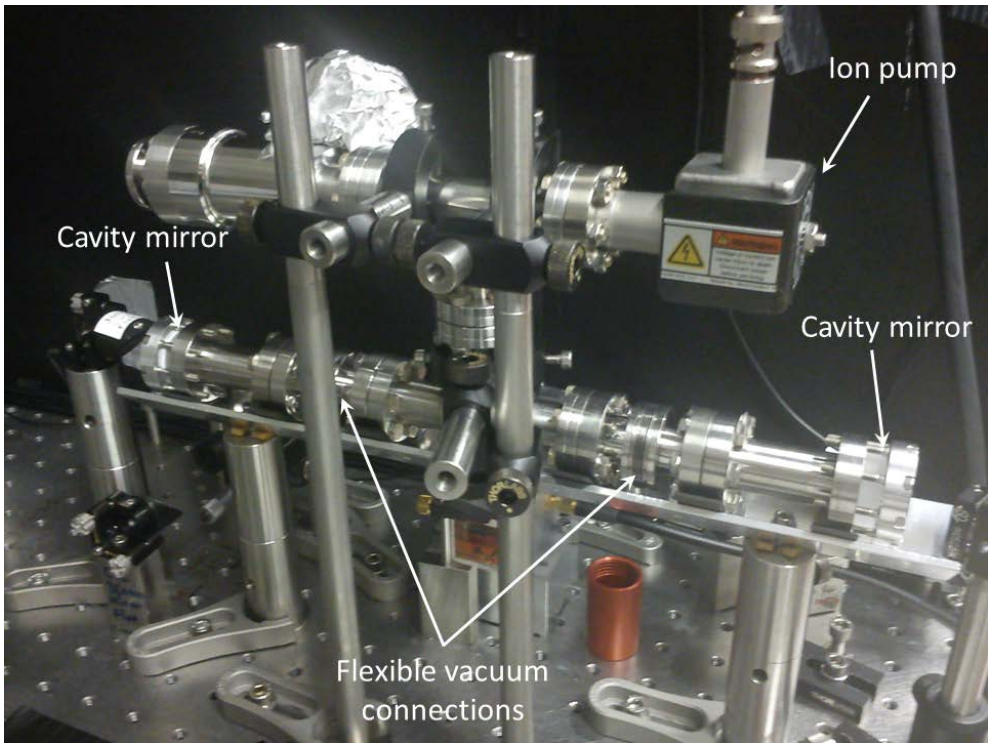

Figure 4.13. *New lattice mirrors mounted on test vacuum cavity in order to check degradation of mirrors' coatings exposed to high power UV light in vacuum.*

4.2.3 Implementation of the new lattice trap

From the set of eight mirrors that we had tested we used the two with the lowest transmission $T(362) = 0.63 \pm 0.06\%$ for our new lattice cavity. As it was said in the previous section, before new mirrors were implemented in the experimental setup, they were installed on a special vacuum part. This vacuum part is made from titanium and has a standard CF-16 flange on one side. The other side is flat and has 8 threaded holes (see fig.4.14). It was decided to mount mirrors on the titanium parts using indium vacuum contact. In order to avoid any leaks in the place of contact the flat sides of both parts were manually polished and inspected until no visible scratches was left on it. The titanium parts were cleaned in an ultrasonic bath several times, to get rid of machine oil, polishing powder and other contaminations. The parts were also baked at 330° C under vacuum to outgas. After all the preparations an o-ring shaped wire of indium was placed between the flat surface of the part and the mirror. The mirror was pressed to the part, while monitoring the retro-reflection of a tracing HeNe laser

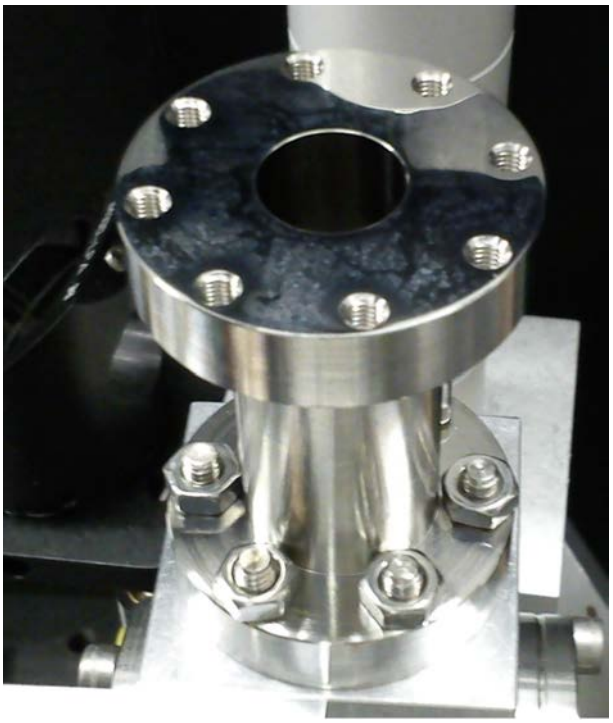

Figure 4.14. *Titanium part for the new lattice mirrors mounting. The top flat surface of the part is polished and used for indium sealing of the mirror. The bottom part has CF-16 flange and on this is connected to the setup that was used to align the mirrors during the indium sealing procedure.*

beam to ensure the mirror was not tilted (see fig.4.15).

Before installing the new lattice cavity we had to take care and not loose the alignment of the lattice trap with the MOT trapped atoms. The problem is that in our experimental setup it is very hard to overlap optical lattice with the MOT atoms due to the fact that detection is done in a direction perpendicular to the lattice trap. It means that we could not see the MOT trapped atoms and the lattice trap on the same image. Therefore, before removing the old trap we coupled to it a reference lattice light beam. The reference beam was coupled from the top, since it was more comfortable and less risk to lose alignment by accidentally bumping some mirrors during the change of the lattice cavity mirrors.

After all the references were set we broke the vacuum and removed the old lattice trap mirrors. To avoid water and contamination getting in the chamber we constantly blew nitrogen through the chamber during all the time it was open. The titanium parts with the new mir-

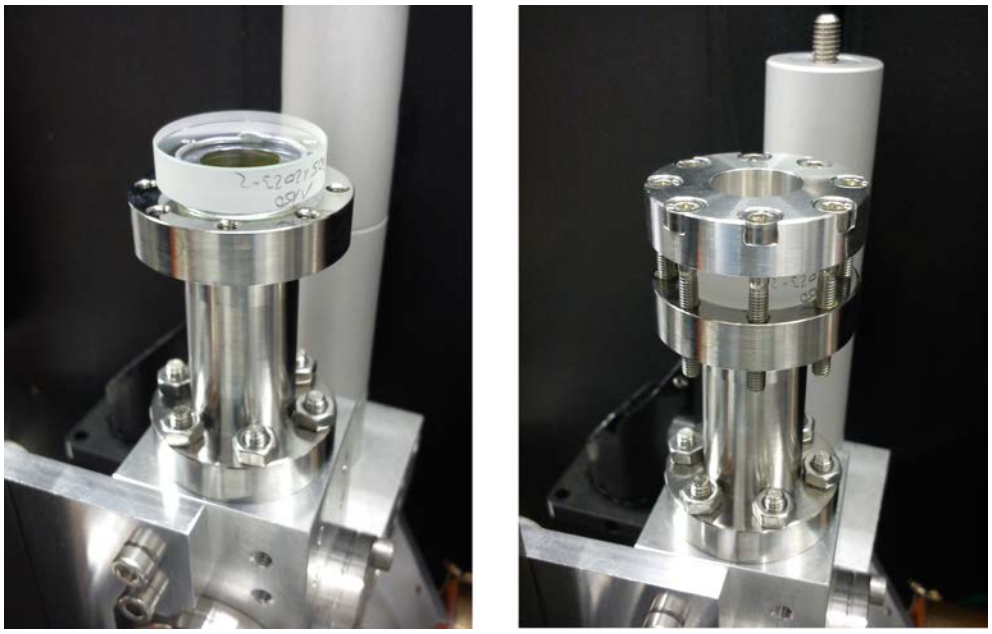

Figure 4.15. *New lattice mirror placed on the titanium part with indium wire in between on the left, and completely mounted new lattice mirror on the right*

rors were connected to the chamber with flexible vacuum connection. Those connections are necessary to be able to align the cavity and also to change its length with the help of PZT drivers. The bottom mirror was installed first and aligned on the reference beam. When both mirrors were installed and the vacuum chamber was closed we pumped the chamber with a turbo pump down to 10^{-7} mbar. We performed a leak test with helium and didn't found any sign of leaks. While still being connected to the turbo pump two getter pumps were activated. After this the final mass spectrometer analysis was done (see fig. 4.16). Before stopping the turbo pump we had closed the valve of the vacuum chamber, to which the flexible tube of the turbo pump was connected. This means that vacuum chamber was disconnected from the pump and we continued pumping only the tube. We saw no changes in mass spectrometer analysis before and after the valve was closed, which indicates that most of the residual particles seen on the figure (4.16) were coming from the tube and not from the experiment. When the ion pump was turned back on its current settled at the value close to nominal, which indicated that vacuum level of few 10^{-9} mbar was reached. The new lattice cavity was closed on a reference beam with the top mirror and the lattice light was coupled to the new cavity.

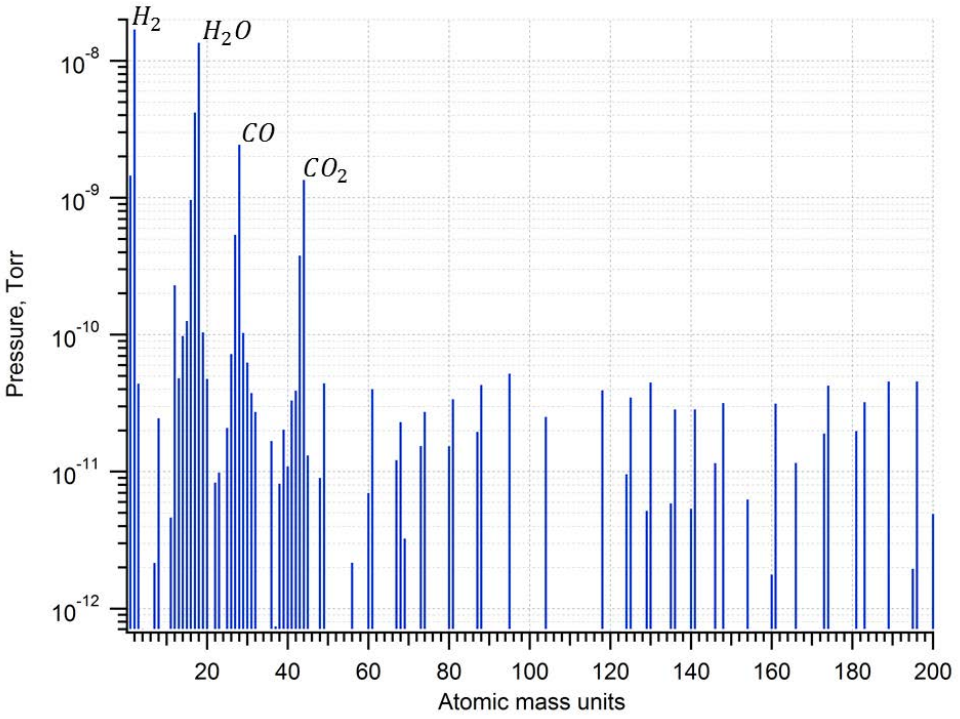

Figure 4.16. *Mass spectrometer analysis done before disconnecting the turbo pump from the vacuum chamber. Most of the residual particles are coming from the flexible tube connection of the pump with the chamber.*

Unfortunately, in spite of our attempt to preserve the alignment of the lattice trap we could not find the lattice trapped atoms signal right away. We had to overlap MOT with the lattice trap, which was a very hard and time consuming task. In practice, we had to overlap in vacuum 110 μm waist MOT with 69 μm waist lattice trap without possibility to image both of of them on the same picture and without any information about their relative position. Beside this we expected fraction of MOT atoms loaded in the trap to be around 1% which would give quite small signal that could be buried into the CCD background noise if MOT and lattice trap were only partly overlapped.

Our first step, considering that alignment was not lost completely and the new lattice trap had to be close to the atoms position, was to shift the MOT position in horizontal plane with magnetic field exploring all available range. Due to difficulties and complexity of operation of our cooling laser system it took us several months to explore reasonable area of MOT positions, but we didn't succeed to find the overlap.

The second step was to align the push beam (see sec.5.3) on the MOT, by minimizing the number of trapped atoms in presence of the push beam. From the difference of the paths of lattice and push beams we could estimate the relative position of the MOT and lattice trap. However, we found that the two beams were quite well aligned, and more precise alignment was not possible due to the relatively big size of the lattice beam at the output of the vacuum chamber and non-Gaussian shape of the push beam with non-uniform spatial intensity distribution. Finally we decided to shift the lattice trap position and for doing this we developed an additional detection path that would allow us to detect MOT and lattice trap on the same image. The new detection path was done in such a way that the main detection scheme was left untouched and normal operation of the experimental setup was not disturbed (see fig.4.17). We could easily switch between the two configurations. Knowledge of the relative position of the lattice trap and the MOT allowed us to adjust the lattice cavity in a right way and finally overlap the lattice trap to the MOT.

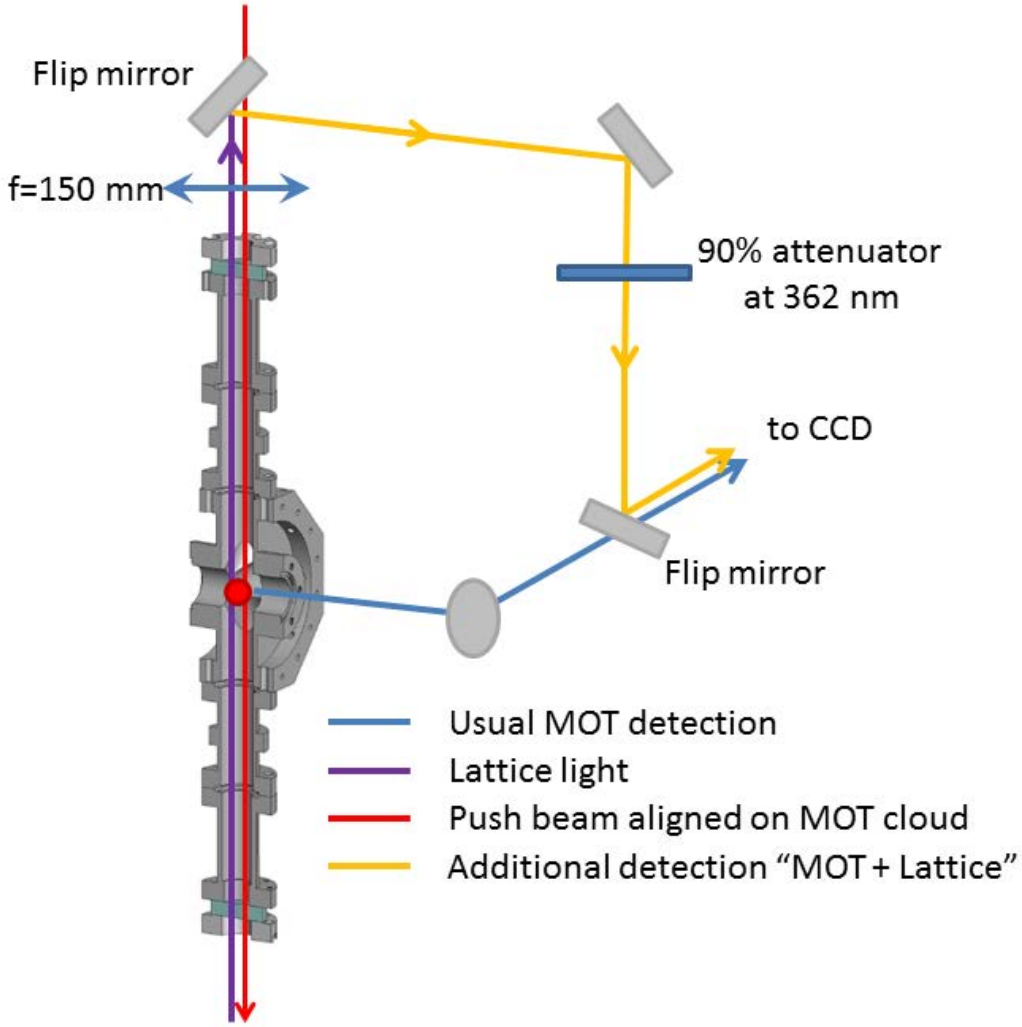

Figure 4.17. *Scheme of the additional detection path (yellow line). The additional detection path allowed to image the MOT trapped atoms and the lattice trap on the same figure and overlap the two.*

4.2.4 Characterisation of the new lattice trap

With the new lattice trap and the trapped atom's signal in place we could start characterization of the new trap. First of all we have measured the width of the lattice cavity's resonance peak (see fig.4.18). The FWHM of the resonance is $\Delta\nu \sim (1.7 \pm 0.19)$ MHz. The FSR of the lattice cavity is 543 MHz and therefore the finesse of the cavity is $F = 300 \pm 40$ (this is the mean value and standard deviation of a set of measurements), which is in good agreement with calculations based on the mirrors coating specifications and measurement. Finesse of a cavity consisting of two mirrors with amplitude reflectivity coefficients r can be calculated as (see e.g.[63], [13])

$$F = \frac{\pi r}{1 - r^2} \tag{4.7}$$

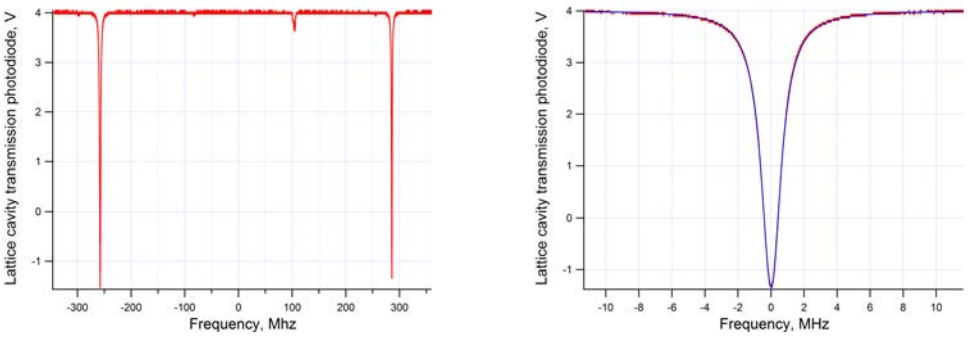

Figure 4.18. *On this figure you can see coupling of the lattice light to the new lattice cavity. Figure (a) shows transmission of the lattice cavity and figure (b) shows Lorentzian fit of the main mode of the lattice cavity. The FWHM of the peak is* 1.7 ± 0.19 *MHz.*

Using one of the spare cavity mirrors as an attenuator, we have calibrated a UV photo diode on a thermal power meter and then used it to measure the power travelling inside the new lattice cavity. We installed calibrated photo diode at the exit of the lattice cavity and measured the output power of the lattice light. With the input light power of $P_{IN} = 88 \pm 1$ mW, from which $\sim 0.6\%$ (~ 530 μW) is coupled to the cavity, the measured power at the exit of the cavity is $P_{OUT} = (43 \pm 2)$ mW. Taking into account the transmission of the cavity mirror, the peak power travelling inside the cavity is $P_T = (6.8 \pm 0.3)$ W. In all

our experiments, the lattice cavity was locked on 80% of this value with a side lock scheme. This means that typical power of the light in lattice trap in all the experiments is $P_{lattice} = (5.5 \pm 0.27)$ W, which corresponds to the trap depth of $U_0 = (56 \pm 2.7)$ recoil energies. In spite the rather low input lattice light power of 88 mW, the new lattice trap depth value is 2.5 times bigger than the one we used to have.

Another independent way to estimate the lattice trap depth is to measure the frequencies at which atoms oscillate in the trap (see section 4.2.1). These frequencies can be measured using a phenomenon called parametric excitation [64]. The principle of this phenomenon is that if parameters of the trapping potential vary periodically at twice the natural frequency of a harmonic oscillator, the oscillator absorbs energy from the trap and its own energy increases exponentially. Therefore modulating the depth of the lattice trap with twice the frequency of the atoms will heat them out from the trap. We performed an experiment in which the lattice trap depth was modulated at different frequencies with the help of an AOM installed on the path of the lattice light (see fig.4.19). The zero order of the AOM was coupled to the

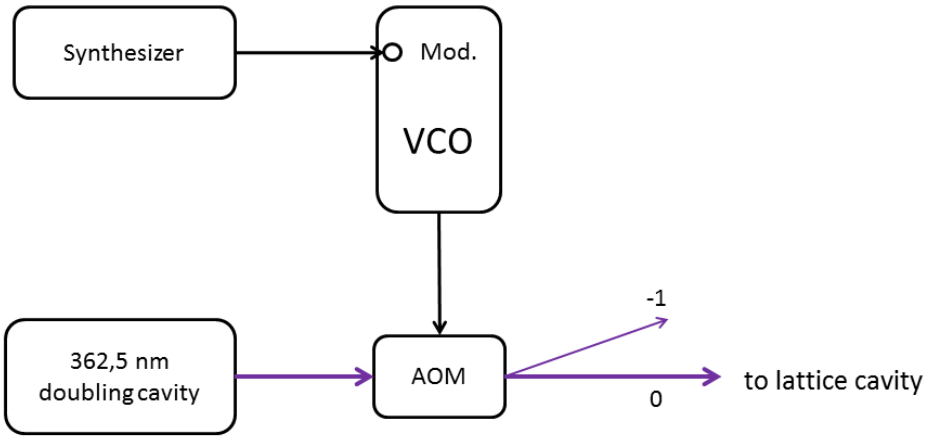

Figure 4.19. *Scheme of the parametric excitation experiment. Lattice light generated by 362 nm doubling cavity is coupled to a AOM, which is driven by a voltage-controlled oscillator (VCO). Output of the VCO is amplitude modulated at the frequency of a synthesizer. Zero order of the AOM is coupled to the lattice cavity.*

lattice cavity and the RF power sent to the AOM was modulated. The amplitude of modulation of the lattice light was $\approx 10\%$ of the total light power. The number of atoms still trapped after the time T_{dark} was reg-

istered at different modulation frequencies. On the figure 4.20 one can see the result of the experiment. Two experiments were done with dark time $T_{dark} = 80$ ms, one with continuous modulation of the trap depth during the whole cycle and the other with pulsed modulation, when the trap depth was modulated only during the dark time. An experiment with twice bigger dark time was done as well. As one can see from the figure the atoms are being completely expelled from the trap at modulation frequency around 200 kHz. We assume that the main mechanism via which atoms are being heated out from the trap is the excitation to the higher axial vibrational states. Taking into account that for parametric excitation the most efficient energy transfer happens when trap parameters are modulated at twice the frequency of the atom in the trap, we can conclude that the frequency at which atoms are oscillating in the trap in axial direction is close to ≈ 100 kHz. This result is in a good agreement with the theoretical value of

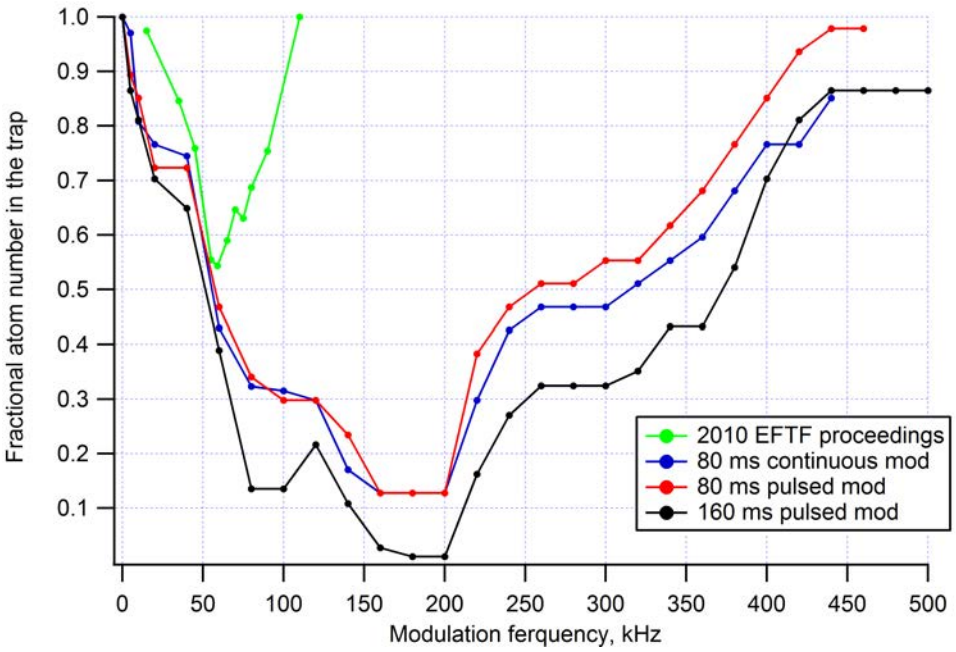

Figure 4.20. *Parametric excitation of atoms in the lattice trap induced by the trap depth modulation. Two experiments were performed with dark time of 80 ms. In one experiment depth of the trap was modulated during whole clock cycle (blue), in the second experiment depth of the trap was modulated only during dark time (red). The black curve is the result of the experiment in which the trap depth was modulated during dark time of 160 ms. The green curve is the similar measurement done for the old lattice trap (see [56]).*

110 kHz calculated based on the parabolic approximation (4.3) for the trap depth of 56 recoil energies. This means that our estimation of the trap depth is close to reality. The results of the parametric excitation with the old lattice trap are also presented on the figure in green color for comparison. As one can see from the graph with deeper lattice trap we were able to discover that parametric excitation has asymmetric shape. We attribute such a broad and strange shaped resonance to coupling between transverse and axial degrees of freedom and non-parabolic shape of the potential. This is a very interesting effect that can be the subject for future studies.

Atoms trapped in an optical lattice can acquire energy sufficient enough to surpass the potential barrier and leave the trap. The energy can be acquired in a several ways, for example it can come from an absorbed photon, can be transferred to the atom from the trap by resonance phenomenon or via collisions with background gas. As a result, atoms have a finite lifetime in the trap. This lifetime defines the maximum possible time of interrogation of trapped atoms with the probe light. To measure the lifetime of the new trap we performed an experiment in which atoms were first cooled and trapped in the lattice and after all the lights and magnetic fields except the lattice light were turned off for a time T_{dark} after which atoms were detected. Several cycles like this were done and in each cycle T_{dark} was incremented until the lattice trapped atom's signal disappeared. The resulting curve was approximated by an exponential decay with a time constant τ, which gives an estimation of a lifetime of the atoms in the trap. (see fig.4.21). The measured lifetime for the new lattice trap is $t_l = (373 \pm 48)$ ms for the ^{199}Hg isotope. This is good result comparing to the 250 ms that we had with the old lattice [61]. Taking into account that vacuum level in the chamber and therefore background collisions rate remained the same, higher lattice lifetime signifies deeper trap depth and better confinement of the atoms. Longer lifetime of atoms in the trap allows us to perform longer interaction light pulses and lower Fourier limit of our spectroscopy resolution. We think that the lifetime in our case is mainly determined by the collisions with background gases.

From our calculation based on the number of counts we are able to trap few tens of thousands of atoms in our new lattice, which is $\sim 2\%$ of MOT atoms. In order to check that this fraction is of the right order

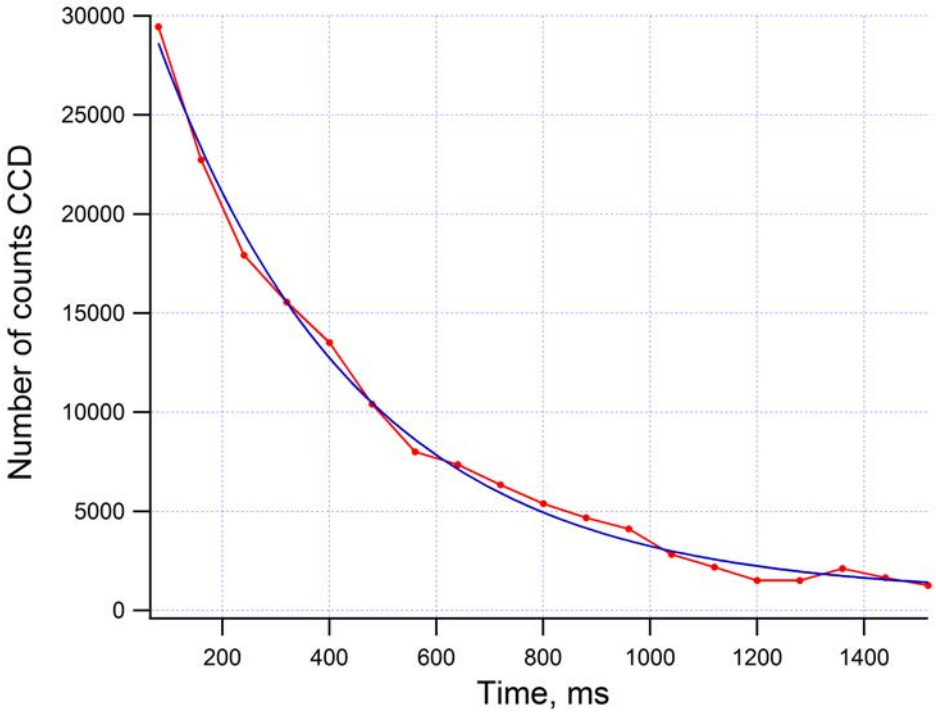

Figure 4.21. *Decay of the lattice trapped atoms signal as a function of time. Blue curve is the exponential decay fit. Lifetime of atoms in the trap estimated from the fit is* 373 ± 48 *ms.*

of magnitude and that the loading efficiency is really limited by the temperature of the atoms and the trap depth, we have calculated theoretical number of MOT atoms loaded in the trap. In our calculations we assumed that all atoms with a speed less than

$$v_{max} = \sqrt{\frac{2U_0}{m_{at}}} = 4\sqrt{\frac{P\alpha h}{\pi w^2 m_{at}}} \tag{4.8}$$

are being trapped. Here P is the power of the lattice light stored in the cavity, α is the polarisability and w is the trap waist. Then the fraction of MOT atoms, that have speed below v_{max} is

$$\int_0^{v_{max}} 4\pi v^2 \sqrt{\left(\frac{m_{at}}{2\pi k_b T}\right)^3} \exp\left(-\frac{m_{at}v^2}{2k_b T}\right) \mathrm{d}v. \tag{4.9}$$

To take into account the fact, that the lattice trap is smaller than the MOT cloud we estimated the overlap area of the two. In the vertical direction the lattice trap is bigger than the MOT and therefore the overlap in this direction is 100%. For the two other directions, since our aim

was to roughly estimate the loaded fraction, we simply integrated the MOT spatial Gaussian over the interval $[-\omega, \omega]$ separately in **x** and **y**. Finally the fraction of atoms of the MOT with a given temperature and size, that is being loaded in the trap can be written as

$$F(\omega, P) = \int_0^{v_{max}} 4\pi v^2 \sqrt{\left(\frac{m_{at}}{2\pi k_b T}\right)^3} \exp\left(-\frac{m_{at} v^2}{2k_b T}\right) \mathrm{d}v \times \\ \times \left(\int_{-\omega}^{\omega} \frac{1}{\sigma_x \sqrt{2\pi}} \exp\left(-\frac{x^2}{2\sigma^2}\right) \mathrm{d}x\right)^2 . \tag{4.10}$$

We had calculated the loaded fraction for different ω and P for the MOT cloud with radius $\sigma = 110$ μm and temperature $T = 70$ μK. The results are presented on the figure 4.22.

As one can see from the figure, for the trap with waist 69 μm and depth 56 recoil energies, which corresponds to 5.5 W of the light inside the lattice cavity, the calculated loaded fraction is 2.3%, which corresponds to few tens of thousands atoms and is in a good agreement with the value that we got from CCD counts. It is typical atom number that we get with rather modest total cooling light power of ≈ 50 mW. For comparison, with the old lattice trap we were able to trap in the best case around 2000 atoms. Therefore we already have one order of magnitude increase in trapped atom number (see fig. 4.23). These figures could be increased even more by realigning the Ti:Sa laser and change the 362 nm doubling stage optics and crystal. By our estimations a trap depth close to 100 recoil energies can be reached. However, already with available light power we had much higher signal of the atoms in the new lattice than before. Therefore we decided to not change the doubling stage optics and continue with existing trap depth devoting our time to spectroscopy experiments and stability measurement.

Increased atom number allowed us to perform spectroscopy with split Zeeman components, increase stability of the clock and measure statistical frequency shifts. All this is described in chapter 5.

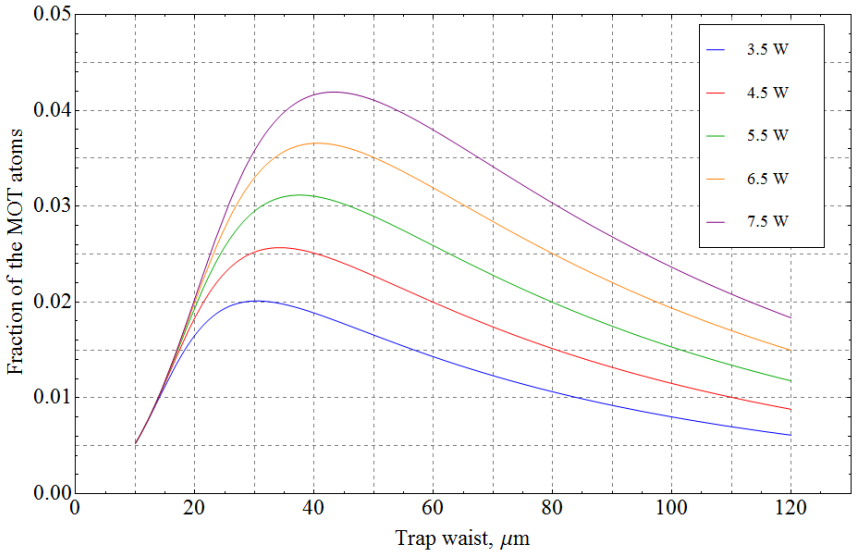

Figure 4.22. *Fraction of MOT atoms that are loaded in the trap, calculated for different trap waists and depths as a function of the lattice light power inside the lattice cavity.*

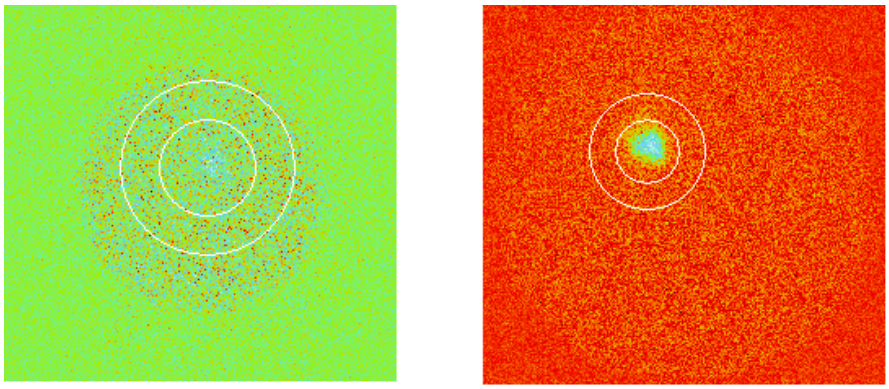

Figure 4.23. *CCD image of the lattice trapped atoms for the old (left) and the new (right) lattice traps. Note that the left figure is a signal of more abundant ^{202}Hg isotope, while the right figure is the signal of ^{199}Hg. Small white circle shows the area of interest and big white circle shows the area that is used in the background noise cancellation process. The big round shadow on the pictures is the iris installed in front of the CCD camera.*

Chapter 5

Spectroscopy experiments on $^1S_0$ - $^3P_0$ transition

In this section one can find description of the spectroscopy experiments and their results, which were done during this thesis. All the spectroscopy experiments reported here were performed with total (sum over all three MOT arms) cooling light power of ≈ 45 mW and the lattice trap depth $\approx 56\, E_{recoil}$.

5.1 Spectroscopy of $^1S_0$ - $^3P_0$ transition

Our first spectroscopy of the clock transition with the new lattice trap is shown on the figure 5.2. As one can see from the figure by chance we had coupling to all four Zeeman components of the clock transition. In previous spectroscopy experiments with the old lattice trap coupling to π and σ transitions was already demonstrated [39]. However, the signal to noise ratio with split Zeeman components was very poor and all previous stability and systematic shifts measurements were performed using lock on the single overlapped Zeeman component.

With the new lattice trap we have increased the trapped atoms signal by a factor of 10. Directly from our first spectroscopy of the ^{199}Hg clock transition we were able to achieve S/N ratio by a factor of > 2 higher than we ever had before in spite the fact that Zeeman components were split. The spectroscopy presented on figure 5.2 was performed with 15 ms and ≈ 22 μW probe pulse. Magnetic field, which

defines the quantisation axis, was directed from North to South, which is the direction from 2D-MOT to 3D-MOT (see fig.5.1). All four Zeeman

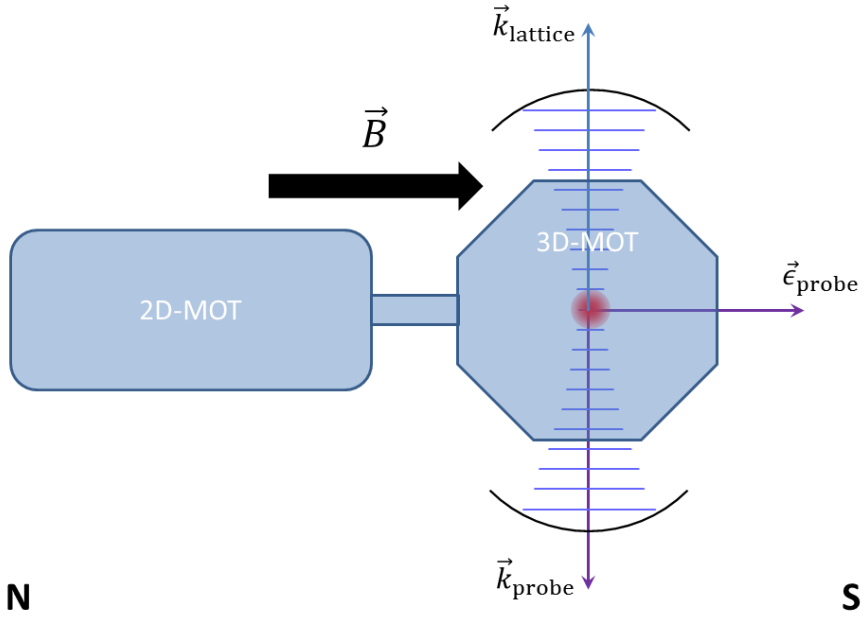

Figure 5.1. *Schematic view from side of the main chamber of the experiment. On the figure you can see 2D and 3D MOTs and vertically mounted lattice trap.* $\vec{k}_{probe}$ *and* $\vec{k}_{lattice}$ *are wave vectors of the probe and lattice light correspondingly,* $\vec{\epsilon}_{probe}$ *is the direction of the probe light polarisation.* $\vec{B}$ *is the direction of quantization magnetic field.*

components were coupled in this experiment, because by chance the linear polarisation of the probe light was oriented at 45° to the vector of the quantisation magnetic field. Spectroscopy shown on the figure 5.2 is the result of a single run with no averaging done. The signal on the figure is the trapped atom's fluorescence at 254 nm, registered by CCD camera. Dips in the signal correspond to decrease of number of atoms that contribute to fluorescence due to excitation to the dark (for the cooling light) $|^3P_0\rangle$ state by probe pulse.

Such S/N ratio will allow to lock our clock on split Zeeman components and suppress common mode effects that are introducing frequency shifts. Simultaneous coupling of all four Zeeman components was not needed in our following experiments and the polarisation of the probe light was rotated to be linear with the N-S magnetic field so only the π-transitions were coupled.

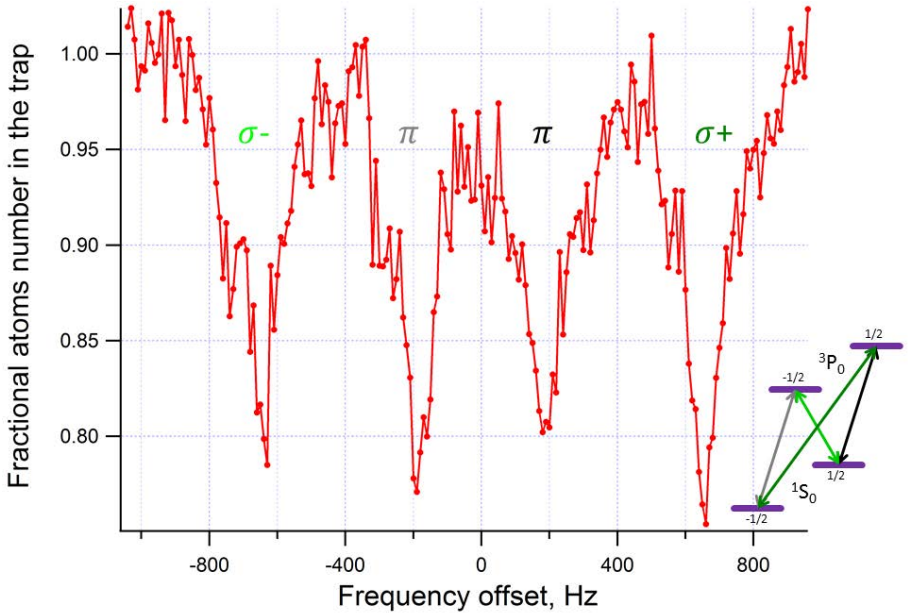

Figure 5.2. *Spectroscopy of ^{199}Hg clock transition with split Zeeman components.*

5.2 Measurement of magnetic field at trapped atoms site

We didn't managed to preserve the alignment of the lattice trap when we changed the lattice cavity, even though we were pretty close to it. In the end we had to change the value of the magnetic field components in horizontal plane in order to overlap the MOT with the new lattice trap. As the result the atoms are now trapped in a different place in space than before.

Since the magnetic field at trapped atom's site had changed, we had to measure value of the field in **x**,**y** and **z** directions to be able to properly orient the quantisation axis. To accurately measure the field we registered the value of the splitting of Zeeman components at different magnetic fields in all three dimensions. First we measured the magnetic field in N-S direction. This is the axis along which we had to apply a significant magnetic field in order to overlap the MOT with the lattice trap, which means that this component of magnetic field should be present in every experiment at least during the loading and compressing phases (see sec.3.2). Therefore in this experiment the coil that creates the overlapping magnetic field was kept at constant

current all the time and to vary the N-S magnetic field we used an additional, so called "sideways" coil that was turned on only during the dark time.

On the figure 5.3 one can see the distance between two π-transitions in Hz as a function of the magnetic field. Based on this data we determined the linear Zeeman effect coefficient for π-transition to be 3 ± 0.2 Hz/μT. Our measurement of the linear Zeeman effect coefficient is in good agreement with the theoretical value calculated as

$$\alpha_z = \frac{\delta g \mu_B s}{2\pi\hbar} \tag{5.1}$$

where s is the spin of ^{199}Hg and δg is the difference of Landé factors of the excited and ground states. We used value of δg calculated in [47]. One can notice that there is no experimental data for splitting

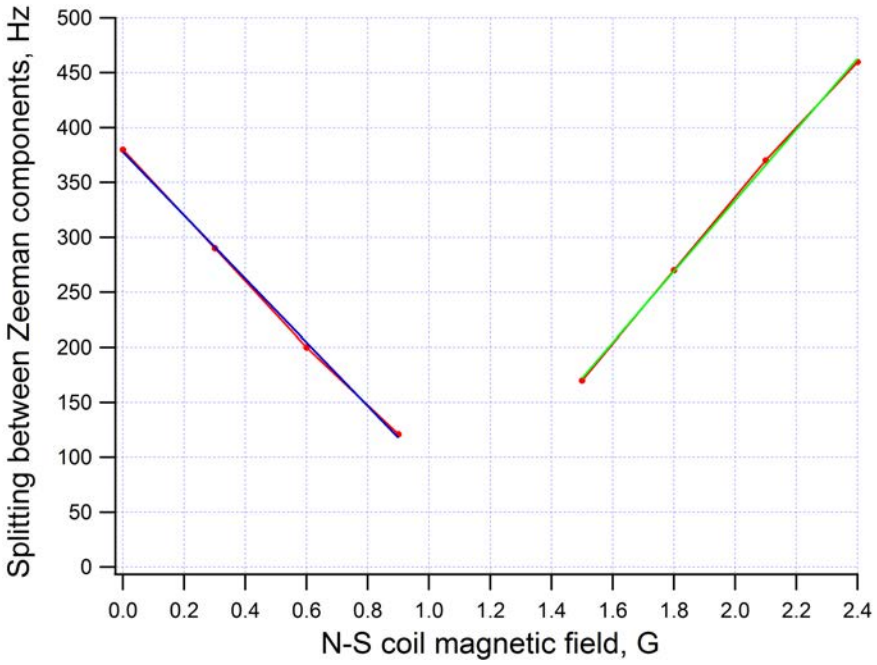

Figure 5.3. *Splitting between the two pi Zeeman components at different N-S fields values with linear fits. The experimental data is presented in red and two linear fits in blue and green.*

below 130 Hz on the graph. This is due to the fact, that there was magnetic field in perpendicular direction, which at some point became significant. Therefore with the decrease of N-S field the orientation of the quantisation axis was changing from being linear to perpendicular with respect to the probe polarisation. As the result coupling to

the π-transitions was decreasing until the transitions completely disappeared. However, by extrapolating the linear fits of the left and the right sides of the data and finding their cross point we could define the value of the field that had to be applied in N-S direction so that the resulting field would be 0. Typical configuration of our experiment with well defined quantisation axis corresponds to the situation when the overlapping magnetic field, which equals to 1.12 ± 0.04 G, is not compensated. The splitting between the two π-components in this case is 370 Hz.

Measurement of the magnetic field in two perpendicular directions was done as well. For this experiment during the probe time the N-S magnetic field component at trapped atoms site was set to 0 and an additional field was applied in perpendicular directions. The orientation of probe light polarisation didn't changed, which means that σ-transitions were coupled. On the figure 5.4 and 5.5 one can see splitting of Zeeman components for different values of magnetic field in W-E and vertical directions respectively. From the fit of the data on the figures we determined that magnetic field of 0.47 ± 0.011 G in W-E direction and 0.31 ± 0.037 G in vertical direction was present at the trapped atoms site. For better control of the direction of quantisation axis in subsequent experiments these fields were compensated during the probe time with the help of the coils that were creating magnetic fields of the same amplitudes but in opposite directions.

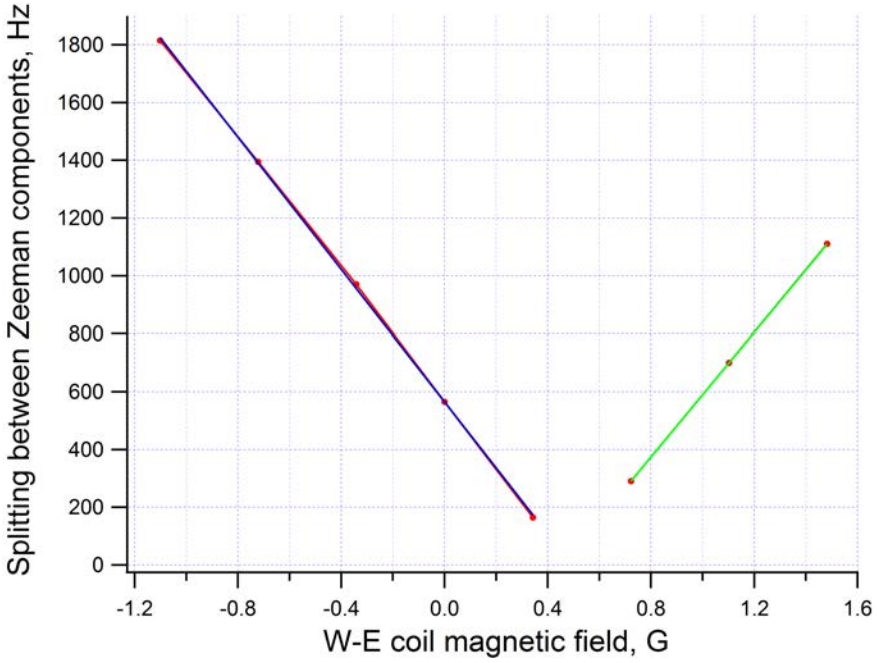

Figure 5.4. *Splitting between the two sigma Zeeman components at different W-E fields values. The experimental data is presented in red and two linear fits in blue and green.*

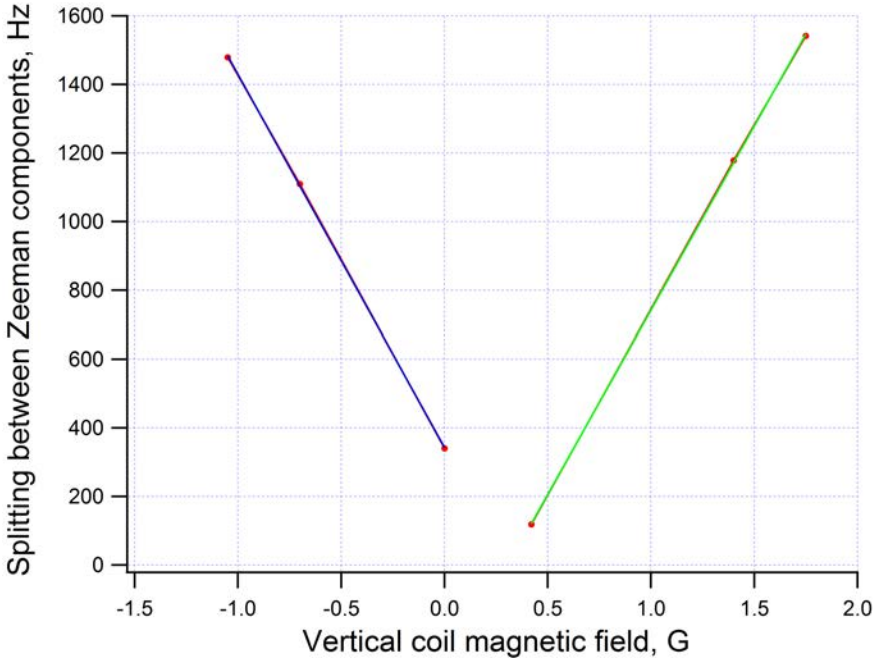

Figure 5.5. *Splitting between the two sigma Zeeman components at different vertical fields values. The experimental data is presented in red and two linear fits in blue and green.*

We have also measured the noise of the magnetic field in the laboratory room with the help of a 1D flux gate magnetometer. Results of the measurement of the magnetic field noise in all three directions over more than three days period are shown on the figure 5.6. As one can see magnetic field had the strongest noise in the vertical component, while the noise in two other directions was a factor of > 10 smaller. It is interesting to mention that the low noise segments, which can be seen on the graphs, coincide in time with the non-operational hours of an electric train line that is passing not far from the laboratory. This signifies that most of the magnetic field noise is coming from the power of electric train line. As it was said before, in almost all our experiments the quantisation axis was directed from North to South and the amplitude of the magnetic field was 1.12 ± 0.04 G. That means that the noise of the magnetic field in vertical direction at its worse was $< 2\%$ of the quantisation field value. Therefore perturbation of the quantisation field orientation induced by this noise is negligible. Noise of the magnetic field in S-N direction is at its worst 1×10^{-4} G, which corresponds to $\sim 3 \times 10^{-2}$ Hz frequency noise of a Zeeman π component. This noise will introduce relative instability of $\sim 3 \times 10^{-17}$ in case of locking on a single Zeeman component (see fig.5.7). However, linear Zeeman effect is a common mode effect. Common mode effects induce the same frequency shift for both Zeeman components, but with different signs, therefore these effects can be cancelled out by simultaneous lock on two Zeeman components and calculating the clock frequency as the mean frequency of the two components. This means that noise introduced by the magnetic field fluctuations will not limit the frequency stability of our clock in future.

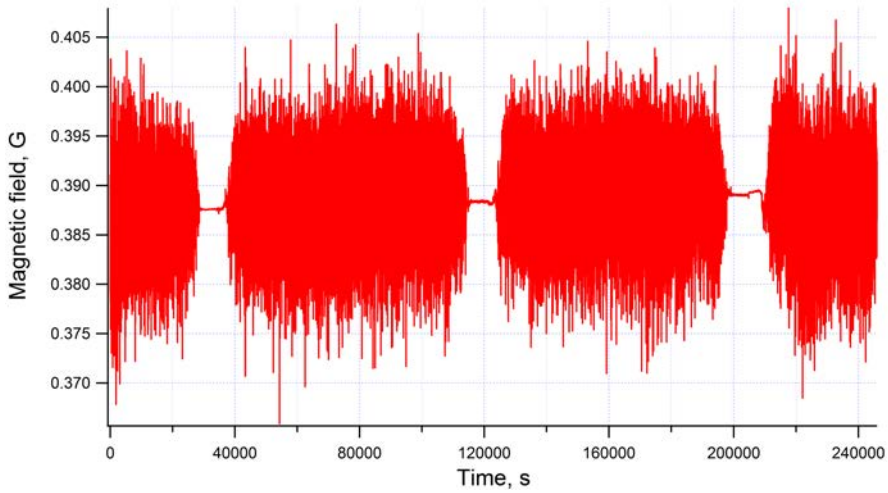

(a)

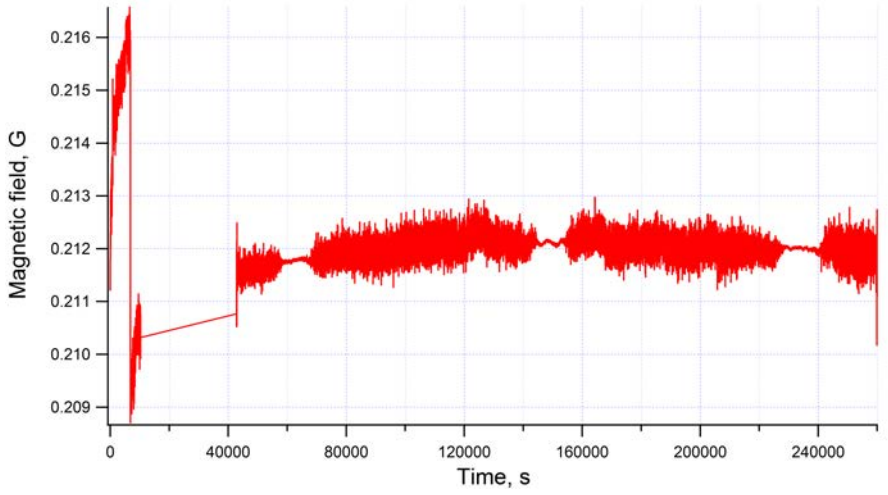

(b)

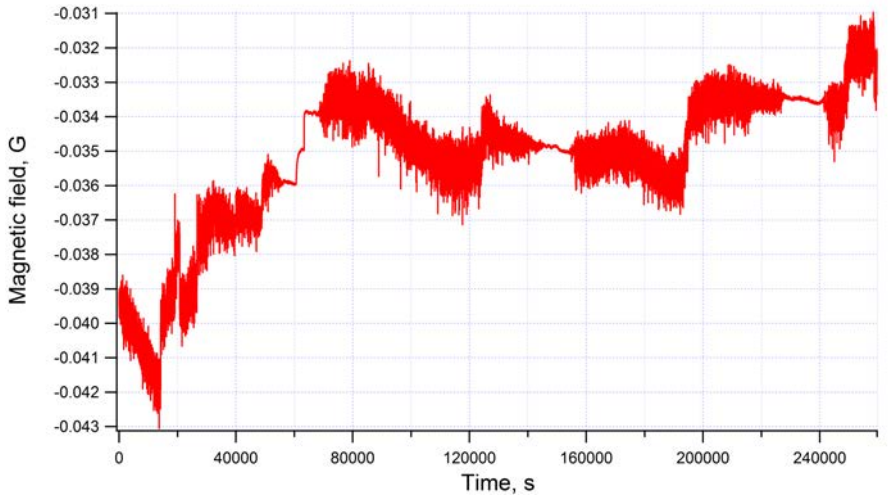

(c)

Figure 5.6. *(a) Magnetic field noise in vertical direction. (b) Magnetic field noise in N-S direction. (c) Magnetic field noise in W-E direction. Low noise segments on all three figures coincide with the non operation hours of the electric trains power line that passes nearby the laboratory.*

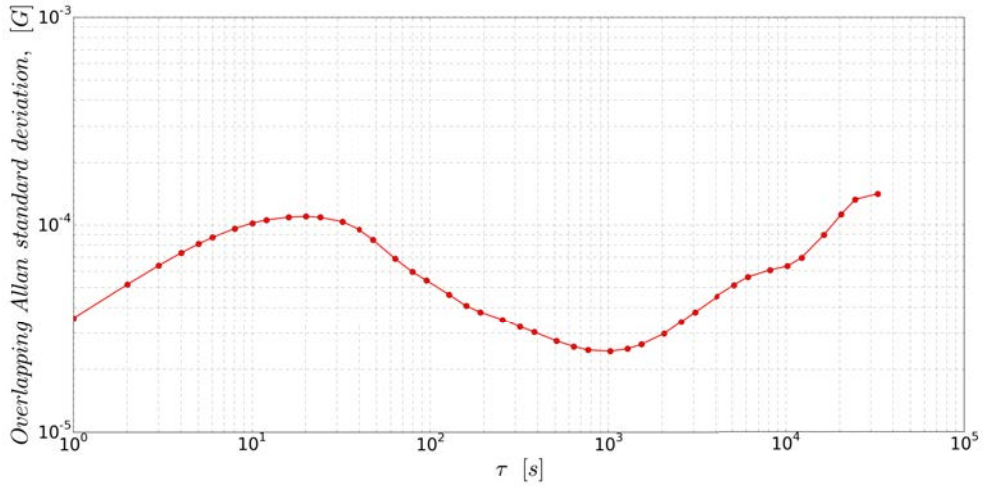

(a)

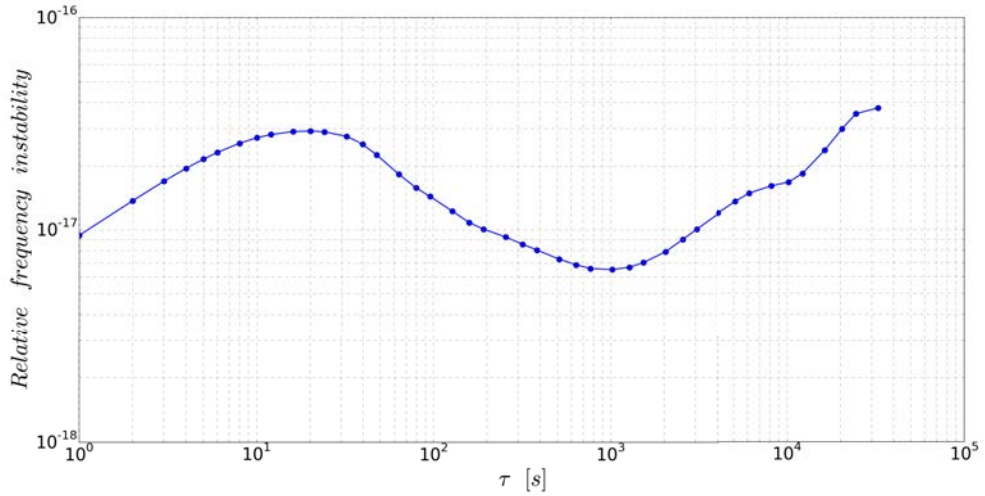

(b)

Figure 5.7. *(a) Allan deviation [65] of the high noise segment of S-N magnetic field fluctuations. Magnetic field in S-N direction defines the quantisation axis in our experiment. (b) Relative frequency instability introduced by fluctuations of magnetic field in the direction of quantisation axis (only linear Zeeman effect is considered).*

5.3 State selection and dark background

In our experiment detection is performed with atoms in the ground state via cooling transition. Which means that when the probe pulse excites atoms with a given spin orientation to the "dark" state $|\,^3P_0\rangle$ we detect it as a loss in the trapped atoms signal. With the implementation of the new lattice trap we increased the number of trapped atoms and noise of the atom signal is not any more dominated by the background noise of CCD camera. It is defined by the fluctuations of the trapped atoms number. In this case the noise is linearly dependent on the signal and further increase of the latter would not change the signal to noise ratio.

The main source of the atom signal fluctuations in our case was the frequency noise of the cooling light. This frequency noise affected not only the number of atoms in the trap but also the number of CCD counts per atom, since it depends on the detuning of the cooling light frequency from the cooling transition. An improved control of the frequency of the cooling light along with normalisation on the MOT signal are planned to be used in future to completely suppress these signal fluctuations. Another approach that allowed us to partly get rid of the noise introduced by the signal fluctuations was to perform a state selection and shift from detection on bright background (detection of a deep in the signal) for which the background noise is defined by the signal fluctuations, to detection of the signal on dark background, where background noise is defined by the dark noise of the CCD camera, which is a factor of ~ 10 smaller than the typical atoms signal fluctuations in our experiment.

To implement the state selection we had to couple an additional low power cooling light beam to the atoms through the top lattice cavity mirror. This beam was used to push the atoms away from the trap. Small amount of cooling light for the push beam was taken from the light propagating to the saturated absorption (see fig.3.1). Using an AOM the frequency of the push beam was tuned to be exactly on the resonance for the best efficiency. The AOM was also used to turn on and off the push beam, however an additional shutter was installed, to avoid any possible light leaked through AOM propagate to the atoms. The typical power of the push beam was measured to be ~ 250 nW and the waist at the trapped atoms site yielded from calculations based on

initial size and focusing power of the used lenses ≈ 200 μm. This was enough to completely damp the signal of the trapped atoms to the level of the CCD background noise with 5 ms long pulse.

Typical time sequence of the spectroscopy with state selection is shown on the figure 5.8. During the dark time we apply a relatively

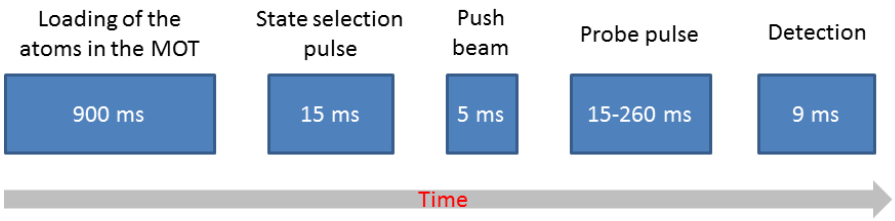

Figure 5.8. *Time sequence of spectroscopy experiment performed with state selection. The state selection pulse couples one of the two Zeeman components and excites atoms with a given spin orientation. After that the push beam removes from the trap all atoms in the ground state. As the result spectroscopy is done with spin polarized sample of atoms.*

short 15 ms Rabi π-pulse of the probe light that transfers 80% of atoms with a given spin orientation in the excited state. After this a 5 ms push pulse of cooling light is applied. The excited $|^3P_0\rangle$ state is a dark state for the cooling light and therefore all atoms that were excited by the first π-pulse do not see the push beam and stay in the trap, while not excited atoms are pushed away by the push beam. The third and the last pulse is a spectroscopy π-pulse with duration that can vary from 15 to 260 ms, depending on the goal of the experiment. This pulse transfers atoms from the excited state to the ground state where detection on the cooling transition is done using light of 2 MOT arms.

On the figure 5.9 one can see a spectroscopy of two split Zeeman components performed without state selection on the left and similar spectroscopy with state selection on the right. In both cases we detect fluorescence at 254 nm of the trapped atoms that are in both $|^1S_0, M_F = 1/2\rangle$ and $|^1S_0, M_F = -1/2\rangle$ states. Atoms are equally distributed between these states. The probe light pulse in our experiments couples one Zeeman component, for instance $|^1S_0, M_F = 1/2\rangle \rightarrow |^3P_0, M_F = 1/2\rangle$, and excites $\sim 80\%$ of atoms with $M_F = 1/2$. Excited state $|^3P_0, M_F = 1/2\rangle$ is a dark state for the 254 nm light and therefore after the probe light pulse only atoms with $M_F = -1/2$ contribute

to the signal and we see a dip 5.9(a). In the state selection scheme atoms in the state $|\,^1S_0, M_F = -1/2\rangle$ are removed from the trap by the push beam. This means that only atoms that were transferred from the $|\,^3P_0, M_F = 1/2\rangle$ to the $|\,^1S_0, M_F = -1/2\rangle$ state by the second probe light pulse will contribute to the fluorescence, which is represented by a peak of the signal on a dark background 5.9(b).

We lose about 40% of the signal during the state selection process due to imperfection of the first π-pulse, but we reduce the

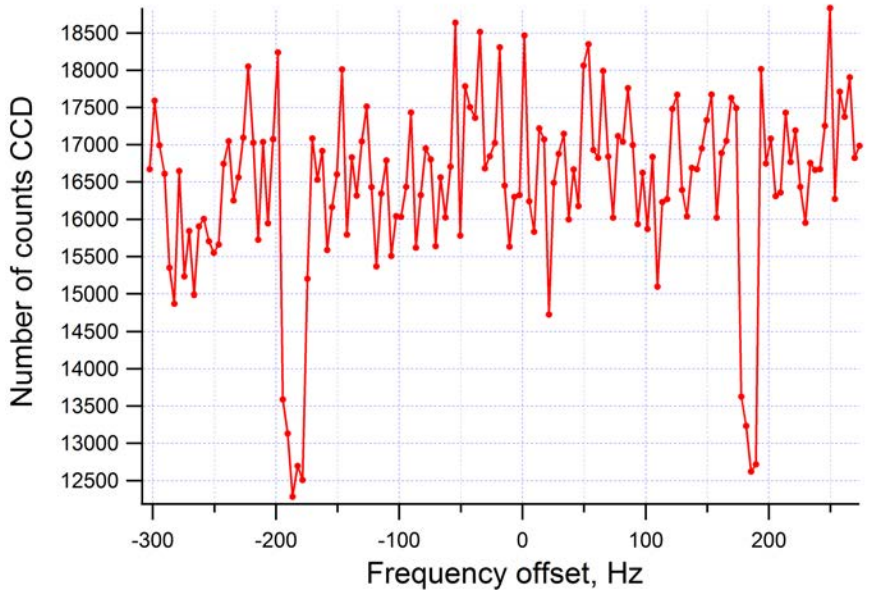

(a)

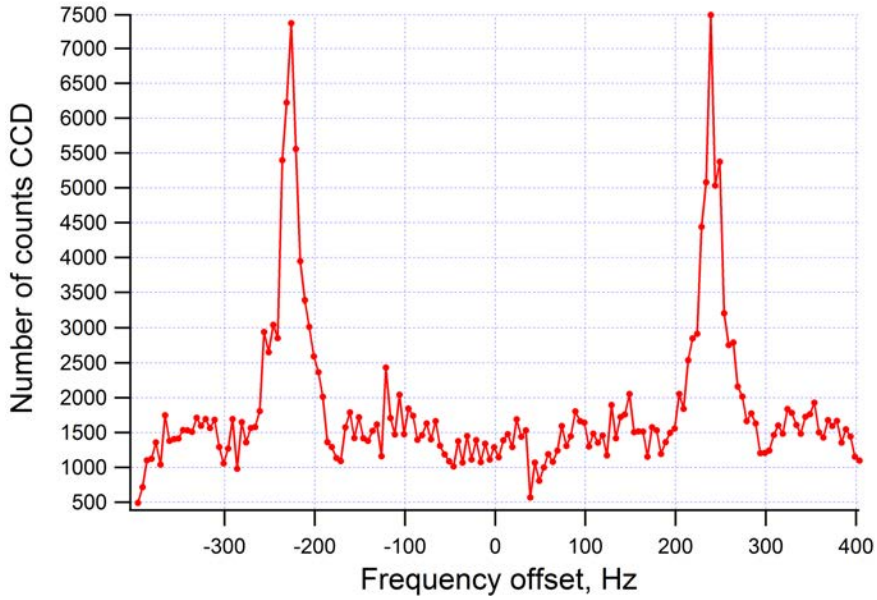

(b)

Figure 5.9. *(a) Spectroscopy of two π Zeeman components on bright background. (b) Spectroscopy of two π Zeeman components on dark background. Detection on dark background improved the S/N ratio by a factor of ~ 3.*

background noise by more than a factor of 3 and this noise does not depend on the trapped atoms number fluctuations any more. Therefore the state selection improved our signal to noise ratio. However, the signal itself is still affected by the cooling light frequency fluctuations. These fluctuations are the main limitation of the stability of our clock and as it was already said, can be removed which will further improve the stability of the clock.

Performing spectroscopy on the dark background also helped us to better resolve the Rabi oscillations (see fig.5.10). The data presented on the figure is averaged 5 times. From the fit of the data we can say that 15 ms and ≈ 20 μW probe pulse that was applied in this experiment corresponded to 1.1π-pulse in terms of Rabi oscillation phase. Thus it assured that we are using optimal width to power ratio for the most efficient excitation.

Both longer lattice lifetime and higher atomic signal allowed us to significantly increase the dark time of the spectroscopy experiments from 80 ms up to 320 ms. This means we could do spectroscopy with

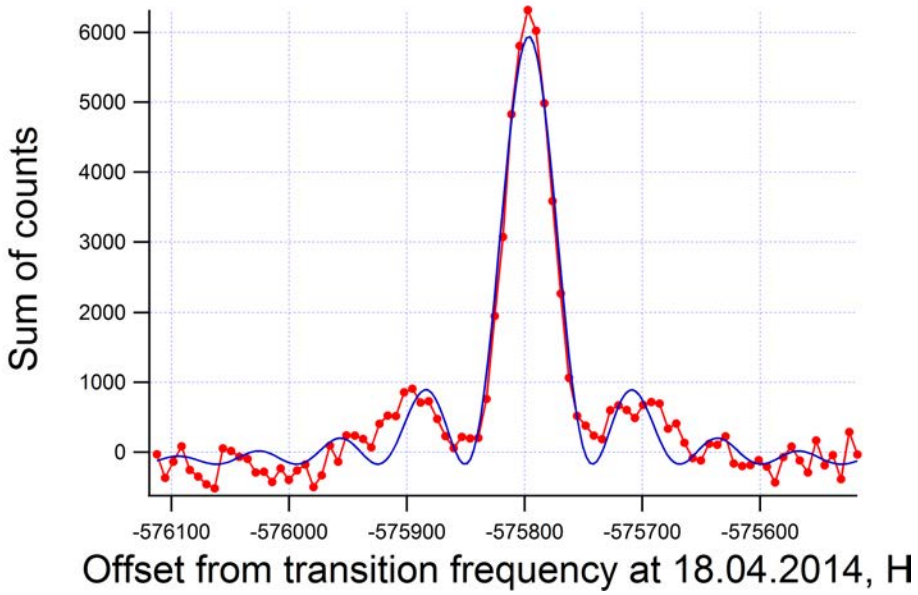

Figure 5.10. *Spectroscopy of one of the clock transition Zeeman components. The blue line is a fit of the data with a function of Rabi oscillations (see [66] page 304).*

longer probe pulses and lower the Fourier limit of the spectroscopy resolution. Result of a spectroscopy with probe pulse of 260 ms is presented on the figure 5.11. Here you can see 5 times averaged spec-

troscopy of one of the split π-transitions. From the Gaussian fit we estimate the FWHM of the transition to be 3 ± 0.3 Hz. This is a factor of more than 3 narrower than the best linewidth that we ever had with the old lattice trap. Unfortunately, the longer probe pulse we apply the less excitation efficiency we have, which leads to loss of the atoms that contribute to the signal and therefore worse S/N ratio. We had to find a trade off between narrowing the linewidth and at the same time keeping the S/N ratio high enough. We found that at the present situation the best stability is reached with 160 ms probe pulse and ≈ 6 Hz wide transition. All the experiments that are described below were performed with 15 ms state selection π-pulse, followed by 160 ms spectroscopy π-pulse.

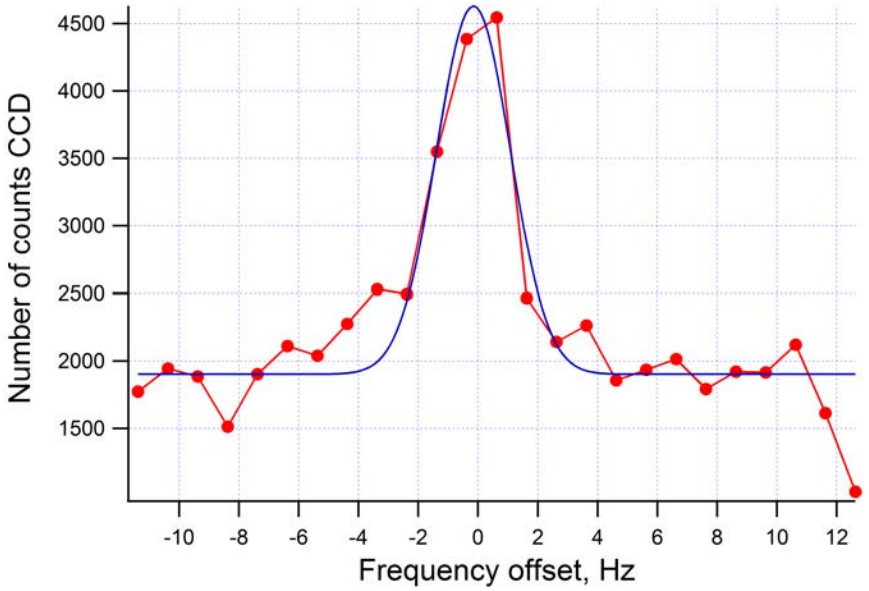

Figure 5.11. *Spectroscopy of one of the clock transition components with linewidth of* 3 ± 0.3 *Hz. Blue line is a Gaussian fit of the data.*

5.4 Frequency stability measurements

Frequency stability is one of the main characteristics of an atomic clock (see ch.1) and one would like to have a tool that would be able to extract as much information as possible from a set of frequency measurements and fully characterize the frequency stability of a clock. For instance, standard deviation is able to provide the overall stability over a set of data but it does not contain information about stability on a given time scale and does not allow to distinguish different types of noise. David Allan proposed to use two-sample variance, known today as Allan variance, to characterize the frequency stability of a clock. The Allan variance is a very powerful tool able to characterize stability of a clock on different time scales and to define which type of noise is limiting it [65]. Today Allan deviation, which is the square root of Allan variance, and modified Allan deviation are the two main tools commonly used to characterize frequency stability of clocks. The difference between these two is that in modified Allan deviation a weighted averaging over period of τ is used [65], which allows it to distinguish white and flicker phase noises, while for standard Allan deviation both of them have the same slope $1/\tau$. In all the experiments described below frequency stability of our clock was characterized using the standard Allan deviation.

To measure the frequency stability of our clock we locked its frequency to the frequency of the ^{199}Hg isotope clock transition and measured it over time. The lock was done by performing spectroscopy on the sides of the transition. We alternated the frequency of the probe laser ν between two values $\nu+\delta$ and $\nu-\delta$. We chose δ to be equal to the HWHM of the clock transition. Therefore if the unmodulated frequency of the probe light ν was equal to the frequency of the clock transition ν_0, the number of atoms excited by the probe light pulses with center frequencies $\nu+\delta$ and $\nu-\delta$ was the same. In case when $\nu \neq \nu_0$ the excitation efficiency of the two pulses and therefore the registered atom signal were different. In this case the correction of the clock frequency equal to

$$\Delta = (S(\nu+\delta) - S(\nu-\delta)) \cdot G \tag{5.2}$$

where $S(\nu)$ is the atom signal corresponding to the probe frequency ν and G is the gain, was applied via an AOM and the frequency of the probe light was shifted by Δ. The optimal value of the gain G was

calculated as $G = \frac{HWHM}{S(\nu_0)}$, where $S(\nu_0)$ is the atom signal exactly at resonance. As one can see, in this locking scheme the noise of the atom signal is converted to frequency noise. It is clear that low S/N ratio leads to probe light frequency fluctuations, which worsen the frequency stability of the clock.

As it was said before, with the new lattice trap and higher atom signal we were able both to increase our S/N ratio and to perform spectroscopy with smaller FWHM of the clock transition. This improved the short term frequency stability of our clock by a factor of ~ 5. On the figure 5.12 the measurement of the frequency stability of our clock locked to one of the split Zeeman components is shown. Blue squares correspond to Allan deviation of the raw data and red circles to Allan deviation of the same data, but with the linear cavity drift removed.

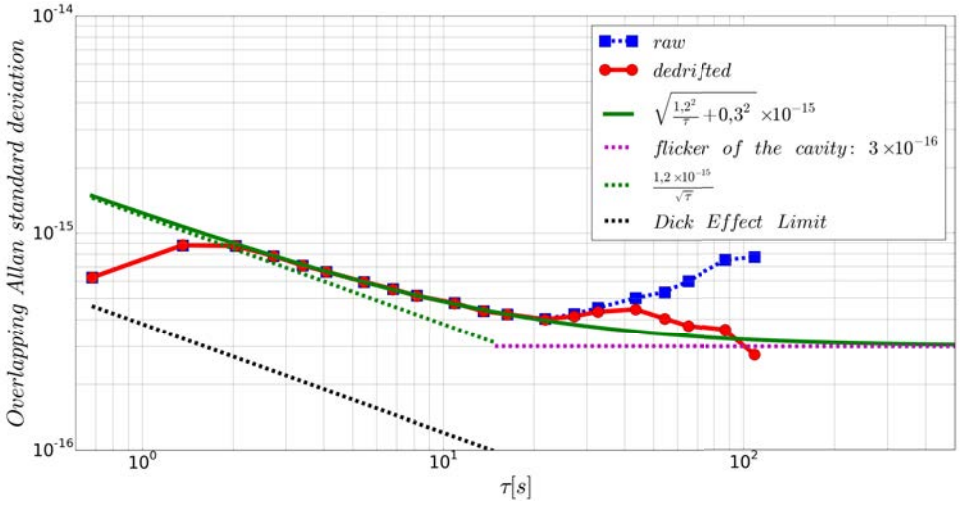

Figure 5.12. *Relative frequency stability of the clock locked to one of the Zeeman components. Frequency stability of our clock measured against the 10 cm long ultra-low expansion glass cavity with fused silica mirrors (blue squares) on the time scale* > 30 *s is dominated by the drift of the ULE cavity. This drift was numerically removed (red circles). The "de-drifted" curve on the time scale* > 100 *s is dominated by the flicker floor of the ULE cavity (dashed magenta line). The green line shows the square root of the sum of squares of the flicker floor of the ULE cavity and the slope of* $1.2/\sqrt{\tau}$.

Notice that the clock frequency is sensitive to the transient of the feedback loop. This fact affects Allan deviation of the clock frequency on short time scales and therefore the value of the Allan deviation on the time scale of several cycle times can not be treated as real frequency stability of the clock. Nevertheless the short term frequency stability of the clock can be estimated based on the middle term val-

ues of the Allan deviation. We can estimate the frequency stability of the clock at 1 second by approximating the midterm Allan deviation with $k/\sqrt{\tau}$ slope, which corresponds to the averaging of the Allan deviation of a signal dominated by the white frequency noise. This approximation is shown in green dashed line.

On the long term the Allan deviation of frequency corrections is affected by the drift of the USC, or if it is properly de-drifted as on the red curve, by the flicker floor of the USC, which corresponds to the magenta dashed line on the plot. The resulting instability introduced by the white frequency noise and the flicker floor of the USC is calculated as the square root of the sum of squares of the two, which is shown on the plot as the green solid line. As one can see from the approximation of the data by the sum of squares, the frequency stability of our clock at 1 second is $\sim 1.2 \times 10^{-15}$ and is limited at $\sim 3 * 10^{-16}$ on the long term by the flicker floor of the USC. This result is a factor of ~ 5 better than the best stability that we had with the old lattice trap [67]. The frequency stability measurement presented on the figure was performed with the cycle time of 0.684 s. The corresponding Dick effect limit for our probe laser is shown on the plot as black dashed line and one can see that it is much below the current frequency stability of our clock and is not a limitation in this case.

5.4.1 Interleaved lock

The possibility to resolve split Zeeman components with sufficiently big signal to noise ratio allows us to simultaneously measure frequencies of both components over time and use these measurements to determine the clock transition frequency with all the shifts due to common mode effects being cancelled. Using the same locking scheme that was described in the previous section, we did an experiment in which the frequency of the probe light was locked to one of the Zeeman components during n cycles and then switched to the other one for the next n cycles etc. As the result we obtained two sets of data with the frequency measurements of the two Zeeman components. To determine the center frequency of the clock transition we calculated the average frequencies $\overline{f_m^l}$ and $\overline{f_m^r}$ for each set of n cycles for the left and right components accordingly. The mean value of each pair $\overline{f_m^l}$

and $\overline{f_m^r}$

$$\nu_m = \frac{\overline{f_m^l} + \overline{f_m^r}}{2} \tag{5.3}$$

corresponds to the center frequency of the clock transition. Such measurement of the clock transition frequency is free from frequency fluctuations introduced by common mode effects. These frequency fluctuations are being naturally cancelled during the averaging with no need for corrections often based on complicated mathematical models.

On the figure 5.13 the result of the interleaved frequency measurement with two split π-transitions is shown. In this measurement the frequency of the probe light was locked subsequently to each component during 20 cycles. On the figure you can see Allan deviation of the mean frequency value of the two components measured against the cryogenic oscillator in blue color and against the Sr clock, which is located in the neighbouring laboratory, in magenta. The red curve is Allan deviation of the difference frequency of the two components. As you can see from the figure, the magenta curve is lower than the red curve below 200 s, which means that the stability of the mean clock frequency, for which common mode effects are compensated, is better than the stability of the differential frequency affected by these effects. This shows that interleaved integration compensates for com-

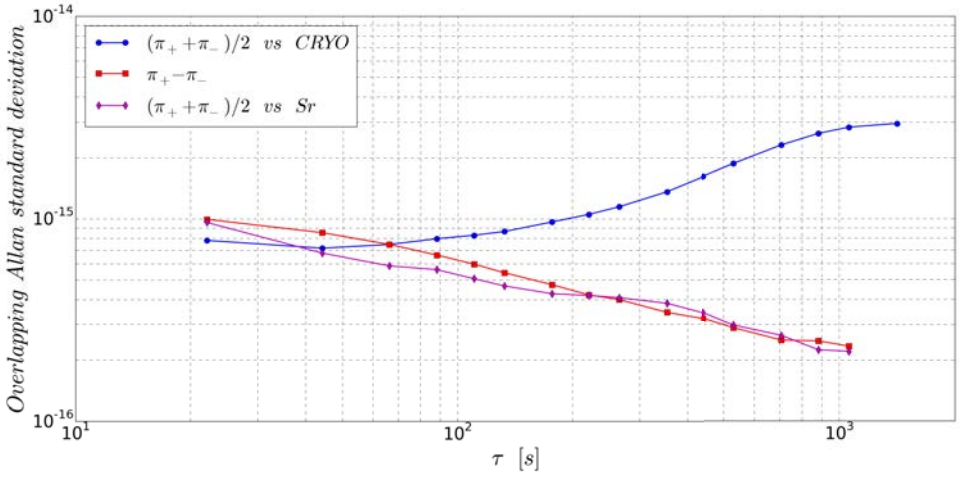

Figure 5.13. *Allan deviation of the relative mean frequency of the two π components measured against cryogenic oscillator in blue and Sr in magenta colors. The red curve is the Allan deviation of the difference frequency of the two π components.*

mon mode effects and improves stability and accuracy of the clock.

Notice that, in order to be able to compare the stabilities of the sum and difference frequencies of the two components, the measurement of the clock mean frequency had to be done against a reference more stable than the cryogenic oscillator, which in our case was Sr lattice clock.

This was our first attempt to lock on both Zeeman components with an interleaved lock scheme. Monitoring the frequency of a single component during n cycles and then leaving it untracked for the next n cycles, was the fastest and easiest scheme to implement and yet good enough for the test. In the future a more sophisticated interleaved scheme will be implemented, that will allow to track frequencies of both Zeeman components quasi-simultaneously without long interruptions, which will further improve the frequency stability of the clock.

5.5 Systematic shifts

5.5.1 Collision shift

Another effect that also introduces a frequency shift of the clock transition are collisions of cold atoms. In quantum mechanics the collision process is described as a scattering of the wave function of a particle with effective mass on a stationary scattering center with a field $U(r)$. It can be shown that the solution of the Schrödinger equation that describes such scattering process can be represented as a superposition of wave functions

$$\psi = \sum_0^\infty \psi_l \tag{5.4}$$

that correspond to the movement of a particle with a given energy $\hbar^2k^2/2m$ and different values of angular momentum l in the field $U(r)$[68]. This is called partial wave expansion and functions ψ_l are called partial waves. Partial waves with a certain l are called s-wave, p-waves, d-waves etc, similarly to the momentum of an electron in an atom.

The less the energy of the colliding atoms the less the probability that collisions will happen via high order momentum channels. For sufficiently cold atoms the high order wave collisions are frozen-out and only s-wave remains. This is called s-wave regime. Notice, that for

fermions s-wave collisions are forbidden by Pauli exclusion principle and therefore at low enough temperatures collisions between fermions should be absent. However, even though the probability of p-wave collisions is very small at low temperatures it is not zero and the residual p-wave collisions should be considered, which means that in our case a non-zero collision frequency shift for ^{199}Hg isotope can exist.

We have performed a series of spectroscopy experiments, in which a differential measurement of the clock transition frequency at various trapped atoms densities was done. These experiments were performed with state selection, which means that the spectroscopy was done only with spin polarized atoms in $|^3P_0\rangle$ state. Using the interleaved lock scheme described in the previous section we have measured the clock transition frequency for configurations with different densities. In order to be sure that the frequency shift arises due to the density variation and not due to other effects we used two different approaches to change the density of the atoms. In the first approach the density of atoms was modified via change of the MOT loading time. However, variation of the MOT loading time can lead not only to a different number of atoms loaded in the trap, but also to a different temperatures of the atoms and MOT cloud size. This would affect spatial distribution of the atoms in MOT and consequently the density of the atoms in the lattice trap.

In order to measure the collisional shift induced only by density variations due to atom number change, but not due to spatial distribution variation, we performed a second experiment, in which the atomic samples were prepared in exactly the same way, but for low density configuration the duration of the state selection pulse was changed, while the power of the light remained the same. As the result less atoms were excited to the $|^3P_0\rangle$ state and kept in the trap after the push beam pulse.

The difference between the frequencies measured at low and high densities for both approaches is shown on figure 5.14. The weighted mean frequency shift and standard deviation for both are shown in the table 5.1. From these measurements we can conclude that we do not see measurable frequency shift due to atom collisions at the 10^{-16} level.

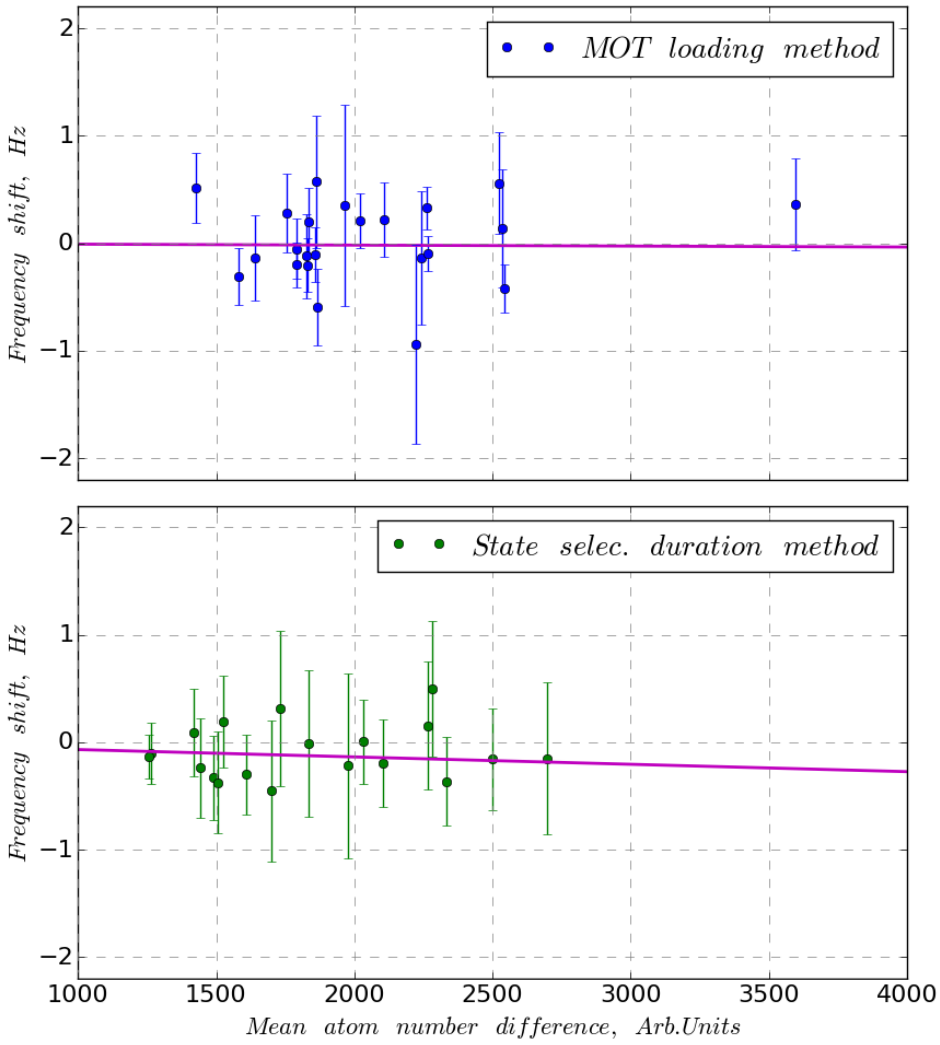

Figure 5.14. *Collisional shift for two methods of density variation via MOT loading time change (in blue) and via state selection pulse duration change (in green). Magenta lines on both figures represent weighted linear fits.*

One can notice that the linear fit of the data presented on the bottom figure has a non zero slope. We attribute this slope to the frequency shift introduced by the AOM, which is used to form the state selection pulse. The optimal RF power that we have to apply to this AOM in order to create proper state selection pulse is ~ 2 W. Such an amount of power heats up the crystal of the AOM, which could lead to a significant change of the refractive index and as a result of the phase that is acquired by the probe light during the propagation through the crystal. In this case reduction of the state selection pulse length will induce a frequency shift. This effect will be carefully investigated in future.

Table 5.1. *Collisional shift summary.*

	Weighted mean shift ($\times 10^{-17}$)	One standard deviation ($\times 10^{-17}$)
MOT loading time	-2.0	5.5
State selection pulse duration	-10.9	8.5
Combined	-4.7	4.6

Lattice trapped atom density

We had estimated the density of atoms in the lattice trap based on the density of our MOT cloud. Typical number of counts of the MOT atoms is $\approx 2 \times 10^6$. Based on this value we calculated the typical number of atoms in the MOT to be $N_M \sim 570000$ (see eq.3.2, 3.3, 3.6). From the ballistic expansion of the MOT (see ch. 3.2) we know, that the cloud has Gaussian shape with almost equal radii in **x** and **y** directions, which are the axes of the plane seen by CCD camera. In **z** direction the gradient of the magnetic field is twice bigger, since it is the direction of the MOT coils axis. From the equipartition theorem we have

$$\frac{1}{2}k_z r_z^2 = \frac{1}{2}k_b T \tag{5.5}$$

where k_z is the spring constant in z direction and r_z is the radius of the MOT cloud. k_z linearly depends on the magnetic field gradient, therefore in **z** direction its twice bigger than in **x** and **y**. This according to (5.5) means that the MOT cloud has radius in **z** direction $\sqrt{2}$ smaller in comparison with **x** and **y**. The MOT volume then equals to the volume covered by the three dimensional Gaussian with $\sigma_x = \sigma_y = \sqrt{2}\sigma_z$, which equals

$$V = (\sqrt{2\pi})^3 \frac{\sigma_x^3}{\sqrt{2}}. \tag{5.6}$$

Estimated MOT peak density corresponding to the volume of the MOT with $\sigma_x = 110$ μm radius is

$$\rho_m = N_M/V \sim 3 \times 10^{10}\, cm^{-3} \tag{5.7}$$

As in case of MOT we used CCD counts to calculate typical number of lattice trapped atoms that yielded $N_L = 11000$, which corresponds to the $\eta = \frac{N_L}{N_M} = 0.019$ fraction of the MOT. The density of atoms in the lattice trap is estimated from

$$\rho_l = \rho_M \cdot \eta \sim 7 \times 10^8\, cm^{-3}. \tag{5.8}$$

This is the density of atoms in the trap directly after the release of the MOT. We have to take into account the state selection, that is done before the spectroscopic probe pulse. During the state selection we keep $\approx 40\%$ of atoms, while the rest is blown away with the push beam. Therefore the resulting density of atoms before the spectroscopy is

$$\rho_l' = \rho_l \cdot \eta \times 0.4 \sim 3 \times 10^8\, cm^{-3}. \tag{5.9}$$

From what was said above we can conclude that we do not observe measurable collision shift for ^{199}Hg isotope at 10^{-16} level for densities $\sim 10^8$ cm^{-3}.

5.5.2 Lattice light shift estimation

As it was discussed in the section 2.3.2 the lattice trap light introduces a frequency shift of the clock transition, unless the wavelength of the lattice light is exactly equal to the magic wavelength. The frequency of the lattice light in our experiments was set to be close to the magic value measured in [39], however it was not locked to any

reference and was freely drifting around. In order to estimate the instability introduced by the lattice light frequency fluctuations we have measured the deviation of the lattice light frequency from the magic frequency (826.85 THz) with time. The frequency of the lattice trap was measured by a commercial wavemeter with resolution of $\sim$ 500 kHz manufactured by "HighFinesse" company. The Allan deviation of the frequency is shown on the figure 5.15 in red color. As you can see the frequency of the lattice light has a linear drift on the long term scale. In order to compensate for this drift we implemented an integral lock of the lattice light frequency to the magic value using data from the wavemeter and applying feedback to the PZT of the Ti:Sa laser (see fig.3.14). The frequency of the lattice light locked to the magic value with different integration time constants is also presented on the figure 5.15.

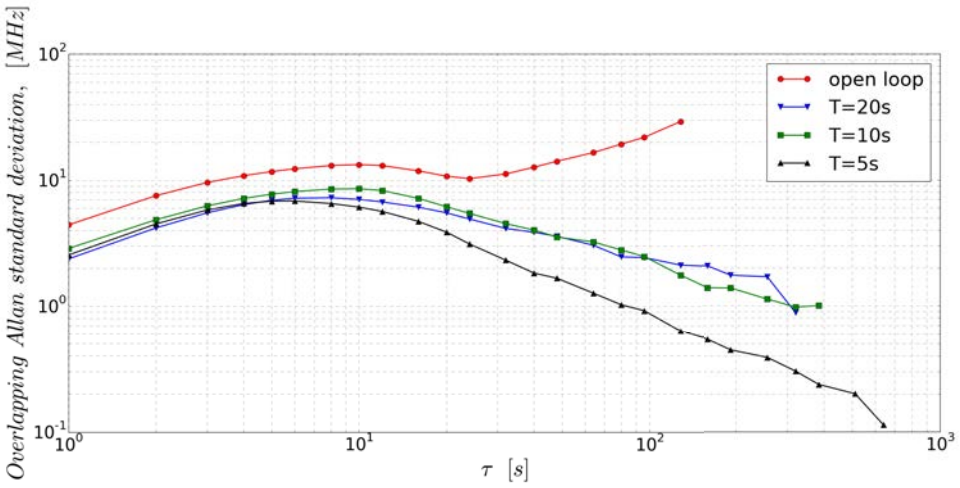

Figure 5.15. *Stability of the lattice light frequency with time measured for different configurations of the frequency control system: open loop (red), integration time constant of the loop T=5 s (black), T=10 s (green) and T=20 s (blue).*

We calculated the light shift introduced by the lattice light using the slope -57 mHzE_R^{-1}GHz^{-1} that was measured in [39]. On the figure 5.16 one can see the instability introduced by the frequency noise of unlocked lattice light in red and light locked to the magic frequency with integration time constant T=5 s in blue. The $k/\sqrt{\tau}$ approximation slopes that corresponds to the present clock frequency stability (see fig.5.12) and to the Dick effect limit are shown in red line and black dashed line respectively. The Dick effect frequency stability limit is

caused by the frequency noise of the probe laser and the presence of the dark time in clock operation cycle, during which the probe light does not interrogate with atoms [69]. As you can see from the fig.(5.16)

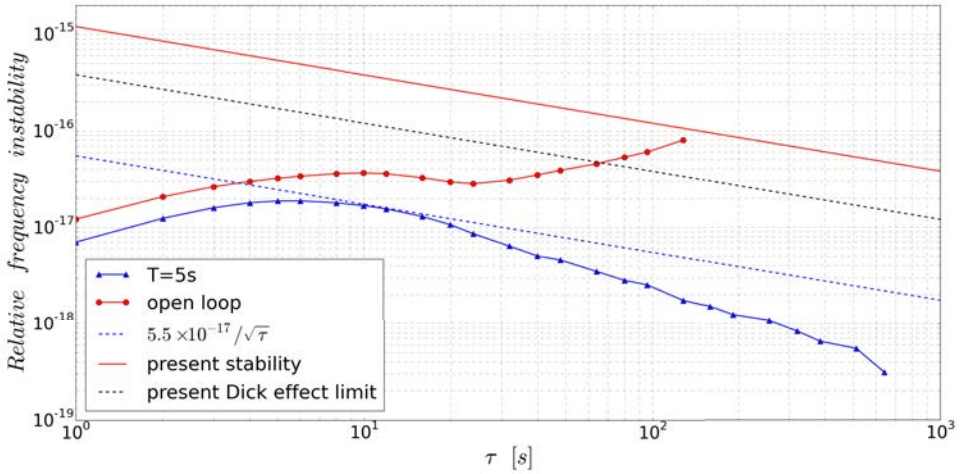

Figure 5.16. *Relative instability of the clock induced by lattice light frequency fluctuations. Frequency control of the lattice light reduces introduced relative instability below* 5.5×10^{-17} *at 1 s.*

on the time scale below 100 s the clock frequency instability introduced by the fluctuations of the lattice light frequency is much lower than the slope of $1.2 \times 10^{-15}/\sqrt{\tau}$ corresponding to the best measured stability of our clock. This means that lattice light frequency fluctuations on the time scale below 100 s at present situation do not limit the frequency stability of our clock. However, after 100 s frequency drift of the lattice light frequency becomes significant and limits the frequency stability of the clock ("open loop" curve on the fig.5.16). The lock of the lattice light to the magic wavelength removes the frequency drift ("T=5s" curve on the fig.5.16) and frequency instability of the clock introduced by the lattice light becomes significantly smaller than the Dick effect limit, which means that lattice light shift has no impact on the clock frequency stability at its present limits.

5.5.3 Second order Zeeman shift

It was shown in section 5.4.1, that a clock is insensitive to 1st order Zeeman effect when its frequency is being defined as the mean frequency of the two Zeeman components, nevertheless there is smaller

2nd order Zeeman shift that must be considered for high accurate clocks. For ^{199}Hg , since the ground state of the clock transition has **L** and **S** equal to 0 and for the excited state **J**$= 0$ the quadratic Zeeman shift comes from interaction of the fine-structure levels of the excited state. The quadratic Zeeman shift is dominated by the interaction of $|^3P_1, F = 1/2\rangle$ and $|^3P_0, F = 1/2\rangle$ states and can be approximated as (e.g. see [70])

$$\delta\nu_{z2} \cong -\frac{2\mu_B^2}{3\nu_{10}h^2}B^2 = -\beta_z B^2 \tag{5.10}$$

where $h\nu_{10}$ is the energy separation between $^3P_1$ and $^3P_0$.

We have performed an experiment in order to measure the 2nd order Zeeman constant β_z for ^{199}Hg . In this experiment the clock was locked to both π Zeeman components using the interleaved configuration (see sec. 5.4.1). The clock frequency was calculated as the mean value of frequencies of the two components. We have measured shift of the clock frequency between two configurations: a reference configuration and a configuration in which value of the magnetic field was changed with respect to the reference configuration. The result of the measurement is presented on the figure 5.17. On the figure you can see the clock frequency shift due to 2nd order Zeeman effect plotted versus the value of linear Zeeman splitting of the two components (blue dots) and a weighted linear fit of the data (dashed red line). The slope determined from the linear fit is $\gamma = (1.43 \pm 1) \times 10^{-7}$ 1/Hz. The coefficient β_z can be derived from the slope by multiplication on the linear Zeeman coefficient squared $\beta_z = \gamma\alpha_z^2 = (1.3 \pm 1) \times 10^6$ Hz/T^2 (here α_z is the linear Zeeman coefficient measured in section 5.2). This value is in a good agreement with similar measurement that yields $1.6(2) \times 10^6$ Hz/T^2 reported by H. Katori et al. [71]. Based on our measurement we have calculated the 2nd order Zeeman relative frequency shift to be $(2.4 \pm 1.8) \times 10^{-16}$ for the maximum value of the magnetic field $B_{max} = 4.6 \times 10^{-4}$ T that we ever applied in our experiment and $(1.4 \pm 1) \times 10^{-17}$ for typical value of the magnetic field $B_0 = 1.1 \times 10^{-4}$ T.

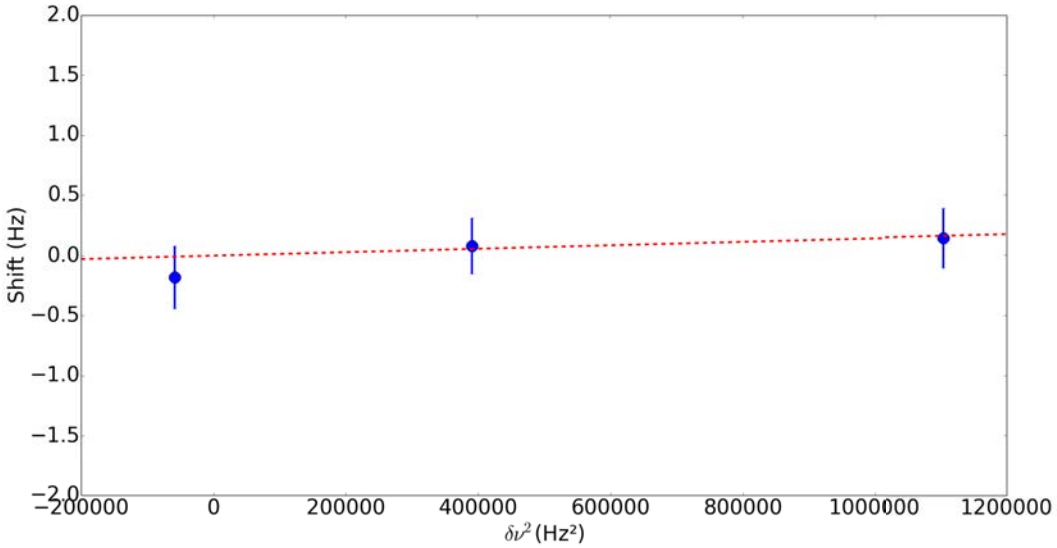

Figure 5.17. *Clock frequency shift due to 2nd order Zeeman effect measured as frequency difference between a reference configuration and configurations with different values of magnetic field (blue dots). The x axes is the square of the linear Zeeman splitting of the two components. Red line is a weighted linear fit.*

Chapter 6

Conclusion

At the beginning of this thesis, the performance of the experiment had reached its limit and several major technical issues had to be adressed in order to exploit all the advantages of a mercury-based frequency standard that I outlined in chapter 2. During my PhD thesis I designed, implemented and tested two major technical improvements of the experimental setup.

The first improvement concerned the cooling light laser source. First, I solved a repetitive technical problem in the design of the cooling system that caused the malfunction of the whole laser and needed to be replaced. Using a new pump module from another supplier with a better design including different cooling system significantly improved reliability of the laser system. I also have designed and implemented a new doubling stage at 254 nm for the cooling laser system that placed the doubling cavity with all its optics in a pure oxygen atmosphere in order to reduce the damage of optics coating and non-linear crystal itself caused by exposure to high-power UV light. Both improvements had increased the reliability of our cooling laser system and allowed us to perform spectroscopy with longer integration times, which was absolutely necessary for the measurement of the stability and systematic uncertainties of our clock.

The second and the most important improvement that I have realised, was the change of the lattice trap cavity. It involved breaking vacuum in the main experiment chamber and therefore, several tests of the new lattice cavity mirrors and a lot of preparation work had been done before the implementation of the new trap. The main goal was to increase the depth of the lattice trap, which would result in increas-

ing the trapped atoms signal and strength of the confinement in the trap. These pushed further limits of the experiment, increased stability of the clock and allowed to measure systematic frequency shifts with higher precision.

As the result of all the technical improvements the depth of the lattice trap was increased by a factor of 3 with capability of further increase up to $100\ E_R$ with reasonable effort done on increasing the power of the lattice light. Spectroscopy of the clock transition with record linewidth of 3 ± 0.3 Hz was performed. The relative frequency stability of the clock was improved to be 1.2×10^{-15} at 1 s, which is a factor of 5 better than it was ever obtained. This translates in 25 times less measurement time required to achieve a given accuracy. We have implemented spin polarisation via optical pumping and interleaved lock on two split Zeeman components.

All these improvements allowed us to switch from spectroscopy experiments to operation of the experimental setup as a clock. This was demonstrated by performing a comparison of our Hg clock against more stable and accurate Sr optical lattice clock, located in the neighbouring laboratory. We made more accurate measurement of systematic shifts, demonstrated that we do not see any measurable frequency shift due to collision of atoms as well as due to the second order Zeeman effect at a level as low as 1×10^{-16}. We have also measured frequency fluctuations of the lattice light laser source and estimated the instability introduced by these fluctuations to be below 5.5×10^{-17}. We can conclude that present stability of the clock is limited by the trapped atom number fluctuations. This limit will be removed in the near future by performing normalisation on the MOT signal. Taking into account results of the measurements of systematic shifts done in this thesis, we expect the stability of the clock to be limited by Dick effect, after the normalisation will be implemented.

Bibliography

[1] Bureau International des Poids et Mesures. In: *Comptes Rendus des séances de la 1e CGPM* (Paris, France 1889. BIPM).

[2] Bureau International des Poids et Mesures. In: *Comptes Rendus des séances de la 13e CGPM* (Pavillon de Breteuil, F-92310 Sévres, France 1967/1968. BIPM).

[3] Ch. J. Bordé. "La réforme du système d'unités". In: *La lettre de l'Académie des sciences* (2008).

[4] Bureau International des Poids et Mesures. In: *Comptes Rendus des séances de la 17e CGPM* (Pavillon de Breteuil, F-92310 Sévres, France 1983. BIPM).

[5] J. Guéna et al. "Progress in atomic fountains at LNE-SYRTE". In: *Ultrasonics, Ferroelectrics and Frequency Control, IEEE Transactions on* 59.3 (2012), pp. 391–410. DOI: 10.1109/TUFFC.2012.2208.

[6] Thomas P Heavner et al. "First accuracy evaluation of NIST-F2". In: *Metrologia* 51.3 (2014), p. 174.

[7] S Weyers et al. "Distributed cavity phase frequency shifts of the caesium fountain PTB-CSF2". In: *Metrologia* 49.1 (2012), p. 82.

[8] N. B. Phillips J. A. Sherman M. Schioppo J. Lehman A. Feldman L. M. Hanssen C. W. Oates A. D. Ludlow K. Beloy N. Hinkley. "Atomic clock with 1x10-18 room-temperature blackbody Stark uncertainty". In: *Phys. Rev. Lett* 113 (2014), p. 260801.

[9] Ichiro Ushijima et al. "Cryogenic optical lattice clocks". In: *Nat Photon* advance online publication (Feb. 2015), pp. –.

[10] J. Lodewyck et al. “Observation and cancellation of a perturbing dc stark shift in strontium optical lattice clocks”. In: *Ultrasonics, Ferroelectrics and Frequency Control, IEEE Transactions on* 59.3 (2012), pp. 411 –415. DOI: 10.1109/TUFFC.2012.2209.

[11] Hidetoshi Katori et al. “Engineering Stark Potentials for Precision Measurements: Optical Lattice Clock and Electrodynamic Surface Trap”. In: *AIP Conference Proceedings* 770.1 (2005), pp. 112–122. DOI: http://dx.doi.org/10.1063/1.1928846.

[12] E. J. Angstmann, V. A. Dzuba, and V. V. Flambaum. “Relativistic effects in two valence-electron atoms and ions and the search for variation of the fine-structure constant”. In: *Phys. Rev. A* 70 (2004), p. 014102. DOI: 10.1103/PhysRevA.70.014102.

[13] F. Riehle. *Frequency Standards: Basics and Applications*. Wiley, 2005.

[14] J. V. L. Essen L.and Parry. “An Atomic Standard of Frequency and Time Interval: A Caesium Resonator”. In: *Nature* 176.4476 (Aug. 1955), pp. 280–282.

[15] “Comptes Rendus de la 13e CGPM (1967/68)”. In: (1969), p. 103.

[16] J. Guéna et al. “Contributing to TAI with a secondary representation of the SI second”. In: *Metrologia* 51.1 (2014), p. 108.

[17] W.M. Itano et al. “Quantum projection noise : Population fluctuations in two-level systems”. In: *Phys. Rev. A.* 47 (1993), p. 3554.

[18] G. Santarelli et al. “Quantum Projection Noise in an Atomic Fountain: A High Stability Cesium Frequency Standard”. In: *Phys. Rev. Lett.* 82.23 (1999), p. 4619.

[19] P. D. Lett et al. “Optical molasses”. In: *J. Opt. Soc. Am. B* 6.11 (1989), pp. 2084–2107.

[20] R. H. Dicke. “The Effect of Collisions upon the Doppler Width of Spectral Lines”. In: *Phys. Rev.* 89 (2 1953), pp. 472–473. DOI: 10.1103/PhysRev.89.472.

[21] W.M. Itano and D.J. Wineland. “Laser cooling of ions stored in harmonic and Penning traps”. In: *Phys. Rev. A.* 25 (1982), p. 35.

[22] C. W. Chou et al. “Frequency Comparison of Two High-Accuracy Al^+ Optical Clocks”. In: *Phys. Rev. Lett.* 104.7 (2010), p. 070802. DOI: 10.1103/PhysRevLett.104.070802.

[23] R. G. DeVoe, J. Hoffnagle, and R. G. Brewer. "Role of laser damping in trapped ion crystals". In: *Phys. Rev. A* 39 (9 1989), pp. 4362–4365. DOI: 10.1103/PhysRevA.39.4362.

[24] Alan A. Madej et al. "$^{88}Sr^{+}$ 445-THz Single-Ion Reference at the 10^{-17} Level via Control and Cancellation of Systematic Uncertainties and Its Measurement against the SI Second". In: *Phys. Rev. Lett.* 109 (20 2012), p. 203002. DOI: 10.1103/PhysRevLett.109.203002.

[25] G. P. Barwood et al. "Agreement between two $^{88}Sr^{+}$ optical clocks to 4 parts in 10^{17}". In: *Phys. Rev. A* 89 (5 2014), p. 050501. DOI: 10.1103/PhysRevA.89.050501.

[26] N. Huntemann et al. "Improved Limit on a Temporal Variation of m_p/m_e from Comparisons of Yb^{+} and Cs Atomic Clocks". In: *Phys. Rev. Lett.* 113 (21 2014), p. 210802. DOI: 10.1103/PhysRevLett.113.210802.

[27] R. M. Godun et al. "Frequency Ratio of Two Optical Clock Transitions in $^{171}Yb^{+}$ and Constraints on the Time Variation of Fundamental Constants". In: *Phys. Rev. Lett.* 113 (21 2014), p. 210801. DOI: 10.1103/PhysRevLett.113.210801.

[28] M. G. Raizen et al. "Ionic crystals in a linear Paul trap". In: *Phys. Rev. A* 45 (9 1992), pp. 6493–6501. DOI: 10.1103/PhysRevA.45.6493.

[29] S. Seidelin et al. "Microfabricated Surface-Electrode Ion Trap for Scalable Quantum Information Processing". In: *Phys. Rev. Lett.* 96 (25 2006), p. 253003. DOI: 10.1103/PhysRevLett.96.253003.

[30] K. Pyka et al. "A high-precision segmented Paul trap with minimized micromotion for an optical multiple-ion clock". In: *Applied Physics B: Lasers and Optics* 114 (Jan. 2014), pp. 231–241. DOI: 10.1007/s00340-013-5580-5. arXiv:1206.5111 [physics.atom-ph].

[31] J. Keller et al. "Precise determination of micromotion for trapped-ion optical clocks". In: *ArXiv e-prints* (May 2015). arXiv:1505.05907 [physics.atom-ph].

[32] Yurii Ovchinnikov. Rudolf Grimm Matthias Weidemüller. "OPTICAL DIPOLE TRAPS FOR NEUTRAL ATOMS". In: *Advances in Atomic, Molecular and Optical Physics* 42 (2000), pp. 95–170.

[33] Hidetoshi Katori et al. "Ultrastable Optical Clock with Neutral Atoms in an Engineered Light Shift Trap". In: *Phys. Rev. Lett.* 91.17 (2003), p. 173005. DOI: 10.1103/PhysRevLett.91.173005.

[34] Harold J. Metcalf and Peter van der Straten. *Laser Cooling and Trapping*. Springer, 1999.

[35] Masami Yasuda et al. "Improved Absolute Frequency Measurement of the ^{171}Yb Optical Lattice Clock towards a Candidate for the Redefinition of the Second". In: *Applied Physics Express* 5.10 (2012), p. 102401. DOI: 10.7567/APEX.5.102401.

[36] B. J. Bloom et al. "An optical lattice clock with accuracy and stability at the 10-18 level". In: *Nature* 506 (Jan. 2014), p. 71.

[37] R. Le Targat et al. "Experimental realization of an optical second with strontium lattice clocks". In: *Nat Commun* 4 (July 2013), p. 2109.

[38] Stephan Falke et al. "A strontium lattice clock with 3x10-17 inaccuracy and its frequency". In: *New Journal of Physics* 16.7 (2014), p. 073023.

[39] J. J. McFerran et al. "Neutral Atom Frequency Reference in the Deep Ultraviolet with a Fractional Uncertainty 5.7x10-15". In: *Phys. Rev. Lett.* 108 (18 2012), p. 183004. DOI: 10.1103/PhysRevLett.108.183004.

[40] J Friebe et al. "Remote frequency measurement of the 1S0-3P1 transition in laser-cooled 24 Mg". In: *New Journal of Physics* 13.12 (2011), p. 125010.

[41] David R. Lide. *CRC Handbook of Chemistry and Physics*. CRC Press, 2005.

[42] D. M. Harber et al. "Effect of cold collisions on spin coherence and resonance shifts in a magnetically trapped ultracold gas". In: *Phys. Rev. A* 66 (5 2002), p. 053616. DOI: 10.1103/PhysRevA.66.053616.

[43] A. V. Taichenachev et al. “Magnetic Field-Induced Spectroscopy of Forbidden Optical Transitions with Application to Lattice-Based Optical Atomic Clocks”. In: *Phys. Rev. Lett.* 96.8, 083001 (2006), p. 083001. DOI: 10.1103/PhysRevLett.96.083001.

[44] Michael M. Petersen. “Laser-cooling of Neutral Mercury and Laser-spectroscopy of the 1S0-3P0 optical clock transition”. PhD thesis. Université de Paris VI, 2009.

[45] M.C. Bigeon. “Probabilité de transition de la raie 6 1S0-6 3P0 du mercure”. In: *Journal de Physique* 28 (1967), p. 51.

[46] A. Kramida et al. *NIST Atomic Spectra Database (ver. 5.2)*. 2015. URL: http://physics.nist.gov/asd.

[47] H. Hachisu et al. “Trapping of Neutral Mercury Atoms and Prospects for Optical Lattice Clocks”. In: *Phys. Rev. Lett.* 100 (2008), p. 053001. DOI: 10.1103/PhysRevLett.100.053001.

[48] Sergey G. Porsev and Andrei Derevianko. “Multipolar theory of blackbody radiation shift of atomic energy levels and its implications for optical lattice clocks”. In: *Phys. Rev. A* 74 (2006), p. 020502. DOI: 10.1103/PhysRevA.74.020502.

[49] Andrei Derevianko and Hidetoshi Katori. “Colloquium: Physics of optical lattice clocks”. In: *Rev. Mod. Phys.* 83.2 (2011), pp. 331–348. DOI: 10.1103/RevModPhys.83.331.

[50] Thomas Middelmann et al. “High Accuracy Correction of Blackbody Radiation Shift in an Optical Lattice Clock”. In: *Phys. Rev. Lett.* 109 (26 2012), p. 263004. DOI: 10.1103/PhysRevLett.109.263004.

[51] L. Yi et al. “Optical Lattice Trapping of ^{199}Hg and Determination of the Magic Wavelength for the Ultraviolet $^1S_0 \leftrightarrow {}^3P_0$ Clock Transition”. In: *Phys. Rev. Lett.* 106.7 (2011), p. 073005. DOI: 10.1103/PhysRevLett.106.073005.

[52] H. Katori et al. “Strategies for reducing the light shift in atomic clocks”. In: *Phys. Rev. A* 91 (2015), p. 052503. DOI: 10.1103/PhysRevA.91.052503.

[53] Robert W. Boyd. *Nonlinear Optics, Third Edition*. 3rd. Academic Press, 2008.

[54] T.W. Hänsch and B. Couillaud. "Laser frequency stabilization by polarization spectroscopy of a reflecting reference cavity". In: *Opt. Commun.* 35 (1980), p. 441.

[55] J. Friebe et al. "β-BaB2O4 deep UV monolithic walk-off compensating tandem". In: *Optics Commun.* 261 (2006), p. 300.

[56] S. Mejri et al. "Ultraviolet laser spectroscopy of neutral mercury in a one-dimensional optical lattice". In: *Phys. Rev. A* 84 (3 2011), p. 032507. DOI: 10.1103/PhysRevA.84.032507.

[57] S. Mejri et al. "Towards an optical lattice clock based on mercury: Loading of a dipole trap". In: *EFTF-2010 24th European Frequency and Time Forum Proceedings*. 2010.

[58] J. J. McFerran et al. "Sub-Doppler cooling of fermionic Hg isotopes in a magneto-optical trap". In: *Opt. Lett.* 35.18 (2010), pp. 3078–3080.

[59] C. Monroe et al. "Very cold trapped atoms in a vapor cell". In: *Phys. Rev. Lett.* 65.13 (1990), pp. 1571–1574. DOI: 10.1103/PhysRevLett.65.1571.

[60] R. W. P. Drever et al. "Laser phase and frequency stabilization using an optical resonator". In: *Applied Physics B: Lasers and Optics* 31.2 (June 1983), pp. 97–105.

[61] S. Mejri. "Horloge 'a r'eseau optique de mercure : D'etermination de la longueur d'onde magique." PhD thesis.

[62] S. Blatt et al. "Rabi spectroscopy and excitation inhomogeneity in a one-dimensional optical lattice clock". In: *Phys. Rev. A* 80.5 (2009), p. 052703. DOI: 10.1103/PhysRevA.80.052703.

[63] W. Demtroeder. *Laser spectroscopy, Basic concepts and Instrumentation*. Springer, 2003.

[64] T. A. Savard, K. M. O'Hara, and J. E. Thomas. "Laser-noise-induced heating in far-off resonance optical traps". In: *Phys. Rev. A* 56.2 (1997), R1095–R1098. DOI: 10.1103/PhysRevA.56.R1095.

[65] D. A. Howe D. B. Sullivan D. W. Allan and F. L. Walls. "Characterization of Clocks and Oscillators". In: *NIST Technical Note* 1337 (1990).

[66] David J. Griffiths. *Introduction to quantum mechanics*. Prentice Hall, 2005.

[67] J. J. McFerran et al. "Laser locking of the 199Hg 1S0-3P0 transition with 5.7×10^{-15} fractional frequency Instability". In: *Opt. Lett.* 37.17 (2012), pp. 3477–3479.

[68] L. M. Lifshitz L. D. Landau. *Quantum Mechanics, Third Edition: Non-Relativistic Theory (Volume 3)*. Butterworth-Heinemann, 2004.

[69] Audrey Quessada et al. "The Dick effect for an optical frequency standard". In: *Journal of Optics B: Quantum and Semiclassical Optics* 5.2 (2003), S150–S154.

[70] J. Ye A. Ludlow M. Boyd. "OPTICAL ATOMIC CLOCKS". In: *arXiv:1407.3493v2* (2015).

[71] Kazuhiro Yamanaka et al. "Frequency Ratio of $^{199}\mathrm{Hg}$ and $^{87}\mathrm{Sr}$ Optical Lattice Clocks beyond the SI Limit". In: *Phys. Rev. Lett.* 114 (23 2015), p. 230801. DOI: 10.1103/PhysRevLett.114.230801.